

YALE UNIVERSITY

DOCTORAL THESIS

**New Methods and Phenomena in
The Study of Correlated Complex
Oxides**

Author:
Alexandru B.
GEORGESCU

Supervisor:
Prof. Sohrab
ISMAIL-BEIGI

*A thesis submitted in fulfillment of the requirements
for the degree of Doctor of Philosophy*

in the

Ismail-Beigi Group
Physics Department

September 22, 2017

“The first principle is that you must not fool yourself and you are the easiest person to fool.”

Richard Feynman

Yale University

Abstract

Physics Department

Doctor of Philosophy

New Methods and Phenomena in The Study of Correlated Complex Oxides

by Alexandru B. GEORGESCU

Transition metal oxides have long been an important subject of study, both theoretically and experimentally. The wide array of phases possible in their bulk forms (high T_c superconductivity, colossal magnetoresistance, ferroelectricity, etc.) makes them of scientific and technological significance, while relatively recent materials deposition techniques have allowed researchers to grow new, 'artificial' materials in the form of heterostructures and thin films. These structures offer a rich array of parameters to explore, as interfaces and thin films often show patterns of behavior that are quite different from their parent bulk compounds. From the point of view of electronic structure theory, this offers a rich playground where one can search for new physical phenomena. What makes transition metal oxides physically interesting is also what makes them difficult to study theoretically: the transition metal d-orbitals that dictate the wide array of phases in this class of materials cannot always be treated appropriately within band theory due to strong local electron-electron interactions. The local interactions are most often treated with a multi-band Hubbard model 'glued' on top of the first principles calculation. In this thesis, we have explored both a variety of complex oxide heterostructures and phenomena as well as advanced the computational framework used to describe them. We have analyzed the effect of local electrostatic fields at a ferroelectric-manganite interface as seen by electron energy loss spectroscopy, found a dimer-Mott state in a cobaltate-titanate interface, and identified new sources of orbital polarization at a nickelate-aluminate interface. We have also developed a generalized slave-boson formalism for multi-band Hubbard models that can be applied in large scale calculations involving complex oxide heterostructures and thin films.

Acknowledgements

It's become a common joke to say that 'it takes a village to raise an academic', and I guess it's my time to list the members of the village that helped 'raise' me until now and make an effort to keep things to one page. I would like to thank Sohrab Ismail-Beigi for being a great advisor over the past five years. From our weekly meetings and physics discussion sessions that often lasted many, many hours, to his consistent guidance to help me become a better scientist as well as a better speaker. There are many things I could say but in summary: I don't see how I could have asked for more from an advisor. I am thankful for having a great Ph.D committee made out of Fred Walker, Leonid Glazman and John Tully. Their mentoring through committee meetings, discussions and collaboration have broadened my perspective as a scientist. I would like to thank my group members and friends over the past five years, Xin Liang (thanks for teaching me how to drive!), Mehmet Dogan, Arvin Kakekhani, Minjung Kim, Subhasish Mandal, Andrei Malashevich, Stephen Eltinge and Jie Jiang. Working and especially traveling with our group to conferences led to some of my best memories from the past few years. I would also like to thank my collaborators, Charles Ahn, Christine Broadbridge, Robert Klie, Divine Kumah, Matthew Marshall, Ankit Disa, Sangjae Lee, Cristina Visani and Eddie Jia. I am incredibly thankful to my wife and best friend, Ayinka Ambrose Georgescu, for all the love and support over the past 8 and a half years as well as to my family and hers for the constant support and encouragement. I am very lucky to have had great friends outside of my research group as well, who offered support both at Yale and from far away from Yale over the past few years. Of the friends not at Yale, I would like to thank my oldest friend in the US whom I've met before coming here, Ion Mihailescu, my 'sister' Jennifer Gillman, Atanas Atanasov, Ivy Chen, Camille Avestruz and Matthew Lightman. Finally, I would like to thank my friends at Yale who - alongside my advisor and group members - have felt like a family away from home. So I would like to thank Derek Murray, Elizabeth Mo, Dave Carper, Teresa Brecht, Omur Dagdeviren, Siddharth Prabhu, Niveditha Samudrala and Ashley Tapley for all the support - especially throughout the past year. Finally, I would like to thank my coach, Mark Robb for helping me continue to push myself and get out of my own way, an attitude which was no doubt reflected in the way I do science. Once again, thanks everybody.

Contents

Abstract	iii
Acknowledgements	v
1 Introduction	1
2 Methods	7
Density Functional Theory (DFT)	7
Pseudopotentials	13
Virtual Crystal Approximation (VCA)	14
DFT+U	15
Wannier Functions	16
O-K Edges in Electron Energy Loss Spectroscopy	19
The Z and Z+1 Approximation for EELS	21
3 A Generalized Slave-Particle Method For Extended Hubbard Models	23
3.1 The Generalized Slave-Particle Representation	26
3.1.1 Number slave	34
3.1.2 Orbital slave	37
3.1.3 Spin slave	38
3.1.4 Spin+orbital slave	39
3.2 Mean-Field Tests	41
3.2.1 Single-band Mott transition	43
3.2.2 Isotropic two-band Mott transition	45
3.2.3 Anisotropic Orbital-Selective Mott Transition	46
3.2.4 Ground State Energies	54
3.3 Conclusion	58
3.4 Appendix	59
4 Symmetry Breaking in Occupation Number Based Slave-Particle Methods	63
4.1 The Slave-Particle Approach	66
4.2 Single-site mean-field approximation	71
4.3 Difficulties Obtaining Symmetry Broken Phases	72
4.4 Symmetry breaking fields	75

4.5	Self-consistent total energy approach	80
4.6	Simplified and more efficient slave-particle approach	82
4.7	Conclusion	86
5	Ionic Potential and Band Narrowing as a Source of Orbital Polarization in Nickelate/Aluminate Superlattices	87
5.1	Methodology	88
5.2	Results	90
5.3	Test Case: Band Narrowing in SrVO ₃	100
5.4	Band narrowing in NAO/NNO	103
5.5	Conclusions	104
6	EELS Spectra in Manganite-Ferroelectric Interfaces	105
6.1	Methodology	107
6.2	Results	110
6.3	Conclusions	124
7	Dimer Mott Insulator State in a Cobaltate-Titanate Heterostructure	125
7.1	Methodology	126
7.2	Results	126
7.3	Conclusions	135
8	Outlook	137
	Bibliography	141

List of Figures

1.1	The large array of physical properties of transition metal oxides that occur from a combination of structural distortions and interplay between local and non-local effects.[1].	2
1.2	From the left: An impurity site is 'glued' on top of the calculated electronic structure from DFT - typical for all 'post-DFT' methods for correlated materials - after which, in this particular case in DMFT, one scans through the various possible allowed local electronic configurations to describe the interacting impurity site. Image from Ref. [11].	4
2.1	16
3.1	Visual representation of a few possible slave-particle models within our formalism.	35
3.2	Quasiparticle weight Z as a function of U/U_c for different slave-particle models for the paramagnetic single-band Hubbard at half filling. U_c is the critical value of U when $Z = 0$, i.e., the Mott transition, for each model. The black crosses show slave rotor results, the blue circles are the Gutzwiller approximation results ($Z = 1 = \frac{U^2}{U_c^2}$) which for this model are the same as the spin+orbital slave ("slave-spin") results in blue crosses, and the green circles show the orbital slave results (identical to the number slave). We note that the slave-orbital Hilbert space is very small, so that it does not agree with the rotor, unlike the two-band slave number.	45
3.3	Quasiparticle weight Z as a function of U/U_c for different slave-particle models for a degenerate paramagnetic two-band Hubbard model at half filling.	46

- 3.4 Quasiparticle weights for the paramagnetic anisotropic two-band single-site Hubbard model at half filling as predicted by the orbital+spin slave model (blue) and the orbital slave model (red) at $J = 0$ for three t_2/t_1 ratios. In each plot, the Z value for the first orbital with larger hopping t_1 is denoted by symbols while for the second orbital solid lines with no symbols are used. An OSMT occurs when the two Z do not go to zero at the same U value: orbital slave (red) in the center plot and both slave models in the lower plot. 48
- 3.5 Phase diagram for the anisotropic two-band single-site Hubbard model at half-filling as a function of the anisotropy ratio t_2/t_1 and J . Two slave boson methods are used: orbital slave (red circles) and spin+orbital slave (blue crosses). In each case, the boundary curve demarcates the possible existence of an Orbital-Selective Mott Transition when U is ramped up from $U = 0$. Regions above the boundary display OSMT while regions below it present a standard Mott transition where both bands become insulating at the same critical U_c value. 52
- 3.6 Phase diagram for the anisotropic two-band single-site Hubbard model at half-filling as a function of the anisotropy ratio t_2/t_1 and J for the spin+orbital slave model. Three different interaction terms are used: intra-orbital term only which is Eq. (3.27), intra-orbital plus Hund's which is Eq. (3.29), and all terms included which is Eq. (3.30) 53
- 3.7 Ground-state energy per site (E_g/t) of a single band Hubbard model at $J = 0$ in the paramagnetic phase at half filling for a variety of slave representations as well as for the Hartree-Fock approximation. $D = 2t$ is the band width of the non-interacting system. For this model the orbital slave is identical to the number slave and the spin slave is the same as the spin+orbital slave. 56
- 3.8 Ground-state energy per site (E_g) for an isotropic two-band Hubbard model at half filling for $J = 0$ in the paramagnetic and paraorbital phase. 57
- 4.1 $\Delta n = n_\uparrow - n_\downarrow$ as a function of $\Delta h = h_\uparrow - h_\downarrow$ on one site of the 1D half-filled single band Hubbard model with $U = 2$ and $t = 1$. Upper figure is for the FM phase, and the lower figure for the AFM phase. The Δh dependence of the spinon and slave occupancies are shown separately. Self-consistency between the two requires zero occupancy difference. 74

4.2	Total energy per site and quasiparticle weight Z (renormalization factor) versus symmetry breaking perturbation field strength b based on the slave-rotor method for the half-filled single-band 1D Hubbard model with $U = 2$ and $t = 1$	77
4.3	Total energy per site and Z versus field strength b for the number-slave method for the single-band 1D Hubbard model at half filling with $U = 2$ and $t = 1$	78
4.4	Total energy per site and Z versus field b for the spin+orbital-slave approach for the single-band 1D Hubbard model at half filling with $U = 2$ and $t = 1$. Unlike the number-slave and slave-rotor, correlations decrease with increasing b for the AFM phase and slowly increase with b for the FM phase.	78
4.5	78
4.6	Comparison of the ground state energies (in units of t) for the single-band 1D Hubbard model at half filling based on the AFM Hartree-Fock solution, the PM slave-spin solution, the symmetry broken (AFM) slave-spin ground state solution, and the exact Bethe Ansatz (AFM) solution as calculated by the method of Ref. [59].	85
5.1	1x1 structure of $(\text{NNO})_1/(\text{NAO})_4$ and fully relaxed $c(2 \times 2)$ $(\text{NNO})_1/(\text{NAO})_3$ as simulated in Quantum Espresso. We only use 3 layers of NAO in order to have an even number of octahedra and allow for octahedral distortions	92
5.2	Projected density of states of the Ni e_g orbitals for the $(\text{NNO})_1/(\text{NAO})_4$ heterostructure.	94
5.3	Simplified picture of how confinement changes inter-orbital hoppings, band widths, and covalence. Top: a p-d Hamiltonian that includes alternating higher and lower energy orbitals in a periodic way (similar to bulk NNO in any axial direction or Ni $x^2 - y^2$ orbital and in-plane oxygens in NNO/NAO). Bottom: a similar Hamiltonian with the same hopping terms and on-site energy differences that, however is not periodic due to the confinement (insulating layers surround this subsystem). This describes the $3z^2 - r^2$ orbital in the $(\text{NNO})_1/\text{NAO}$ system. While the immediate environment around the d orbitals is the same, the hoppings to father sites are not and this modifies band widths and covalence.	96

5.4	Schematic representation of the NNO/NAO interface. Note that hopping is energetically costly (i.e., forbidden) onto the Al in the NAO from O_b (due to the high energy of the local states on Al). As one proceeds away from the NiO_2 layer, the oxygens become more occupied as the environment becomes more ionic, i.e. $n(O_a) < n(O_b) < n(O_c)$. Image from Disa, Georgescu et al (under review).	97
5.5	Potential difference averaged in the x-y direction in the NNO layer between NNO/NAO and NNO/NNO as a function of z position offset from the Ni (arbitrary horizontal linear axis units). The $3z^2-r^2$ orbital (red) samples a lower potential than the x^2-y^2 orbital (blue), leading to an energy splitting between the two orbitals.	99
5.6	Simple physical picture of how band narrowing can reverse the direction of orbital polarization. Left: the average energy of the $3z^2 - r^2$ is lower than that of $x^2 - y^2$, however the $x^2 - y^2$ is quite broad and thus more of it is under the Fermi level, leading to a higher occupancy. Right: narrowing both bands by a significant amount leads to a higher occupancy of the band that has an average lower energy. In the limit of bands of zero width, the $x^2 - y^2$ would have zero occupancy, and we would have maximum orbital polarization.	101
5.7	Basic schematic of the software used for the slave-particle calculation on real materials, starting with Quantum Espresso, continuing with Wannier90 and finishing with slave-particle calculations done with our software	102
5.8	Spectral functions for $SrVO_3$. Left: ARPES [61] and Right: DMFT [14] calculations, Middle: LDA+Slave. Despite a much simpler, faster approach, we reach very good agreement with DMFT and experiment.	102
6.1	(A-C) Schematic of the $BaTiO_3/LSMO$ interface where the purple part represents LSMO and light blue represents BTO. The oxygen octahedron changes its ratio with ferroelectric polarization. (D-F) Relaxed atomic structures from first-principles calculations. The structure is strained to an STO substrate (not shown) and uses Platinum as an electron reservoir (not shown). This figure was first published in a previous work[26]	108

6.2	Z+1 calculations for two different doping levels of bulk $\text{La}_{1-x}\text{Sr}_x\text{MnO}_3$. Computed O $2p$ PDOS are in black and cation d PDOS are below them in blue and green. Note the two main effects of the change in doping: hole doping leads to an increased Mn-prepeak, while the change in element from La to Sr increases the relative energy of the La/Sr prepeak as Sr d states are higher in energy than La d states.	111
6.3	Z+1 calculations for fully relaxed LaMnO_3 and SrMnO_3 versus experimental data. Both show good agreement between theory and experiment.	111
6.4	Z+1 calculations from a 1×1 supercell interface for LSMO/BTO. What are plotted are projected densities of states (PDOS) onto O $2p$ (the “O-K edge” data in black) and the various cation d orbitals at the interface. The normalization of the plots is arbitrary. Top two plots are for depletion and bottom two plots are for accumulation. Notice the upward shift in energy of the Ba d states and the La/Sr d states in the accumulation state compared to the depletion state as well as the increase in the Mn $3d$ density of states above E_F for accumulation.	113
6.5	Energy shifts of various cation states across the LSMO/BSTO interface computed in two different ways. The blue dots show shifts of the layer-averaged electrostatic potential going from accumulation to depletion. They are compared to shifts of the cation PDOS peaks for the BaO and La/SrO layers as well showing close agreement. As expected, deep inside the metallic LSMO the shifts go to zero.	115
6.6	Simple electrostatic model of the LSMO/BTO system for the Accumulation State. Due to the ferroelectric field effect, electrons “run away” from the interface between the LSMO and the BTO, and the remaining holes act as the screening charge. The electrode on the other side of the BTO is the reservoir accepting the electrons. Hence, the energy shifts in the Ba d and La/Sr d PDOS and local potential correspond this effect. The depletion depletion state corresponds to the opposite of this effect.	116
6.7	Comparison of DFT-computed and measured O-K edge EELS spectra for the O atoms in the interfacial MnO_2 layer at the LSMO/BTO interface. The columns label the interfacial state and the rows show a comparison between the Z and Z+1 theoretical models.	117

6.8	Comparison of DFT-computed and measured O-K edge EELS spectra for O atoms in the second MnO ₂ layer of LSMO. The spectra are already bulk-like in this layer and show good agreement between theory and experiment. Shown here are depletion (left) and accumulation (right)	120
6.9	Comparison of DFT-computed and measured O-K edge EELS spectra for the O atoms in the second TiO ₂ layer in BTO, depletion (left) and accumulation (right). The spectra are already bulk-like and match experiment well.	121
6.10	Steps in the STO substrate can lead to defects in the interface. An incoming electron samples both the TiO ₂ layer and the MnO ₂ layer, requiring an interpolation of the spectra of the two layers to appropriately describe the EELS spectra.	121
6.11	EDS image of the sample from our experimental collaborators at University of Illinois at Chicago. Note that as one follows the red line upwards, the atoms to the right are shown as darker. This signals that there is an increased amount of LSMO. A beam passing through the LSMO/BTO layer would see intermixing at that interface, as described in Figure 6.10.	122
6.12	Experimental O-K edge compared to theoretical O-K edge simulated by linear superposition of 70% of the interfacial LSMO O-K edge obtained from the MnO ₂ layer and 30 % of BTO TiO ₂ layer for the depletion interfacial layer.	123
7.1	(LCO) ₂ /(LTO) ₂ , fully relaxed with a c(2×2) in-plane unit cell (left) and 1×1 (right). Periodic boundary conditions are imposed in theoretical calculation along the superlattice direction, whereas experiment uses 20 repetitions of the unit cell.	128
7.2	Right: a visual illustration of charge transfer in the superlattice, as one electron is transferred across the interface. Left: projected densities of states (PDOS) for all Ti d states (top) showing primarily unoccupied Ti d states and hence a 4+ valence (the conduction band is empty). PDOS for Co e _g states (bottomw), showing a narrow filled band below the Fermi level and more unoccupied states above the Fermi level. Note that bulk LCO has all e _g character states are above the Fermi level	130

- 7.3 Left: schematic representation of the Co octahedron at the LCO/LTO interface. The O atom at the top is 'pulled' towards the Ti atom with a 4+ valence instead of the 2+ Co. Right: the resulting distorted structure. 131
- 7.4 Top: projected density of states of Co e_g orbitals in bulk LCO. Bottom: projected density of states for Co e_g orbitals in the LCO/LTO superlattice. Both valence bands are empty in the bulk, however after charge transfer that is mainly isolated to the $3z^2 - r^2$ (denoted as z^2 in the legend) orbital in the superlattice, the e_g states show large orbital polarization and a narrow band gets filled right below the Fermi level. 132
- 7.5 Right: plots of the unoccupied state right above the Fermi level (top) and the occupied state right below the Fermi level (bottom) at $k = 0$. What is shown are isosurfaces $|\Psi_{k=0}(r)|^2 \times \text{sign}(\Psi_{k=0}(r))$. The in-phase and out-of-phase nature is easily visible as is the dominant $3z^2 - r^2$ character on each Co site. We identify this pair as a bonding and anti bonding pair (left) of a simple diatomic molecular system. 133
- 7.6 "Particle in a box" picture: understanding of the bonding-anti-bonding pair in the interfacial LCO bilayer. Since the transferred electron on each Co is confined to the bilayer system of Co (due to insulating band offset with the LTO), we get confined electronic states. The two nearby Co $3z^2 - r^2$ pair and form bonding and antibonding states, essentially forming a diatomic molecular system. 134

List of Tables

5.1	Electron occupation and orbital polarization of e_g orbitals as a function of strain and with and without octahedral distortions based on DFT calculations.	90
5.2	Electron occupation numbers and average energies for Ni e_g orbitals for the $(\text{NNO})_1/(\text{NAO})_4$ 1×1 structure calculation for different values of U within DFT+U theory.	91
5.3	Occupation numbers for oxygen apical $2p$ orbitals ($2p$ orbitals pointing along the local cation-O-cation direction on each oxygen). Oxygens are defined by Figure 5.4. The increased occupancy going from NNO to NAO indicating increased ionicity & decreased covalence.	98
5.4	Slave-number calculations on the 1×1 NNO/NAO superlattice. Note that around $U = 10$ and $m^*/m_{DFT} = 2.15$, the orbital polarization starts matching the direction from experiment	104
7.1	Band gap, displacement along the z direction between O and La in the interfacial LaO layer between Ti and CO, and Löwdin electron count of the d orbitals on Co and Ti as a function of the U on Co and Ti. Increasing the U on Ti (but not on Co) significantly affects both charge transfer and interfacial distortions. Calculations done allowing full a full $c(2 \times 2)$ unit cell in the x-y plane, allowing for full octahedral distortions	131

Dedicated to Ayinka, my parents and my sisters.

Chapter 1

Introduction

Transition metal oxides have long been a subject of study in both theoretical and experimental physics. This is due to their technological utility (for example, as ferroelectrics) as well as due to their fascinating and less-well understood properties which relate to fundamental issues in condensed matter physics (e.g., high temperature superconductivity) which also have possible practical use - if they can be harnessed.

Even in bulk form, the physical behavior of transition metal oxides is dominated by many competing degrees of freedom and order parameters (lattice, orbital, spin, charge). Due to this complexity, combining different transition metal oxides into new, 'artificial' materials is a promising avenue of study for the discovery of new phenomena not found in their parent compounds. As experimental approaches continue to push the boundaries on the precision and complexity of the materials that can be fabricated, it has become increasingly important that theory predict which materials are relevant to grow in order to focus experimental efforts. Furthermore, with advances in spectroscopy through which materials can be understood at the level of individual atoms (Atomic Force

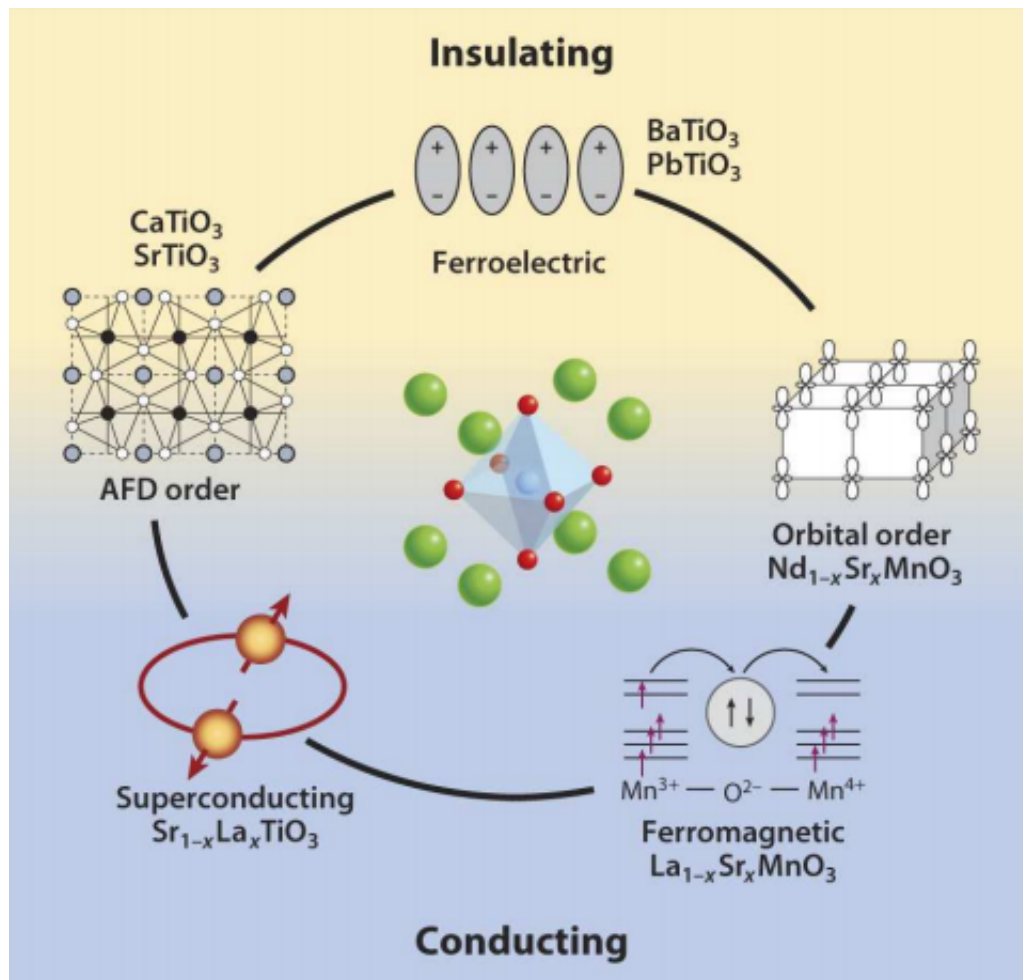


FIGURE 1.1: The large array of physical properties of transition metal oxides that occur from a combination of structural distortions and interplay between local and non-local effects.[1].

Spectroscopy, Electron Energy Loss Spectroscopy), it has become increasingly important that theory become predictive in order to understand and explain spectroscopic results.

Starting with the Kohn-Sham equations, [2, 3] Density Functional Theory (DFT) has been the main workhorse in understanding the basic properties of many materials including transition metal oxides. One of its advantages is that, rather than solving the full many-body electron

problem, it solves a single-particle problem with the many-body interactions approximated by an 'exchange-correlation' potential calculated from the average electron density. This allows for atomic and electronic structure predictions of surprising accuracy with a relatively low computational cost, making DFT indispensable for modeling of novel materials.

At the same time, DFT's main advantage as a single-particle theory is also one of its biggest headaches when treating the electronic structure of transition metal oxides. The 3d orbitals on the transition metal cations exhibit 'strong correlations', i.e., the local Coulomb interaction on the orbitals is so strong that many-body effects at the local level compete with long-range electron transport and make the band picture inaccurate and at times inadequate.

In order to treat local interactions, a standard approach has been to focus a single atom and treat it as an interacting impurity with a set of localized electronic states within a bath of conduction electrons (e.g., the Anderson model [4, 5]). The next level is to connect all these interacting impurities together to create a Hubbard model [6]. Even within the simplest context, however, Hubbard models for solid state systems have been very difficult to solve exactly or even accurately over a wide range of their model parameters, requiring the development of new theoretical tools. Some examples are slave-boson methods [7–10] (described in some detail in this thesis) and Dynamical Mean-Field Theory (DMFT) [11, 12]. In addition, a model Hamiltonian approach necessarily relies heavily on the set of adjustable parameters it contains (e.g., the Hubbard local repulsion energy U).

In recent decades, computational improvements have allowed researchers

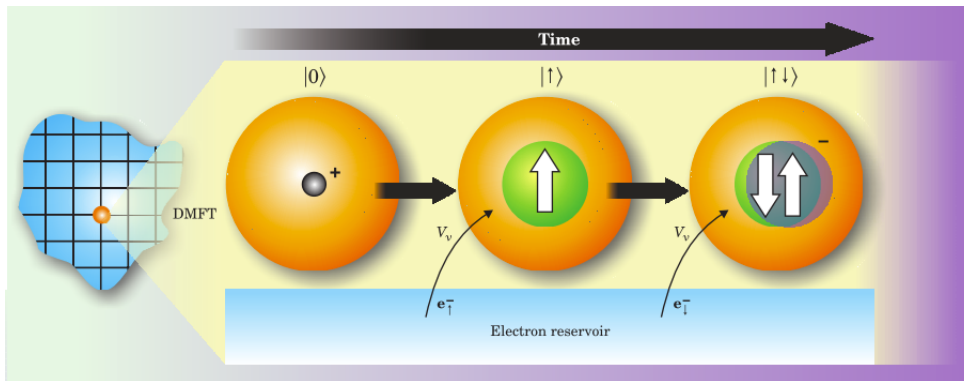


FIGURE 1.2: From the left: An impurity site is 'glued' on top of the calculated electronic structure from DFT - typical for all 'post-DFT' methods for correlated materials - after which, in this particular case in DMFT, one scans through the various possible allowed local electronic configurations to describe the interacting impurity site. Image from Ref. [11].

to 'glue' impurity models on top of Density Functional Theory within various levels of approximation, with the most common one being DFT+DMFT [11].

DFT+DMFT has often allowed for great progress, particularly in terms of spectroscopic properties - especially ARPES - in the bulk [13, 14]. However, it involves the very expensive self-consistent computation of the local Green function (i.e., the solution of the interacting impurity problem) which does not lend itself well to use on heterostructures that often involve over 100 atoms and 20 different impurity sites. For this reason, we began with two recent methods to solve the Hubbard model that are extremely inexpensive computationally by comparison: the slave-rotor [8–10] and slave-spin [15, 16] approaches. While developing our own numerical implementation for these methods, we discovered that they can be generalized [17] to an array of intermediate models of occupation-based slave-boson methods. Since one of the goals of using this class of

model is to be able to understand long-range order in materials, we also had to develop a way to include spontaneous symmetry breaking, as all previous work using the slave-rotor and slave-spin relied on a Hund's J coupling term or structural symmetry breaking to induce spin symmetry breaking [10, 18]. We have shown that within these existing slave-boson frameworks, one could not even obtain a self-consistent antiferromagnetic solution for a one dimensional, single band Hubbard model at half-filling. However, we have shown that the addition of symmetry breaking fields actually leads to a simpler, more efficient and stable computational framework for slave-particle calculations that also allows for spontaneous symmetry breaking.

The remainder of this thesis is organized as follows. In Chapter 2, we discuss some of the methods that we've used as they relate to Density Functional Theory. In Chapter 3, we discuss the generalized slave-particle framework we have developed that builds upon the slave-rotor and slave-spin approaches. In Chapter 4, we use both density functional theory and slave-particle methods to analyze new sources of orbital polarization in an aluminate-nickelate interface. In Chapter 5, we use density functional theory methods to analyze the electron energy loss spectra at a manganite-ferroelectric interface. In Chapter 6, we discuss an unconventional insulating state in a cobaltate-titanate heterostructure. In Chapter 7, we present an outlook on open questions and future work.

Chapter 2

Methods

Density Functional Theory (DFT)

DFT is the main workhorse of computational material physics based on first principles electronic structure. The main idea behind it is that, often, we can access many useful physical observables without explicitly solving the full many-body interacting electron problem. Instead, we can use a mean-field single-particle approach that is appropriately designed to give key observables correctly. As mentioned in the Introduction, this is also its main weakness when it comes to transition metal oxides.

The main point in DFT is to avoid explicit solution of the quantum mechanical equation for the electronic ground state

$$H\Psi_0 = E\Psi_0 \quad (2.1)$$

where Ψ_0 is the ground state many-body wavefunction of an N -electron system. In natural units ($\hbar = 1, e = 1, m_e = 1$) the electronic Hamiltonian is

$$H = T + V_{ee} + V_{ei} \quad (2.2)$$

which is the sum of the electronic kinetic energy

$$T = -\frac{1}{2} \sum_{j=1}^N \nabla_j^2, \quad (2.3)$$

the electron-electron repulsive interaction energy

$$V_{ee} = \frac{1}{2} \sum_{j \neq k}^N \frac{1}{|r_j - r_k|}, \quad (2.4)$$

and the electron-ion attractive interaction energy

$$V_{ei} = - \sum_J \frac{Z_J}{|r - R_J|}. \quad (2.5)$$

To solve the many-body equation exactly, we would have to tabulate the anti-symmetrized wavefunction:

$$\Psi_0(r_1, r_2, \dots, r_i, \dots, r_j, \dots, r_N) = -\Psi_0(r_1, r_2, \dots, r_j, \dots, r_i, \dots, r_N) \quad (2.6)$$

for all inequivalent combinations of the electron coordinates $\{r_j\}$ (spin indices are suppressed for simplicity). In real space, for a spatial representation that allows g grid points, to represent the N wave function Ψ_0 , we would need on the order of g^N tabulated values which scales exponentially in the number of electrons. This clearly shows a need for a simpler (e.g., single-particle) approach. Modern DFT algorithms are much more efficient than exponential scaling: in fact, their computational cost typically scales cubically in the number of electrons, i.e. $O(N^3)$. As opposed to solving the full problem, however, DFT describes information such as:

- the ground state energy of the system E_0 ; and thus energy differences between various configurations of atoms (particularly useful in physical chemistry)
- the electron density, $n(r)$
- single particle band energies (which are not always reliable, as we'll discuss later)

The first two (energy and density) DFT can, in principle, describe exactly. The band energies are in principle suspect and inexact, but in practice enormously useful for analysis of materials properties.

In order to create a single-particle approach, we write the equation in the energy E_0 in the following way:

$$E_0 = \langle \Psi_0 | T + V_{ee} + V_{ei} | \Psi_0 \rangle = \langle \Psi_0 | T + V_{ee} | \Psi_0 \rangle + \int n(r)v(r). \quad (2.7)$$

Here $v(r)$ is the potential felt by electrons due to the ions

$$v(r) = - \sum_I \frac{Z_I}{|r - R_I|}$$

which in fact specifies the specific electronic Hamiltonian to be solved for a particular material. The other energies have no dependence on the actual problem being solved.

We define an energy functional for this universal part

$$F = \langle \Psi_0 | T + V_{ee} | \Psi_0 \rangle \quad (2.8)$$

The Hohenberg-Kohn theorems [3] that describe how to solve the above equations are the following.

Theorem 1: $v(r)$ is a unique function of $n(r)$, i.e., there is a unique bijection between $v(r)$ and $n(r)$. Usually, we are given $v(r)$ and then solve for Ψ_0 which then yields $n(r)$. This theorem means we can instead use the ground state density $n(r)$ as a working variable. So, in fact, Ψ_0 is a functional of $n(r)$ which we denote as $\Psi_0[n]$. And so is $F[n]$.

This permits us to define an energy functional of any density \tilde{n} (which is some ground state density)

$$E[\tilde{n}] = F[\tilde{n}] + \int dr \tilde{n}(r)v(r) \quad (2.9)$$

Theorem 2 $E[n]$ takes its minimum value at the ground state electron density $n_0(r)$ associated with $v(r)$, and its value is the ground state energy E_0 . Hence we have a variational principle: we minimize $E[\tilde{n}]$ over trial densities and the lowest energy one is the right one (and delivers the ground state energy).

These two theorems show that we can find the ground state energy of a system as a function of the local potential and thus of the electronic density. However, they do not tell us what $F[n]$ is.

Kohn and Sham [2] invented a set of N fictitious independent electron degrees of freedom $\{\psi_j(r)\}$ where the electron density for N electrons is given as

$$n(r) = \sum_{j=1}^N |\psi_j(r)|^2. \quad (2.10)$$

The **Kohn-Sham equations** show that one can find these electronic states

by solving a Schrodinger equation for independent electrons. These equations are

$$-\left[\frac{\nabla^2}{2} + v_{eff}(r)\right]\psi_j(r) = \epsilon_j\psi_j(r). \quad (2.11)$$

The effective potential v_{eff} is the sum of the ionic, the Hartree (electrostatic term) as well as the 'exchange-correlation' potentials.

$$v_{eff}(r) = v(r) + \int dr' \frac{n(r')}{|r - r'|} + v_{xc}(r) \quad (2.12)$$

where $v(r)$ is the ionic potential, the second term is the Hartree (classical electrostatic) potential associated with $n(r)$, and v_{xc} is the so-called exchange-correlation potential. The total energy in this picture is given by

$$E_0 = -\sum_j \langle \psi_j | -\nabla^2/2 + v(r) | \psi_j \rangle + \frac{1}{2} \int dr \int dr' \frac{n(r)n(r')}{|r - r'|} + E_{xc}[n].$$

The exchange correlation energy E_{xc} is related to the potential via

$$v_{xc}(r) = \frac{\delta E_{xc}}{\delta n(r)}.$$

We also have no information, from the basic theory, about E_{xc} .

The problem is then, what is the exchange-correlation potential (or energy functional)? There is no known general solution, however various approximations are used. The most commonly used types of exchange correlation energies are:

- Local Density Approximation, where we assume that E_{xc} depends on $n(r)$ in a local way, i.e., the local density of electrons determines

the local exchange-correlation potential. This idea takes the form

$$E_{xc}^{LDA} = \int d^3r n(r) \epsilon_{xc}(n(r)) \quad (2.13)$$

where $\epsilon_{xc}(n)$ is the exchange correlation energy of an electron system at constant density n (and which has been computed and tabulated using accurate many-body methods [19]). LDA tends to work well when the density of the electron gas is nearly constant; when n is very large (so that the kinetic energy will dominate errors rather than E_{xc}); and often for the case of weak electron correlations. LDA is usually bad when we have rapidly varying $n(r)$, i.e., at the same scale as the mean electron-electron separation, when we have low density and thus electron-electron interactions dominate over the kinetic terms, or when there are strong electron correlations LDA gives poor band spectra. Throughout this thesis when we refer to LDA, we specifically mean the version developed by Perdew and Zunger. [20]

- LSDA: Is simply LDA generalized to include the effects of different spins separately in the exchange correlation potential, hence the name Local Spin Density Approximation.
- GGA: the Generalized Gradient Approximation, which as the name suggests, involves the gradient of the density and is of the form:

$$E_{xc}^{GGA} = \int d^3r n(r) \epsilon_{xc}(n(r), \nabla n(r)) \quad (2.14)$$

Within the context of this thesis, the GGA approximation is used

in the context of chapter 5, specifically the PBE version [21], as in our experience it more accurately predicts both EELS spectra and magnetic order in $\text{La}_{1-x}\text{Sr}_x\text{MnO}_3$

Pseudopotentials

Since most often for our solid-state calculations we will use Bloch states (we are mainly interested in periodic systems in this thesis), full numerical convergence of all the electronic states (core and valence) would be difficult to obtain if we simulated all the electrons. Furthermore, many of the very tightly-bound core states may not be of physical interest in our calculations. For example, a 1s state in a transition metal can be approximated as a point charge in most calculations.

Thus, when we pick an atom, we pick the states that are of most interest to us and create an atomic pseudopotential to replace the actual potential such that:

- the resulting potential that valence electrons ‘feel’ after a certain distance is the same as what they would have felt had the full calculation with all the electrons been done, and
- the resulting valence wavefunctions after a certain critical distance from the nucleus are identical to the true atomic wavefunctions of the atom.

The core-states are not included in the explicit DFT calculation that we wish to perform. In practice, they serve as screening charges around the nucleus so that the resulting pseudopotentials are smoother than the true potential. Also, there are fewer electrons needed to calculate the properties of the system making it easier to obtain physical results.

In some respects, this is one of the trickiest part of DFT calculations. It is unclear what makes a certain pseudopotential type work very well, as there are many types to choose from as well as different available open-source codes that one can use to generate them. For the calculations I have done, I have used pseudopotentials that are either from the Quantum Espresso library [22] or others that I have generated myself using the Vanderbilt Ultrasoft pseudopotential generating code [23].

Virtual Crystal Approximation (VCA)

In order to approximate alloys, such as $\text{La}_{1-x}\text{Sr}_x\text{MnO}_3$, it is very useful to have a way to represent the alloying (x) in a simple and efficient manner that does not require a very large unit cell containing the various random distribution of atoms involved. The VCA [24] is the simplest solution to this problem that one can think of: one creates pseudopotentials for the two atoms and combine them linearly. Namely, to create the virtual atom corresponding to the chemical alloying $A_{1-x}B_x$, one creates the virtual pseudopotential V_{ps}^X as

$$V_{ps}^X = (1 - x)V_{ps}^A + xV_{ps}^B. \quad (2.15)$$

Of course, an ‘average atom’ seems like a somewhat artificial idea. However, in cases where the atom being modeled through VCA does not have electronic states close to the Fermi level and is used as an electron donor as well as for its size, we’ve found that VCA [25, 26] can be a very appropriate method.

DFT+U

The DFT+U approach [27], also known as LDA+U or GGA+U depending on the type of exchange-correlation functional one uses, is a way to try and include some of the effects of local Coulombic interactions on a single atomic site with localized orbitals in a way that goes beyond the local potential of DFT for cases of open shell systems (partial occupancies of local orbitals). For example, one can aim to create an energy functional looking like

$$E_{DFT+U} = E_{DFT} + \frac{1}{2}U \sum_{i \neq j} n_i n_j \quad (2.16)$$

where the second term is the Coulomb interaction term from the Hubbard model, and n_i is the electron occupancy of localized orbital i on atom. However, assuming that the energy obtained from DFT is correct when the orbitals are either completely empty or completely full, $n_{j\sigma} \in \{0, 1\}$, one has to subtract out the contribution of this Hubbard like term to void “double counting”. This yields the following modified functional:

$$E_{DFT+U} = E_{DFT} + \frac{1}{2}U \sum_{i \neq j} n_i n_j - UN(N-1)/2 \quad (2.17)$$

where N is the total number of electrons on the site of interest. The local orbital energies are then

$$\epsilon_i = \frac{\partial E}{\partial n_i} = \epsilon_i^{DFT} + U \left(\frac{1}{2} - n_i \right) \quad (2.18)$$

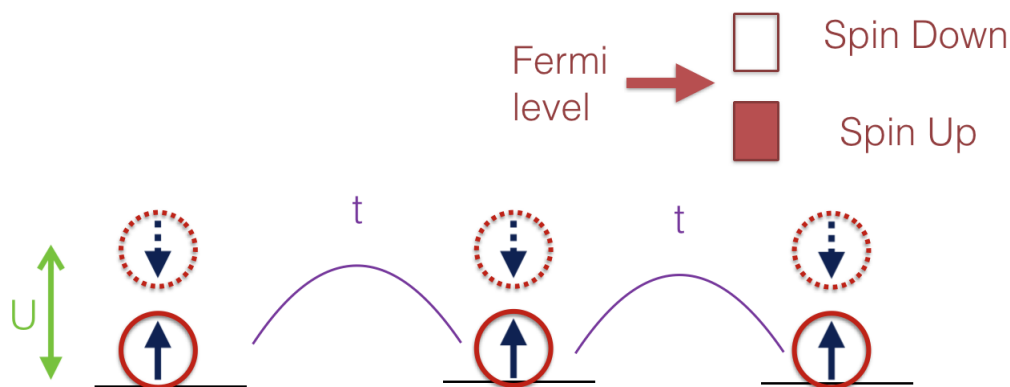


FIGURE 2.1

A correction to DFT such as DFT+U can help break symmetry and obtain a magnetically polarized solution and thus a band gap. This is illustrated here for a ferromagnetic phase of a one dimensional lattice system with nearest neighbor hoppings.

There are more complicated versions of DFT+U that include a Hund's term J [27], but we will not be using them in this thesis. From a pragmatic viewpoint, what DFT+U often does is best understood in the above local orbital energy equation: when an orbital is more than half-filled, its energy is lowered (and vice versa). A full shift of occupancy between 0 and 1 means an energy splitting of U which mimics the formation of a Hubbard band (albeit in band theory). In this way, DFT+U often exacerbates whatever tendency to occupancy differences already exists in a material. In addition, it can stabilize symmetry broken phases which will have orbitals with differing electron occupations. Figure 2.1 illustrates this point.

Wannier Functions

In many cases when we need to obtain local properties, Bloch states become inappropriate: they are, by definition, extended throughout the

crystal. In the case of calculations such as those in this thesis, the need to understand physics at a local level using correlated localized orbitals is obvious. However, atomic orbitals are not always a great option: while they are useful to understand free atoms, in the context of a solid they do not lead to an orthogonal, complete set of states.

A method to obtain a complete and orthonormal set of states (for a set of bands of interest) is to take a discrete Fourier transform of the Bloch states for each band to generate a Wannier function for that band. The method to obtain them looks deceptively simple. Pick a band n , and to obtain the value of the Wannier function at the lattice position R , just sum over all the Bloch states corresponding to that band:

$$W_{nR} = \frac{1}{\sqrt{N}} \sum_k e^{-ikR} \psi_{nk}(r). \quad (2.19)$$

It is very straightforward to prove that this transformation leads to a complete and orthonormal basis set. Furthermore, the locality effect seems obvious from this tight-binding like equation:

$$\langle W_{nR} | H | W_{n'R'} \rangle = \delta_{nn'} e_n(R - R') \quad (2.20)$$

where H is the one-particle Hamiltonian generating the Bloch states, and $e_n(R - R')$ is a function that only depends on the relative distance between the two lattice sites. This tight-binding representation would tend to make us believe the Wannier functions must be localized.

There is, unfortunately, a great deal of freedom in picking the phases

for the Fourier transform from Bloch to Wannier representation. For example,

$$W_{nR} = \frac{1}{\sqrt{N}} \sum_k e^{-ikR} \psi_{nk}(r) e^{i\theta_{nk}} \quad (2.21)$$

are an equally good set of Wannier functions for any phases θ_{nk} . In fact, for a set of bands, one can make arbitrary unitary transformations among them as well:

$$\tilde{\psi}_{nk}(r) = \sum_m \psi_{mk}(r) U_{mn}^k \quad (2.22)$$

and still get equally valid Wannier functions. Hence, Wannier functions are quite ill defined without some further constraints being imposed.

It turns out that one can pick the phases or U matrices to minimize the spatial extent of the Wannier functions. Namely, one varies the U^k matrices until the quadratic 'spread functional' is minimized:

$$\Omega = \sum_n \langle r^2 \rangle_n - \langle r \rangle_n^2 \quad (2.23)$$

These are the basics of generating Minimally Localized Wannier Functions (MLWF) [28]. As it turns out, MLWFs tend to look quite like atomic orbitals with some added features from nearby orbitals to ensure orthonormality (for example, the Mn Wannier d orbitals will have some character from the O 2p orbitals from the nearby oxygen atoms in an oxide of Mn).

There are many uses of Wannier functions [29]. The main reason we will use them is to obtain the physical parameters for tight-binding models that will then be modified to include local interactions. We pick bands of interest, usually the ones near the Fermi level, and use models based on their Wannier functions to find hopping parameters for Hubbard-like

models.

From the above description, Wannier functions seem like an ideal basis set. But, in practice, they may be difficult to generate or work with. For example, in calculations involving complex heterostructures, it can be near impossible to isolate the bands of physical interest from other bands at the same energies. This especially true in cases where, for computational reasons, we must include an explicit electrode in the simulation cell: most of the bands near the Fermi level will belong to the electrode, and separating them from the relevant transition metal d states can be very difficult. Furthermore, selecting the energy ranges of interest involves some art, intuition, and luck. If one picks a range that is too small, the bands may be cut off and incomplete. If one picks a range that is too large, the MLWF will lose their intended meaning as the most localized states the computer will obtain will asymptotically tend to delta functions.

O-K Edges in Electron Energy Loss Spectroscopy

Electron Energy Loss Spectroscopy (EELS) is one of the few experimental tools that provides information about the local electronic structure in real space at the atomic scale. High speed electrons (keV) are shot through a material and their loss of kinetic energy is measured upon exiting the sample. To get chemically specific information that is spatially local, one uses a narrow electron beam and looks at high energy electron loss processes involving transitions from core states to valence states on specific chemical species, and each atom has a unique “fingerprint” in terms of the energy ranges for its core-valence transitions.

We focus on the oxygen K-edge corresponding to the oxygen $1s \rightarrow 2p$ transition (approximately at 530 eV [30, 31]). The matrix element on the O atom involved for a process with momentum transfer k is

$$\langle 1s | e^{ik \cdot r} | 2p \rangle \approx \langle 1s | 2p \rangle + \langle 1s | ikr | 2p \rangle \quad (2.24)$$

The first term is zero since $1s$ and $2p$ are orthogonal, and the second term is a dipole transition. We generally stop at the dipole level since the $1s$ state is extremely localized so the range of r variation in the inner product is small. In a crystal, the Bloch states have amplitudes on all atomic states including the O $2p$ states, so a transition from O $1s$ to a Bloch state labeled by n, k at energy E will have rate given by

$$\begin{aligned} T_{1s \rightarrow n,k}(E) &\propto \sum_{n,k} |\langle n, k | 2p \rangle|^2 \delta(E - E_{n,k}) \theta(E_{n,k} - E_F) \\ &= \theta(E - E_F) PDOS_{2p}(E) \end{aligned} \quad (2.25)$$

where $PDOS_{2p}$ is the projected density of states on the $2p$ states and the zero of E is at $E_F - E_{1s}$ (the lowest transition energy possible). We have assumed here that the transition dipole matrix elements is energy independent so it does not appear inside the sum. Since in a typical oxide the O has a closed shell (formal charge of -2), T will be nonzero only due to hybridization of O $2p$ to nearly cation states and the O-K edge describes the local electronic and chemical environment of the O atom in question.

The Z and Z+1 Approximation for EELS

Although DFT, in principle, can not describe excited states involved in EELS, in practice it has proven quite effective in the study of EELS spectra in many materials [30–32]. Physically, when the core hole is created, the electronic system requires some time to respond and screen the positive charge of the core hole. Separately, various materials have different effectiveness at screening of electrostatic perturbations. In situations where the screening is very localized and strong, one may disregard the effect the core hole has on the electrons and simply compute the transition rate with the unperturbed ground state electronic wave functions: this is the so called “Z approximation.” The opposite limit (the “final state” approximation) is to permit the electrons to completely adjust to the core hole and screen it statically (“Z+1 approximation”). In order to model the core hole on the Oxygen atom, the standard method is to generate a pseudopotential in which the core hole is manually added to the Oxygen 1s state. Thus, when screening is stronger (for example in metallic systems such as Al), Z is a more appropriate approximation, while for insulators Z+1 is better. For the manganite systems we are interested in in chapter 5, the Z+1 approximation has proven itself appropriate in the literature.[30, 31]

We note that Kohn-Sham states are single-particle effective electronic states used to solve the many-body Hamiltonian in some indirect manner. It is not clear at all whether using them to compute O-K edge excitation spectra is a sensible procedure. Again, in practice, a great deal of physical information is generated by this procedure and often good agreement with experiment is possible.

There are, of course, many shortcomings of the approach we have used. We have ignored multipole effects in the transition matrix element, we have ignored its energy dependence, we have not allowed for multiple scattering processes, and our description of the many-body excited state is still at a single-particle level.

Chapter 3

A Generalized Slave-Particle Method For Extended Hubbard Models

One of the long-standing areas of interest in condensed matter physics, particularly that of complex oxides, is that of the Mott metal-insulator transition [33]. Generically, within a Hubbard model framework, as the strength of localized electronic repulsions is increased, the electrons prefer to be localized on atomic sites and inter-site hopping is suppressed, and at a critical interaction strength the system becomes an insulator. An example of the rich behavior that can occur in such systems is the Orbital Selective Mott Transition (OSMT) whereby only a subset of localized orbitals become insulating (localized) while the remainder have metallic (extended) bands. An example is provided by quasi-two-dimensional Mott transition in the $\text{Ca}_{2-x}\text{Sr}_x\text{RuO}_4$ family, where the Mott metal-insulator transition and its magnetic properties [34] at the critical doping $x = 0.5$ show a coexistence between magnetic susceptibility that shows a Curie form for $S = 1/2$ and a metallic state. Anisimov *et al.* [35] have used

DFT+DMFT to explain this situation in terms of an OSMT in which one Ru $4d$ orbital is localized, while the other continues to present metallic behavior.

The present day workhorse for *ab initio* materials modeling and prediction, Density Functional Theory (DFT), is fundamentally based on band theory and is unable to describe such transitions (without symmetry breaking of the electronic degrees of freedom: e.g., spin or orbital polarization). To this end, Hubbard model based methods such as Dynamical Mean Field Theory (DMFT) and DFT+DMFT [11, 36] have been developed to include localized correlation effects in electronic structure calculations. However, DMFT-based methods are computationally expensive and typical present day calculations on real materials are generally restricted to treating a few correlated sites. Therefore, it is of significant interest to have computationally inexpensive, but necessarily more approximate, methods that include correlations and can permit one to rapidly explore the qualitative effects of electronic correlations.

One set of such approximate methods that have been of recent interest are slave-particle methods. Slave-boson methods have a long background in condensed matter theory for analytical treatments of correlations typically in the limiting case of infinite correlation strength [5, 7, 37–41]. Kotliar and Ruckenstein [7] used a slave-particle representation to treat Hubbard-like models at finite interaction strength, which found applications in the realm of high-temperature superconductors [42]. Further, Kotliar and Ruckenstein’s model has been generalized to multi-band models [43–45] where, e.g., the effects of multiple orbitals, orbital degeneracy, and the Hund’s have been studied [43, 44]. However,

the approach of Kotliar and Ruckenstein, and its various extensions, require a large number of bosonic slave particles: one needs one boson per possible electronic configuration on a correlated site.

For this reason, more economical slave-boson representations have been of significant interest. Florens and Georges [8, 9] used a single “rotor” slave-boson per site that describes the total electron count on each site in a computationally economical manner. The slave-rotor method was been successfully to predict a number of electronic phases of nickelate heterostructures [46] which was a distinct improvement over previous studies. However, a rotor-like description is not orbitally selective as it can only describe the total electron count on a site and not its partitioning among inequivalent orbitals on that site. An alternative slave-particle approach is to treat each localized electronic state (i.e., a unique combination of spin and orbital indices) with a slave boson: this “slave-spin” approach automatically handles orbital symmetry breaking and can predict OSMTs [15, 16]. Recently, it has been applied to predict key physical characteristics in iron superconductors [47].

In this chapter, we introduce a generalized framework for slave-particle descriptions. This produces a ladder of correlated models, and the slave-rotor and slave-spin are automatically included as two specific cases. Our approach does not require any physical analogies to create the slave bosons (e.g., a quantum rotor or angular variable to motivate the slave-rotor or a pseudo-spin to motive the slave-spin) and works directly in the occupation number representation. In our approach, one can choose which degrees of freedom are treated as correlated degrees of freedom

(e.g., total electron count on a site, electron counts in each orbital, electron count in each spin channel, etc.) so that we can isolate the effect of correlations on the separate degrees of freedom in a systematic manner. Section 3.1 presents our general formalism, how it builds upon previous models, as well as gives a few examples of models that can be built within this framework. Section 3.2 is devoted to tests of possible models built within this formalism in a mean-field approach at half-filling within a one-band and a two-band model in order to compare our results with those of previous work as well as to better understand the role of the different terms in an extended Hubbard model within our formalism. In Section 4.7 we conclude this paper and discuss possible new avenues for researchers to use this method and possible developments of it in predicting properties of correlated materials.

3.1 The Generalized Slave-Particle Representation

In this section we introduce our generalized slave-particle representation. In appropriate limits, our approach reproduces previous frameworks such as the slave-rotor and slave-spin methods. One utility of our approach is that it allows us to unite these two, as well as other intermediate models, into a single slave-particle methodology. A variety of slaves-particle models can be investigated and compared so that one can isolate which specific correlated degrees of freedom are critical for describing a specific physical problem.

The general correlated-electron Hamiltonian we consider is an extended Hubbard model given by

$$\hat{H} = \sum_i \hat{H}_{int}^i + \sum_{im\sigma} \epsilon_{im\sigma} \hat{d}_{im\sigma}^\dagger \hat{d}_{im\sigma} - \sum_{i'i'm'\sigma} t_{im'i'm'\sigma} \hat{d}_{im\sigma}^\dagger \hat{d}_{i'm'\sigma}. \quad (3.1)$$

The index i ranges over the localized sites of the system (usually atomic sites), m ranges over the localized spatial orbitals on each site, σ denotes spin, \hat{H}_{int}^i is the local Coulombic interaction for site i detailed further below, $\epsilon_{im\sigma}$ is the onsite energy of the orbital $im\sigma$, and $t_{im'i'm'\sigma}$ is the spin-conserving hopping element term connecting orbital $im\sigma$ to $i'm'\sigma$. The \hat{d} are canonical fermion annihilation operators. We take the interaction term to have the standard Slater-Kanamori form [48]

$$\begin{aligned} \hat{H}_{int}^i = & \frac{U_i}{2} (\hat{n}_i^2 - \hat{n}_i) + \frac{U'_i - U_i}{2} \sum_{m \neq m'} \hat{n}_{im} \hat{n}_{im'} - \frac{J_i}{2} \sum_{\sigma} \sum_{m \neq m'} \hat{n}_{im\sigma} \hat{n}_{im'\sigma} \\ & - \frac{J_i}{2} \sum_{\sigma} \sum_{m \neq m'} \left\{ \hat{d}_{im\sigma}^\dagger \hat{d}_{im\bar{\sigma}} \hat{d}_{im'\bar{\sigma}}^\dagger \hat{d}_{im'\sigma} + \hat{d}_{im\sigma}^\dagger \hat{d}_{im\bar{\sigma}}^\dagger \hat{d}_{im'\sigma} \hat{d}_{im'\bar{\sigma}} \right\}. \quad (3.2) \end{aligned}$$

The first and second term stem from Coulombic repulsion terms between same spatial orbital (U) and different spatial orbitals (U'). The third term is Hund's exchange between different orbitals of the same spin with strength J . The fourth term contains the intrasite "spin flip" and "pair hopping" terms. The index $\bar{\sigma}$ is the spin opposite to σ . The subscripts i on the U, U' and J parameters denote the fact that each correlated site can have its own set of parameters; however, to keep indices to a minimum

below, we suppress this index. The various number operators are

$$\begin{aligned}\hat{n}_{im\sigma} &= \hat{d}_{im\sigma}^\dagger \hat{d}_{im\sigma} \quad , \quad \hat{n}_{im} = \sum_{\sigma} \hat{n}_{im\sigma} \\ \hat{n}_{i\sigma} &= \sum_m \hat{n}_{im\sigma} \quad , \quad \hat{n}_i = \sum_{m\sigma} \hat{n}_{im\sigma} .\end{aligned}$$

For what follows, we keep in mind that due to the fact that $\hat{n}_{im\sigma}^2 = \hat{n}_{im\sigma}$, the Hund's term in \hat{H}_{int}^i can be rewritten in an equivalent form to give

$$\begin{aligned}\hat{H}_{int}^i &= \frac{U_i}{2} (\hat{n}_i^2 - \hat{n}_i) + \frac{U'_i - U_i}{2} \sum_{m \neq m'} \hat{n}_{im} \hat{n}_{im'} - \frac{J_i}{2} \sum_{\sigma} (\hat{n}_{i\sigma}^2 - \hat{n}_{i\sigma})^2 \\ &\quad - \frac{J_i}{2} \sum_{\sigma} \sum_{m \neq m'} \left\{ \hat{d}_{im\sigma}^\dagger \hat{d}_{im\bar{\sigma}} \hat{d}_{im'\bar{\sigma}}^\dagger \hat{d}_{im'\sigma} + \hat{d}_{im\sigma}^\dagger \hat{d}_{im\bar{\sigma}}^\dagger \hat{d}_{im'\sigma} \hat{d}_{im'\bar{\sigma}} \right\} .\end{aligned}$$

The interacting Hubbard hamiltonian is impossible to solve exactly and even difficult to solve approximately. Part of the difficulty comes from the fact that we have interacting fermions which have both charge and spin degrees of freedom. Following well-known ideas in slave-boson approaches [5, 7, 37–41], one separates at each site the fermionic degrees of freedom from the charge degrees of freedom by introducing a bosonic “slave” particle on that site. The boson is spinless and charged, and one also has a remaining neutral fermion with spin termed a spinon. With spinons denoted by \hat{f} operators and slave bosons by \hat{O} operators, we define

$$\hat{d}_{im\sigma} = \hat{f}_{im\sigma} \hat{O}_{i\alpha} \quad (3.3)$$

and

$$\hat{d}_{im\sigma}^\dagger = \hat{f}_{im\sigma}^\dagger \hat{O}_{i\alpha}^\dagger . \quad (3.4)$$

The index α is part of our generalized notation that permits us to unify many slave-particle models. The meaning of α depends on the type of

model chosen, as we will show in detail below with a variety of examples. The index α refers to a subset of the $m\sigma$ indices that belong to a site i . For example, if we use a slave-rotor model for the correlated orbitals on a site [8, 9], then α is nil: $\hat{O}_{i\alpha} = \hat{O}_i$. Namely, we have a single slave particle on each site i that tracks the total number of particles on that site. At the opposite limit, we can have a unique slave boson for each $m\sigma$ (the “slave-spin” method [15, 16]), so that $\alpha = m\sigma$.

Since we have introduced new degrees of freedom and enlarged the Hilbert space, it is necessary to avoid unphysical states that have no correspondence to those in the original problem. As Eqs. (4.3) and (3.4) show, the number of spinon and slave particles track each other because they are annihilated and created at the same time. Thus, one must enforce the operator constraints

$$\hat{d}_{im\sigma}^\dagger \hat{d}_{im\sigma} = \hat{f}_{im\sigma}^\dagger \hat{f}_{im\sigma} \quad (3.5)$$

and

$$\sum_{m\sigma \in \alpha} \hat{f}_{im\sigma}^\dagger \hat{f}_{im\sigma} = \hat{N}_{i\alpha} \quad (3.6)$$

where $\hat{N}_{i\alpha}$ is the number operator for the slave particles which takes on integer values from N_{min} to N_{max} , i.e., in the number representation we have

$$\hat{N}_{i\alpha} = \text{diag} (N_{min}, N_{min} + 1, \dots, N_{max} - 1, N_{max}). \quad (3.7)$$

The appropriate values of N_{min} and N_{max} depend on the slave model chosen and are discussed below. Enforcing the operator constraints of Eq. (3.6) at all times ensure that only physical states in one-to-one correspondence to the original states are considered in the extended spinon+slave boson Hilbert space.

To reproduce the standard behavior of the annihilation operator [15, 16]

$$\hat{d}_{im\sigma}|n_{im\sigma}\rangle = \sqrt{n_{im\sigma}}|n_{im\sigma} - 1\rangle$$

it must be that

$$\hat{f}_{im\sigma}|n_{im\sigma}\rangle = \sqrt{n_{im\sigma}}|n_{im\sigma} - 1\rangle$$

and

$$\hat{O}_{i\alpha}|N_{i\alpha}\rangle = |N_{i\alpha} - 1\rangle.$$

However, if $n_{im\sigma} = 0$, then the action of $\hat{f}_{im\sigma}$ will destroy the state regardless of what \hat{O}_α may do, so for this case we have an undetermined situation:

$$\hat{O}_{i\alpha}|N_{i\alpha} = 0\rangle = \text{undetermined}.$$

Following the same logic for the creation operators yields

$$\hat{O}_{i\alpha}^\dagger|N_{i\alpha}\rangle = |N_{i\alpha} + 1\rangle$$

unless we reach the ceiling $N_{i\alpha} = N_{max}$ when we have a similar indeterminacy

$$\hat{O}_{i\alpha}^\dagger|N_{max}\rangle = \text{undetermined}.$$

Putting this all together, the slave boson operator $\hat{O}_{i\alpha}$ in the number basis must have the form

$$\hat{O}_{i\alpha} = \begin{pmatrix} 0 & 1 & 0 & \dots & 0 & 0 \\ 0 & 0 & 1 & \dots & 0 & 0 \\ \vdots & \vdots & \vdots & \ddots & \vdots & \vdots \\ 0 & 0 & 0 & \dots & 1 & 0 \\ 0 & 0 & 0 & \dots & 0 & 1 \\ C_{i\alpha} & 0 & 0 & \dots & 0 & 0 \end{pmatrix} \quad (3.8)$$

where $C_{i\alpha}$ is at this point an undetermined constant that we are free to choose. Below, we will use this freedom to ensure that we reproduce a desired non-interacting band structure at zero interaction strength (when $\hat{H}_{int}^i = 0$).

We note that we may decide to allow for additional unphysical states with negative or positive occupations. For example, letting $N_{min} \rightarrow -\infty$ and $N_{max} \rightarrow +\infty$, which in turn makes $C_{i\alpha}$ irrelevant, yields the slave-rotor formalism [8, 9]. On the other hand, a separate slave boson for each spin+orbital combination $im\sigma$ gives $N_{min} = 0$ and $N_{max} = 1$ which recovers the “slave-spin” formalism [15, 16].

Substituting the spinon and slave operators into the original extended Hubbard Hamiltonian gives the following form, which for the moment we specialize to the symmetric $U' = U, J = 0$ case to keep the logic simple

(the more general cases are enumerated further below):

$$\begin{aligned} \hat{H} = \frac{U}{2} \sum_i \left(\left(\sum_{\alpha} \hat{N}_{i\alpha} \right)^2 - \sum_{\alpha} \hat{N}_{i\alpha} \right) \\ + \sum_{im\sigma} \epsilon_{im\sigma} \hat{f}_{im\sigma}^{\dagger} \hat{f}_{im\sigma} \\ - \sum_{ii'mm'\sigma} t_{imim'\sigma} \hat{O}_{i\alpha}^{\dagger} \hat{O}_{i'\alpha'} \hat{f}_{im\sigma}^{\dagger} \hat{f}_{i'm'\sigma} . \end{aligned}$$

For the onsite $\epsilon_{im\sigma}$ terms, we have replaced $\hat{f}_{im\sigma}^{\dagger} \hat{f}_{im\sigma} \hat{O}_{i\alpha}^{\dagger} \hat{O}_{i\alpha}$ by the simpler $\hat{f}_{im\sigma}^{\dagger} \hat{f}_{im\sigma}$ because even though $\hat{O}_{i\alpha}^{\dagger} \hat{O}_{i\alpha}$ is not necessarily identity (unless $C_{i\alpha} = 1$), the two set of operators act identically on all the physical states of interest (because $\hat{f}_{im\sigma}$ annihilates the state with zero particles). The important point is that the introduction of the slave bosons permits us to write the interaction term only in terms of the slave operators.

The above Hamiltonian is still an interacting one and thus impossible to solve. In slave-particle approaches, one splits this problem into two separate problems connected to each other via averaging of the relevant operators. Namely, we approximate the ground state wave function of the original system by a product state $|\Psi_f\rangle|\Phi_s\rangle$ where $|\Psi_f\rangle$ is the collective spinon state and $|\Phi_s\rangle$ is the collective slave boson state. The operator constraints of Eq. (3.6) are replaced by their average number constraints

$$\left\langle \sum_{m\sigma \in \alpha} \hat{f}_{im\sigma}^{\dagger} \hat{f}_{im\sigma} \right\rangle_f = \langle \hat{N}_{i\alpha} \rangle_s \quad (3.9)$$

where the f and s subscripts denote averaging over the spinon $|\Psi_f\rangle$ and slave boson $|\Phi_s\rangle$ ground state wave functions, respectively.

With this separability assumption, the time-independent Schrödinger equation for the original system separates into two separate equations where the constraints are enforced by Lagrange multipliers appearing in

the two Hamiltonians. The spinon Hamiltonian is

$$\begin{aligned} \hat{H}_f = \sum_{im\sigma} \epsilon_{im\sigma} \hat{f}_{im\sigma}^\dagger \hat{f}_{im\sigma} - \sum_{i\alpha} h_{i\alpha} \sum_{m\sigma \in \alpha} \hat{f}_{im\sigma}^\dagger \hat{f}_{im\sigma} \\ - \sum_{ii'\alpha\alpha'} \langle \hat{O}_{i\alpha}^\dagger \hat{O}_{i'\alpha'} \rangle_s \sum_{\substack{m\sigma \in \alpha \\ m'\sigma' \in \alpha'}} t_{imim'\sigma} \hat{f}_{im\sigma}^\dagger \hat{f}_{i'm'\sigma'} \end{aligned} \quad (3.10)$$

where $h_{i\alpha}$ is the Lagrange multiplier enforcing Eq. (3.9). The spinons are coupled to the slave bosons via the average $\langle \hat{O}_{i\alpha}^\dagger \hat{O}_{i'\alpha'} \rangle_s$ which renormalizes spinon hoppings between sites i and i' . The spinon problem is one of non-interacting fermionic particles with spin.

The slave boson Hamiltonian takes the form

$$\begin{aligned} \hat{H}_s = \frac{U}{2} \sum_i \left(\left(\sum_\alpha \hat{N}_{i\alpha} \right)^2 - \sum_\alpha \hat{N}_{i\alpha} \right) + \sum_\alpha h_{i\alpha} \hat{N}_{i\alpha} \\ - \sum_{ii'\alpha\alpha'} \left[\sum_{\substack{m\sigma \in \alpha \\ m'\sigma' \in \alpha'}} t_{imim'\sigma} \langle \hat{f}_{im\sigma}^\dagger \hat{f}_{i'm'\sigma'} \rangle_f \right] \hat{O}_{i\alpha}^\dagger \hat{O}_{i'\alpha'} \end{aligned} \quad (3.11)$$

where the spinon average $\langle \hat{f}_{im\sigma}^\dagger \hat{f}_{i'm'\sigma'} \rangle_f$ renormalizes the slave boson hoppings. The slave boson problem is one of interacting charged bosons without spin.

The original problem has been reduced to a set of paired problems that must be solved self-consistently. The spinon and slave boson problems only communicate (i.e., are coupled) via averages which renormalize each other's hoppings. At this point, one must make some approximations in order to solve the interacting bosonic problem. Typical approaches to date include single-site mean field approximations [8, 9], multiple-site mean field [49], approximation by sigma models to yield

Gaussian integrals [8, 9] as well as a combination of using tight-binding parameters obtained using Wannier functions from DFT followed by a mean-field approximation [46].

The procedure to obtain the required $C_{i\alpha}$ in order to solve the coupled problems is as follows. At $U = U' = J = 0$, one ensures that the spinons reproduce the original non-interacting band structure and pre-specified site occupancies (i.e., fillings). This means that the slave-boson expectations $\langle O_{i\alpha}^\dagger O_{i'\alpha'} \rangle_s$ should be unity in order not to modify the spinon hoppings away from the original hoppings. The numbers $C_{i\alpha}$ and $h_{i\alpha}$ are determined by these condition as well as the prespecified non-interacting site occupancies. This requires us to solve the coupled slave and spinon problems at $U = U' = J = 0$ self-consistently to obtain $C_{i\alpha}$ and $h_{i\alpha}$. The values of $C_{i\alpha}$ are then held fixed from that point forward. Finally, we can turn on U, U', J to non-zero values to self-consistently solve the desired interacting problem.

Prior to solving some model problems within our new framework, we first provide more complete descriptions of a number of potential choices for the slave-boson model (i.e., the choice of α). Differing choices split the interaction terms \hat{H}_{int}^i of Eq. (3.2) in different ways between the spinon and slave sectors. This opens the door to systematic comparison between the different types of treatments of correlations with the slave bosons.

3.1.1 Number slave

The simplest approach is to simply create a single slave boson on each site i whose number operator \hat{N}_i counts all the electrons on that site.

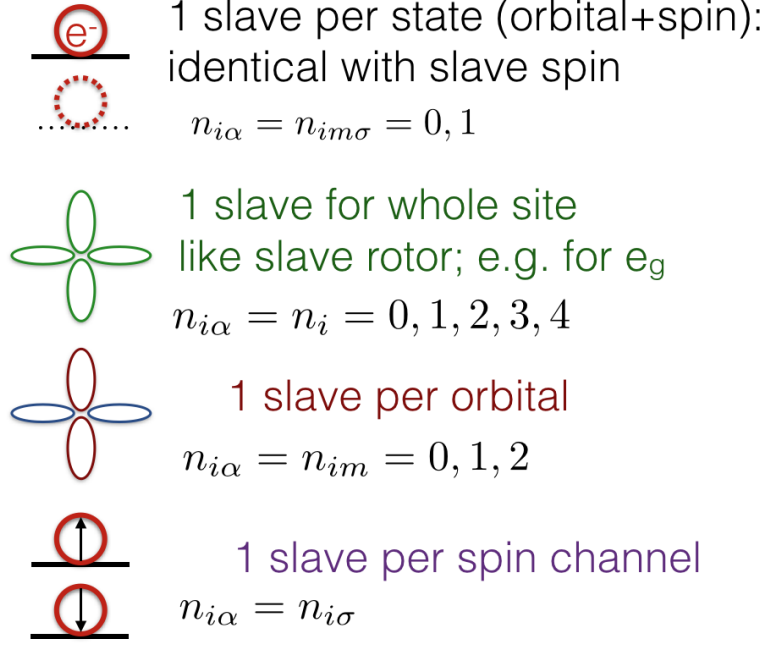


FIGURE 3.1: Visual representation of a few possible slave-particle models within our formalism.

In other words, the label α contains all the $m\sigma$ orbitals on that site and thus is superfluous so we can simply write $\hat{O}_{i\alpha} = \hat{O}_i$. Description of the physically allowed states requires $N_{min} = 0$ while N_{max} will be the maximum number of electrons allowed on that site: e.g., 10 for d shells or 14 for f shells.

In this case, the slave boson can only represent the U term of the interaction in Eq. (3.2) so that all remaining interaction terms must be treated at the mean-field level in the spinon sector. Thus the slave Hamiltonian in this case is

$$\hat{H}_s = \frac{U}{2} \sum_i (\hat{N}_i^2 - \hat{N}_i) + \sum_i h_i \hat{N}_i - \sum_{ii'} \left[\sum_{mm'\sigma} t_{imim'\sigma} \langle \hat{f}_{im\sigma}^\dagger \hat{f}_{i'm'\sigma} \rangle_f \right] \hat{O}_i^\dagger \hat{O}_{i'} \quad (3.12)$$

while the spinon Hamiltonian contains all the remaining interaction terms at mean-field level:

$$\begin{aligned}
\hat{H}_f = & \frac{U' - U}{2} \sum_i \sum_{m \neq m'} \left(n_{im} \hat{n}_{im'} + n_{im'} \hat{n}_{im} \right. \\
& - \sum_{\sigma \sigma'} \left\{ \rho_{im'\sigma'im\sigma} \hat{f}_{im'\sigma'}^\dagger \hat{f}_{im\sigma} + \rho_{im\sigma im'\sigma'} \hat{f}_{im\sigma}^\dagger \hat{f}_{im'\sigma'} \right\} \Big) \\
& - \frac{J}{2} \sum_{i\sigma} \sum_{m \neq m'} \left(n_{im\sigma} \hat{n}_{im'\sigma} + n_{im'\sigma} \hat{n}_{im\sigma} \right. \\
& - \rho_{im'\sigma'im\sigma} \hat{f}_{im'\sigma'}^\dagger \hat{f}_{im\sigma} - \rho_{im\sigma im'\sigma'} \hat{f}_{im\sigma}^\dagger \hat{f}_{im'\sigma'} \Big) \\
& - \frac{J}{2} \sum_{i\sigma} \sum_{m \neq m'} \left(\rho_{im\bar{\sigma} im'\sigma} \hat{f}_{im'\bar{\sigma}}^\dagger \hat{f}_{im'\sigma} + \rho_{im'\sigma im'\bar{\sigma}} \hat{f}_{im\sigma}^\dagger \hat{f}_{im\bar{\sigma}} \right. \\
& - \rho_{im'\sigma im\sigma} \hat{f}_{im'\bar{\sigma}}^\dagger \hat{f}_{im\bar{\sigma}} - \rho_{im\bar{\sigma} im'\sigma} \hat{f}_{im\sigma}^\dagger \hat{f}_{im'\sigma} \\
& + \rho_{im'\bar{\sigma} im\sigma} \hat{f}_{im\bar{\sigma}}^\dagger \hat{f}_{im'\sigma} + \rho_{im'\sigma im\bar{\sigma}} \hat{f}_{im\sigma}^\dagger \hat{f}_{im'\bar{\sigma}} \\
& \left. - \rho_{im'\sigma im\sigma} \hat{f}_{im\bar{\sigma}}^\dagger \hat{f}_{im'\bar{\sigma}} - \rho_{im'\bar{\sigma} im\sigma} \hat{f}_{im\sigma}^\dagger \hat{f}_{im'\sigma} \right) \\
& + \sum_{im\sigma} \epsilon_{im\sigma} \hat{f}_{im\sigma}^\dagger \hat{f}_{im\sigma} - \sum_i h_i \hat{n}_i \\
& - \sum_{ii'} \langle \hat{O}_i^\dagger \hat{O}_{i'} \rangle_s \sum_{mm'\sigma} t_{im'i'm'\sigma} \hat{f}_{im\sigma}^\dagger \hat{f}_{i'm'\sigma}. \quad (3.13)
\end{aligned}$$

In the derivation of the expression for the above spinon Hamiltonian \hat{H}_f , we have used the definition of the one-particle density matrix

$$\rho_{ba} = \langle \hat{f}_a^\dagger \hat{f}_b \rangle_f,$$

the standard mean-field contraction of four particle operators into two-particle operators weighed by averages

$$\hat{f}_a^\dagger \hat{f}_b^\dagger \hat{f}_c \hat{f}_d \approx \rho_{da} \hat{f}_b^\dagger \hat{f}_c - \rho_{ca} \hat{f}_b^\dagger \hat{f}_d + \rho_{cb} \hat{f}_a^\dagger \hat{f}_d - \rho_{db} \hat{f}_a^\dagger \hat{f}_c,$$

and the average occupations

$$n_{im\sigma} = \rho_{im\sigma im\sigma} \quad , \quad n_{im} = \sum_{\sigma} n_{im\sigma} .$$

This approach has the simplest slave Hamiltonian and the most complex spinon Hamiltonian because the number-only slave boson can only describe the simplest U part of the interaction; the remaining terms involving U' and J must be handled at mean-field level by the spinons. As mentioned above, the physical range for the occupation numbers of the number slave \hat{N}_i is from zero to the physically allowed N_{max} for that site. However, we can decrease N_{min} below zero and N_{max} above the physical value if desired; in the limit where the range of occupancies allowed is very large we automatically recover the slave-rotor method.

3.1.2 Orbital slave

A more fine-grained model is to count the number of electrons in each spatial orbital m separately with a slave boson. We call this the orbital slave method. Here the index α labels a specific spatial orbital m and ranges over the two spin directions for that orbital: we have \hat{O}_{im} for the raising/lowering operator and \hat{N}_{im} for the particle count slave operators.

The slave sector can now directly describe more of the interaction terms:

$$\begin{aligned}
\hat{H}_s = & \frac{U}{2} \sum_i \left(\left(\sum_m \hat{N}_{im} \right)^2 - \sum_m \hat{N}_{im} \right) \\
& + \frac{U' - U}{2} \sum_i \sum_{m \neq m'} \hat{N}_{im} \hat{N}_{im'} + \sum_i \sum_m h_{im} \hat{N}_{im} \\
& - \sum_{ii'mm'} \left[\sum_{\sigma} t_{imim'\sigma} \langle \hat{f}_{im\sigma}^{\dagger} \hat{f}_{i'm'\sigma} \rangle_f \right] \hat{O}_{im}^{\dagger} \hat{O}_{i'm'} \quad (3.14)
\end{aligned}$$

and the spinon Hamiltonian is less complex than the previous case as it only has the J terms (at mean-field level):

$$\begin{aligned}
\hat{H}_f = & -\frac{J}{2} \sum_{i\sigma} \sum_{m \neq m'} \left(n_{im\sigma} \hat{n}_{im'\sigma} + n_{im'\sigma} \hat{n}_{im\sigma} \right. \\
& \left. - \rho_{im'\sigma im\sigma} \hat{f}_{im'\sigma}^{\dagger} \hat{f}_{im\sigma} - \rho_{im\sigma im'\sigma} \hat{f}_{im\sigma}^{\dagger} \hat{f}_{im'\sigma} \right) \\
& - \frac{J}{2} \sum_{i\sigma} \sum_{m \neq m'} \left(\rho_{im\bar{\sigma} im\sigma} \hat{f}_{im'\bar{\sigma}}^{\dagger} \hat{f}_{im'\sigma} + \rho_{im'\sigma im'\bar{\sigma}} \hat{f}_{im\sigma}^{\dagger} \hat{f}_{im\bar{\sigma}} \right. \\
& \left. - \rho_{im'\sigma im\sigma} \hat{f}_{im'\bar{\sigma}}^{\dagger} \hat{f}_{im\bar{\sigma}} - \rho_{im\bar{\sigma} im'\bar{\sigma}} \hat{f}_{im\sigma}^{\dagger} \hat{f}_{im'\sigma} \right. \\
& \left. + \rho_{im'\bar{\sigma} im\sigma} \hat{f}_{im\bar{\sigma}}^{\dagger} \hat{f}_{im'\sigma} + \rho_{im'\sigma im\bar{\sigma}} \hat{f}_{im\sigma}^{\dagger} \hat{f}_{im'\bar{\sigma}} \right. \\
& \left. - \rho_{im'\sigma im\sigma} \hat{f}_{im\bar{\sigma}}^{\dagger} \hat{f}_{im'\bar{\sigma}} - \rho_{im'\bar{\sigma} im\bar{\sigma}} \hat{f}_{im\sigma}^{\dagger} \hat{f}_{im'\sigma} \right) \\
& + \sum_{im\sigma} \epsilon_{im\sigma} \hat{f}_{im\sigma}^{\dagger} \hat{f}_{im\sigma} - \sum_i \sum_m h_{im} \hat{n}_{im} \\
& - \sum_{ii'mm'} \langle \hat{O}_{im}^{\dagger} \hat{O}_{i'm'} \rangle_s \sum_{\sigma} t_{imim'\sigma} \hat{f}_{im\sigma}^{\dagger} \hat{f}_{i'm'\sigma} \cdot \quad (3.15)
\end{aligned}$$

3.1.3 Spin slave

An alternative fine-graining beyond the number slave is to have two slave bosons per site that count spin up and spin down electrons separately but with no orbital differentiation. Namely, α labels a spin state

σ but ranges over all spatial orbitals. Hence, we have $\hat{O}_{i\sigma}$ and $\hat{N}_{i\sigma}$ for our slave operators. The slave-boson Hamiltonian is

$$\begin{aligned} \hat{H}_s = & \frac{U}{2} \sum_i \left(\left(\sum_{\sigma} \hat{N}_{i\sigma} \right)^2 - \sum_{\sigma} \hat{N}_{i\sigma} \right) - \frac{J}{2} \sum_{\sigma} \left(\hat{N}_{i\sigma}^2 - \hat{N}_{i\sigma} \right) \\ & + \sum_i \sum_{\sigma} h_{i\sigma} \hat{N}_{i\sigma} - \sum_{ii'\sigma} \left[\sum_{mm'} t_{imim'\sigma} \langle \hat{f}_{im\sigma}^{\dagger} \hat{f}_{i'm'\sigma} \rangle_f \right] \hat{O}_{i\sigma}^{\dagger} \hat{O}_{i'\sigma} \quad (3.16) \end{aligned}$$

while the spinon Hamiltonian is

$$\begin{aligned} \hat{H}_f = & \frac{U' - U}{2} \sum_i \sum_{m \neq m'} \left(n_{im} \hat{n}_{im'} + n_{im'} \hat{n}_{im} \right. \\ & - \sum_{\sigma\sigma'} \left\{ \rho_{im'\sigma'im\sigma} \hat{f}_{im'\sigma'}^{\dagger} \hat{f}_{im\sigma} + \rho_{im\sigma im'\sigma'} \hat{f}_{im\sigma}^{\dagger} \hat{f}_{im'\sigma'} \right\} \\ & - \frac{J}{2} \sum_{i\sigma} \sum_{m \neq m'} \left(\rho_{im\bar{\sigma} im\sigma} \hat{f}_{im'\bar{\sigma}}^{\dagger} \hat{f}_{im'\sigma} + \rho_{im'\sigma im'\bar{\sigma}} \hat{f}_{im\sigma}^{\dagger} \hat{f}_{im\bar{\sigma}} \right. \\ & \quad - \rho_{im'\sigma im\sigma} \hat{f}_{im'\bar{\sigma}}^{\dagger} \hat{f}_{im\bar{\sigma}} - \rho_{im\bar{\sigma} im'\bar{\sigma}} \hat{f}_{im\sigma}^{\dagger} \hat{f}_{im'\sigma} \\ & \quad + \rho_{im'\bar{\sigma} im\sigma} \hat{f}_{im\bar{\sigma}}^{\dagger} \hat{f}_{im'\sigma} + \rho_{im\sigma im'\bar{\sigma}} \hat{f}_{im\sigma}^{\dagger} \hat{f}_{im'\bar{\sigma}} \\ & \quad \left. - \rho_{im'\sigma im\sigma} \hat{f}_{im\bar{\sigma}}^{\dagger} \hat{f}_{im'\bar{\sigma}} - \rho_{im\bar{\sigma} im'\bar{\sigma}} \hat{f}_{im\sigma}^{\dagger} \hat{f}_{im'\sigma} \right) \\ & + \sum_{im\sigma} \epsilon_{im\sigma} \hat{f}_{im\sigma}^{\dagger} \hat{f}_{im\sigma} - \sum_i \sum_m h_{im} \hat{n}_{im} \\ & \quad - \sum_{ii'mm'} \langle \hat{O}_{im}^{\dagger} \hat{O}_{i'm'} \rangle_s \sum_{\sigma} t_{imim'\sigma} \hat{f}_{im\sigma}^{\dagger} \hat{f}_{i'm'\sigma}. \quad (3.17) \end{aligned}$$

3.1.4 Spin+orbital slave

This approach represents maximum fine-graining whereby we use a slave boson for each spin+orbital combination. Thus the index α now represents a full set of quantum numbers $m\sigma$ so we have $\hat{O}_{im\sigma}$ and $\hat{N}_{im\sigma}$ for the slave operators. The physically allowed occupancies are 0 and 1 which

is isomorphic to a pseudo-spin. For this reason, the named used for this approach in the literature is the “slave-spin” method [15, 16]. However, given the possible confusion this term creates between the real electron spin as well as the difficulty of using such a name unambiguously in our generalized formalism, we prefer the more explicit name “spin+orbital slave” where the spin refers to the physical electron spin.

In this approach, we can describe the maximum number of interaction terms in the slave Hamiltonian:

$$\begin{aligned}
\hat{H}_s = & \frac{U}{2} \sum_i \left(\left(\sum_{m\sigma} \hat{N}_{im\sigma} \right)^2 - \sum_{m\sigma} \hat{N}_{im\sigma} \right) \\
& + \frac{U' - U}{2} \sum_{m \neq m'} \left(\sum_{\sigma} \hat{N}_{im\sigma} \right) \left(\sum_{\sigma'} \hat{N}_{im'\sigma'} \right) - \frac{J}{2} \sum_{\sigma} \sum_{m \neq m'} \hat{N}_{im\sigma} \hat{N}_{im'\sigma} \\
& + \sum_i \sum_{m\sigma} h_{im\sigma} \hat{N}_{im\sigma} - \sum_{ii'mm'\sigma} t_{imim'\sigma} \langle \hat{f}_{im\sigma}^\dagger \hat{f}_{i'm'\sigma} \rangle_f \hat{O}_{im\sigma}^\dagger \hat{O}_{i'm'\sigma}. \quad (3.18)
\end{aligned}$$

The corresponding spinon Hamiltonian still contains the spin flip and pair-hopping terms:

$$\begin{aligned}
\hat{H}_f = & -\frac{J}{2} \sum_{i\sigma} \sum_{m \neq m'} \\
& \left(\rho_{im\bar{\sigma}im\sigma} \hat{f}_{im'\bar{\sigma}}^\dagger \hat{f}_{im'\sigma} + \rho_{im'\sigma im'\bar{\sigma}} \hat{f}_{im\sigma}^\dagger \hat{f}_{im\bar{\sigma}} \right. \\
& - \rho_{im'\sigma im\sigma} \hat{f}_{im'\bar{\sigma}}^\dagger \hat{f}_{im\bar{\sigma}} - \rho_{im\bar{\sigma} im'\bar{\sigma}} \hat{f}_{im\sigma}^\dagger \hat{f}_{im'\sigma} \\
& + \rho_{im'\bar{\sigma} im\sigma} \hat{f}_{im\bar{\sigma}}^\dagger \hat{f}_{im'\sigma} + \rho_{im'\sigma im\bar{\sigma}} \hat{f}_{im\sigma}^\dagger \hat{f}_{im'\bar{\sigma}} \\
& \left. - \rho_{im'\sigma im\sigma} \hat{f}_{im\bar{\sigma}}^\dagger \hat{f}_{im'\bar{\sigma}} - \rho_{im'\bar{\sigma} im\bar{\sigma}} \hat{f}_{im\sigma}^\dagger \hat{f}_{im'\sigma} \right) \\
& + \sum_{i\sigma} \epsilon_{im\sigma} \hat{f}_{im\sigma}^\dagger \hat{f}_{im\sigma} - \sum_i \sum_m h_{im} \hat{n}_{im} \\
& - \sum_{ii'mm'} \langle \hat{O}_{im}^\dagger \hat{O}_{i'm'} \rangle_s \sum_{\sigma} t_{imim'\sigma} \hat{f}_{im\sigma}^\dagger \hat{f}_{i'm'\sigma}. \quad (3.19)
\end{aligned}$$

We mention that in prior work [15], the spin flip and pair hopping terms were argued to be well treated in the slave-particle sector instead. Namely, they were removed from the spinon Hamiltonian and the following terms were added to the slave Hamiltonian:

$$- J \sum_{m \neq m'} (\hat{S}_{im\uparrow}^+ \hat{S}_{im\downarrow}^- \hat{S}_{im'\downarrow}^+ \hat{S}_{im'\uparrow}^- + \hat{S}_{im\uparrow}^+ \hat{S}_{im\downarrow}^+ \hat{S}_{im'\uparrow}^- \hat{S}_{im'\downarrow}^- + h.c.) \quad (3.20)$$

where the \hat{S} operators in the number basis are

$$\hat{S}^+ = \begin{pmatrix} 0 & 0 \\ 1 & 0 \end{pmatrix}, \quad \hat{S}^- = \begin{pmatrix} 0 & 1 \\ 0 & 0 \end{pmatrix} \quad (3.21)$$

While such an *ad hoc* approach is not the strictly theoretically consistent way to split operators between the spinon and slave boson sectors, in practice it does reproduce the desired behavior of the spin flip and pair hopping terms in the slave boson sector and does not introduce any numerical difficulties.

3.2 Mean-Field Tests

We now proceed to describe computational results based on a simple single-site, paramagnetic, nearest-neighbor, mean-field solution of the slave Hamiltonian at half filling. This will permit us to both reproduce prior literature as well as to compare various slave Hamiltonians to each other.

To do so, we shift the local interaction energies so that they are zero at half filling, i.e. when $n_{im\sigma} = 1/2$. We also make the standard choice

$U' = U - 2J$. The local interaction term (ignoring for the moment the spin flip and pair-hopping terms) takes the form from prior work[16]:

$$\hat{H}_{int}^i = \frac{U - 2J}{2} (\hat{n}_i - n_{orb}^i)^2 + J \sum_m (\hat{n}_{im} - 1)^2 - \frac{J}{2} \sum_\sigma (\hat{n}_{i\sigma} - n_{orb}^i/2)^2 \quad (3.22)$$

where n_{orb}^i is the number of localized correlated spatial orbitals on site i .

In the single-site mean-field approximation, we will be solving for a single site self-consistently coupled to an averaged bath of bosons on the nearest neighbor sites. Our assumptions ensure that all sites are identical with no spin polarization. Furthermore, to connect to the literature, we further assume that in the multi-orbital case there are only non-zero hoppings between nearest neighbor orbitals with the same m index. With all these assumptions, it is easy to see that $C_{i\alpha} = 1$ is the choice that gives half-filling for the slave problem at $U = U' = J = 0$. In addition, we can set the Lagrange multipliers $h_{i\alpha} = 0$ since we have set the half-filling energy to be zero. The density matrix elements $\langle \hat{f}_{im\sigma}^\dagger \hat{f}_{i'm'\sigma} \rangle_f$ that renormalize the slave boson hoppings will be spin and site independent and will be non-zero only when $m = m'$. Hence, they can be absorbed into the definition of the hopping elements $t_{imi'm'\sigma}$.

We begin with $J = 0$. The slave Hamiltonian is

$$H_s = \frac{U}{2} \sum_i \left(\sum_\alpha \hat{N}_{i\alpha} - n_{orb} \right)^2 - \sum_{i\alpha} \sum_{m \in \alpha} \left(\hat{O}_{i\alpha} t_m^{eff} + \hat{O}_{i\alpha}^\dagger t_m^{eff} \right) \quad (3.23)$$

where the effective hopping for spatial orbital m is

$$t_m^{eff} = \sum_{i'\alpha'} \sum_{m'\sigma \in \alpha'} t_{imi'm'\sigma} \langle \hat{O}_{\alpha'} \rangle_s.$$

The simple form of this Hamiltonian makes it easy to directly read off the quasiparticle weight renormalization Z_α which narrows the spinon bands:

$$Z_\alpha = \langle \hat{O}_\alpha \rangle_s^2. \quad (3.24)$$

When $Z_\alpha = 0$, a Mott insulator is realized in such a simple single-site model [50]. We solve the problem self-consistently for different slave models. Since at half-filling the Lagrange multipliers $h_{i\alpha} = 0$, all that is required to solve the spinon problem is to renormalize each spinon band width (i.e., hopping) by the appropriate Z_α factor.

3.2.1 Single-band Mott transition

We begin with a single-band model where there is one spatial orbital per site. Figure 3.2 compares various slave models based on the dependence of Z on U . Specifically, we compare the slave rotor model (allowed occupancies from $-\infty$ to $+\infty$), the orbital slave model (allowed occupancies 0, 1, or 2) which here is identical to the number slave model, the spin+orbital slave (“slave-spin”) model (allowed occupancies 0 or 1) and the Gutzwiller approximation where $Z_{Gutzwiller} = 1 - (U/U_c)^2$.

For this system, the Gutzwiller and spin+orbital slave methods predict exactly the same results, as noted previously.[16] In fact, the spin+orbital slave model, at half-filling for a single orbital per site at the single-site mean field level, can be shown to be isomorphic to the Gutzwiller approximation as well as to the Kotliar-Ruckenstein model as described by Bunemann.[45] This shows that, beyond their utility as mathematical models, such slave-boson methods can parallel and help understand

other approaches that originate from apparently different sets of many-body approximations.

The slave-rotor method has an aberrant behavior for small U . Specifically, Z for the slave-rotor method has the small U expansion

$$Z_{rotor} = 1 - O(\sqrt{U/t_{eff}}). \quad (3.25)$$

The reason for this behavior is due to the unbounded number states permitted in the slave rotor model. Specifically, in the number basis the slave-rotor problem corresponds to an infinite one dimension lattice labeled by N_i , with hoppings t^{eff} between neighboring sites, and with a quadratic potential $UN_i^2/2$. For small U , the ground state of this problem will be spread over many sites so that we can take the continuum limit. The problem turns into the textbook one dimensional harmonic oscillator with mass $1/(2t_{eff})$ and spring constant U . The ground state wave function $\psi(N_i)$ is a Gaussian, and $\langle O \rangle_s = \sum_n \psi(n)\psi(n-1)$ can be computed. Expansion in U then gives the above form.

In reality, however, perturbation theory guarantees that quasiparticle weights are modified starting at second order in the interaction strength:

$$Z = 1 - O(U^2/t^{eff}). \quad (3.26)$$

The slave-rotor fails since for small U it spreads the wave function over a large number of unphysical states. What this means is that one would incorrectly overestimate the importance of electronic correlations at weak interaction strengths when using the slave-rotor method. In this view,

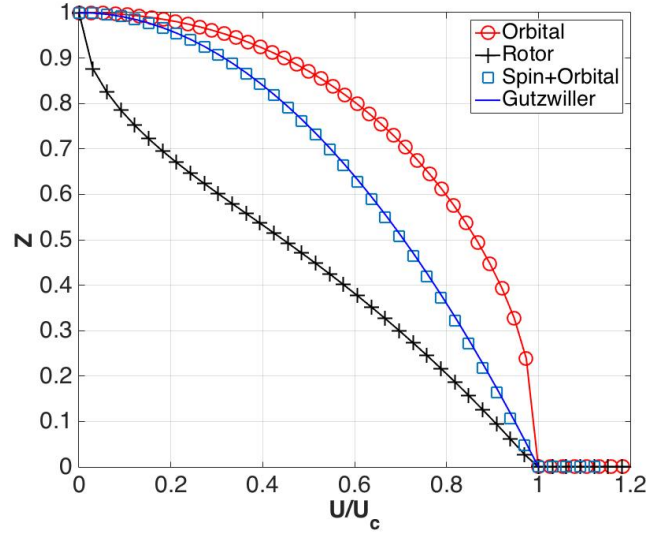


FIGURE 3.2: Quasiparticle weight Z as a function of U/U_c for different slave-particle models for the paramagnetic single-band Hubbard at half filling. U_c is the critical value of U when $Z = 0$, i.e., the Mott transition, for each model. The black crosses show slave rotor results, the blue circles are the Gutzwiller approximation results ($Z = 1 = \frac{U^2}{U_c^2}$) which for this model are the same as the spin+orbital slave (“slave-spin”) results in blue crosses, and the green circles show the orbital slave results (identical to the number slave). We note that the slave-orbital Hilbert space is very small, so that it does not agree with the rotor, unlike the two-band slave number.

our orbital and number slave methods may be viewed as corrected rotors which are restricted to the appropriate finite set of physical states. Finally, Figure 3.2 illustrates that slave methods employing finite slave Hilbert spaces all automatically correct the small U behavior.

3.2.2 Isotropic two-band Mott transition

Next, we consider a two-band degenerate Hubbard model. Figure 3.3 displays the results. We note that the two band e_g model is of physical relevance as the slave-rotor has shown itself to be of use in e_g nickelate

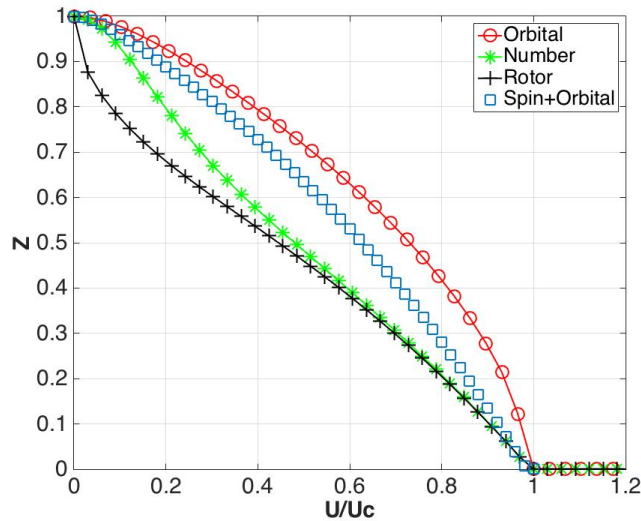


FIGURE 3.3: Quasiparticle weight Z as a function of U/U_c for different slave-particle models for a degenerate paramagnetic two-band Hubbard model at half filling.

systems within a pd model[46]. For this particular degenerate case with high symmetry, the spin slave and orbital slave models turn out to be identical since each posits two slave particles each with the allowed occupations 0, 1, or 2. We note that, in this case, the slave rotor and number slave become very similar for large U : once slave number fluctuations of N_i are small, the size of the slave Hilbert space becomes irrelevant.

3.2.3 Anisotropic Orbital-Selective Mott Transition

We present mean-field calculations exemplifying the orbital-selective Mott transition in an anisotropic two band model with paramagnetic solution and at half filling. We take spatial orbital $m = 1$ to have the larger hopping t_1 while $m = 2$ has the smaller hopping t_2 . Hence, t_2/t_1 specifies the degree of anisotropy.

The first slave model for this system is the spin+orbital method which

has been used previously[15, 16]: each slave boson has allowed occupancies 0 or 1. The second model is to forgo the explicit spin degree of freedom in the slave description and to employ the orbital slave model where each slave boson has allowed occupancies 0, 1, and 2. The comparison tests the importance of explicit treatment of spin in the electronic correlations for such a system. We will focus on the Orbital-Selective Mott Transition (OSMT) when one orbital has a finite bandwidth and is metallic while the other has undergone a Mott insulating transition and is localized.

We begin with $J = 0$. Figure 3.4 illustrates the behavior of the renormalization factor Z for both bands versus U for three different t_2/t_1 ratios within the two slave particle models. An OSMT occur for small enough t_2/t_1 ratio but the critical value depends on the type of slave model. For the orbital slave model, we find that OSMT occurs when $t_2/t_1 < 0.25$ while for spin+orbital slave we must have a slightly smaller value of $t_2/t_1 < 0.2$.

We now consider $J > 0$. We continue to treat the spinon problem as that of a simple, paramagnetic, half-filled tight-binding model with two separate bands with each hopping renormalized by the appropriate $\langle \hat{O}_\alpha \rangle_s$. For the orbital slave model, we can only include the first two terms of Eq. (3.22) due to the lack of an explicit spin label in the slave description. Thus we will compare the orbital slave and spin+orbital slave using the same interaction term

$$\hat{H}_{int}^i = \frac{U - 2J}{2} (\hat{N}_i - 2)^2 + J \sum_m (\hat{N}_{im} - 1)^2. \quad (3.27)$$

It is clear from the above two interaction terms that, for fixed U , $J > 0$ permits larger orbital independent number fluctuations (i.e., it reduces

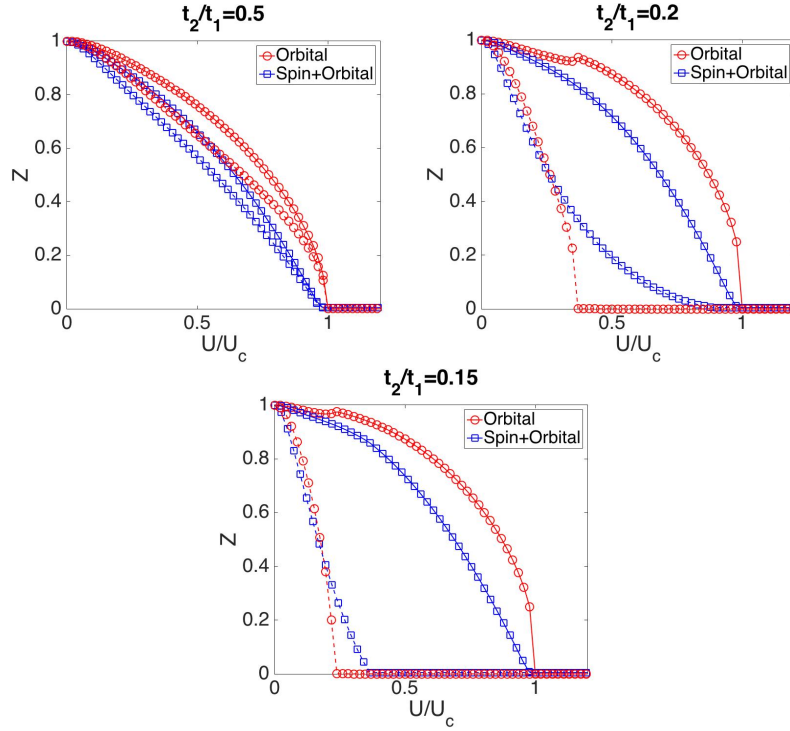


FIGURE 3.4: Quasiparticle weights for the paramagnetic anisotropic two-band single-site Hubbard model at half filling as predicted by the orbital+spin slave model (blue) and the orbital slave model (red) at $J = 0$ for three t_2/t_1 ratios. In each plot, the Z value for the first orbital with larger hopping t_1 is denoted by symbols while for the second orbital solid lines with no symbols are used. An OSMT occurs when the two Z do not go to zero at the same U value: orbital slave (red) in the center plot and both slave models in the lower plot.

the correlation effect of this mode) since $U' = U - 2J$ becomes smaller in the first term. However, the second $+J$ term simultaneously punishes intra-orbital number fluctuations and thus enhances intra-orbital correlation effects which in turn favors an OSMT.

The phase diagram as a function of t_2/t_1 and J for this system is shown in Figure 3.5. The boundaries shown separate regions where OSMT occurs (above the boundaries) from where a standard Mott transition occurs (below the boundaries). The figure confirms the fact that increasing J favors OSMT. Qualitatively, the orbital slave and spin+orbital slave show very similar behavior: they have a critical t_2/t_1 at $J = 0$ between 0.2–0.25 for OSMT to occur, and then with increasing J the critical t_2/t_1 becomes larger so less anisotropy is needed to drive an OSMT, as observed previously in DMFT [51] and spin+orbital slave calculations [16].

We have also considered the case where we permit the orbital slave model to have unlimited occupations: namely, we have a two rotor model (one for each orbital occupation). In this case, we find that no OSMT is possible when $J = 0$ for any bandwidth ratio t_2/t_1 . This result is similar to previous DMFT [16, 51], which found that a finite J is needed in order to have an OSMT. However, it contradicts the results of previous orbital+spin slave results [16] as well as our results above where we find that a small enough bandwidth ratio t_2/t_1 makes an OSMT possible even for $J = 0$. These differences further illustrate the need for multiple models and cross verification when describing a possible OSMT for real materials which have complex band structures (e.g., the three-band $\text{Ca}_{2-x}\text{Sr}_x\text{RuO}_4$ system [35]).

Prior work [16] has shown that the presence of the Hund's term

$$-\frac{J}{2} \sum_{\sigma} \sum_{m \neq m'} (\hat{n}_{m\sigma} - 1/2)(\hat{n}_{m'\sigma} - 1/2) = -\frac{J}{2} \sum_{\sigma} (\hat{n}_{i\sigma} - 1)^2 \quad (3.28)$$

makes OSMT slightly more difficult to achieve as it increases inter-orbital $m \neq m'$ correlations by favoring spin pairing between different orbitals but does not aid intra-orbital correlations. Separately, adding the spin-flip and pair-hopping terms makes OSMT easier to achieve [16].

Although not directly relevant to our main focus, for completeness we include a final comparison based on a fixed slave model with various combination of interaction terms. We choose the spin+orbital orbital model and then choose to include different interaction terms in the slave-particle Hamiltonian. The first choice is the interaction terms used above in Eq. (3.27). The second choice is to add the Hund's term:

$$\hat{H}_{int}^i = \frac{U - 2J}{2} (\hat{N}_i - 2)^2 + J \sum_m (\hat{N}_{im} - 1)^2 - \frac{J}{2} \sum_{\sigma} (\hat{N}_{i\sigma} - 1)^2. \quad (3.29)$$

Prior work [16] has shown that the presence of the Hund's term makes OSMT more difficult to achieve as it increases inter-orbital correlations by favoring spin-pairing among different orbitals but does not enhance intra-orbital correlations.

The third choice is to add the spin-flip and pair-hopping terms as per the *ad hoc* method of Eq. (3.20):

$$\begin{aligned} \hat{H}_{int}^i = & \frac{U - 2J}{2} (\hat{N}_i - 2)^2 + J \sum_m (\hat{N}_{im} - 1)^2 - \frac{J}{2} \sum_{\sigma} (\hat{N}_{i\sigma} - 1)^2 \\ & - J \sum_{m \neq m'} (\hat{S}_{im\uparrow}^+ \hat{S}_{im\downarrow}^- \hat{S}_{im'\downarrow}^+ \hat{S}_{im'\uparrow}^- + \hat{S}_{im\uparrow}^+ \hat{S}_{im\downarrow}^+ \hat{S}_{im'\uparrow}^- \hat{S}_{im'\downarrow}^- + h.c.). \end{aligned} \quad (3.30)$$

Adding these spin-flip and pair-hopping terms makes OSMT easier to achieve [16].

Phase diagrams for the second and third choices above are available in the literature [16] and are reproduced in Figure 3.6 which also includes the results of the first choice as well. We note that only including the intra-orbital terms (first choice) or all terms (third choice) leads to essentially the same phase diagram. However, excluding the spin-flip and pair-hopping terms (second choice) makes it harder to achieve an OSMT phase: one can not achieve an OSMT for any reasonable J once the bandwidth ratio t_2/t_1 exceeds ≈ 0.6 . The physics behind this progression is as follows. Starting with $J = 0$ and a relatively large U , the ground-state basically contains only states which are half-filled and have a total of two electrons per site (there are six such states). Adding the intra-orbital term (first choice) with $J > 0$ then further restricts us to the four states with only one electron per orbital (but with no preference for spin states). Such a ground-state can suffer an OSMT when further increasing U since the narrower band (more localized orbital) can become fully localized. Next, adding the Hund's term (second choice) creates a preference for the two spin-aligned states in this four dimensional subspace by lowering their energy: this enhances inter-orbital correlations at the expense of intra-orbital correlations which favor an OSMT phase. Third, adding the spin-flip and pair-hopping (third choice) terms essentially cancels the effect of the Hund's term. This is explained by a straightforward computation of the matrix elements of this interaction in the four dimensional subspace. One finds that the spin-flip term couples the two states where electrons have opposite spins with a strength that is precisely such that their symmetric combination has the same energy lowering as the Hund's term induces for the spin-aligned states. Thus,

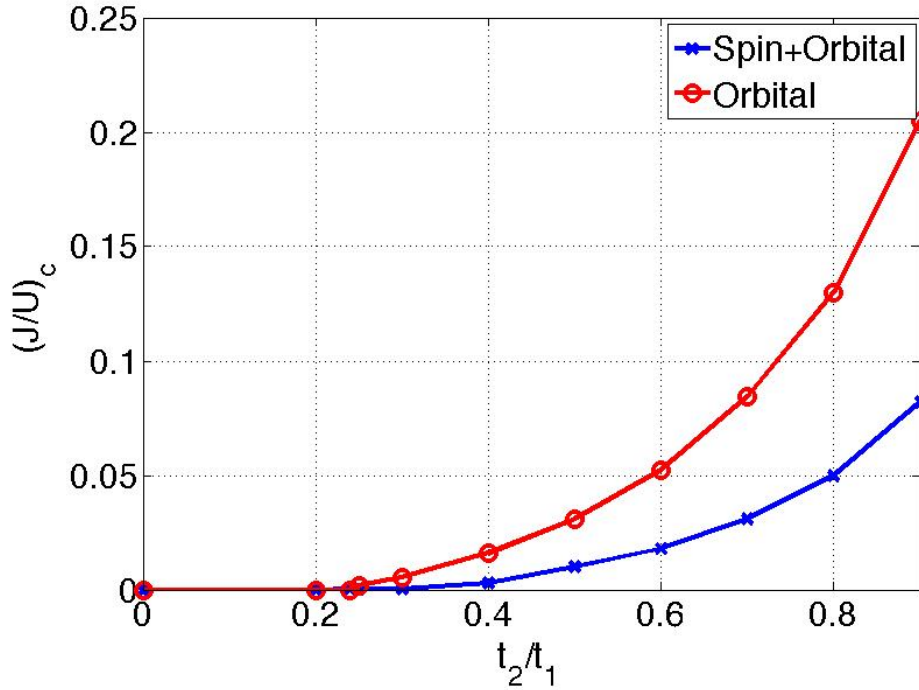


FIGURE 3.5: Phase diagram for the anisotropic two-band single-site Hubbard model at half-filling as a function of the anisotropy ratio t_2/t_1 and J . Two slave boson methods are used: orbital slave (red circles) and spin+orbital slave (blue crosses). In each case, the boundary curve demarcates the possible existence of an Orbital-Selective Mott Transition when U is ramped up from $U = 0$. Regions above the boundary display OSMT while regions below it present a standard Mott transition where both bands become insulating at the same critical U_c value.

we are essentially back to the four states we had when only operating with the intra-orbital interaction (first choice). Our final comment is that these differences are not very dramatic once the hopping ratio t_2/t_1 is below ≈ 0.5 . As Fig. 3.6 shows, in all cases only a modest value for J is sufficient to stabilize the OSMT phase instead of a standard Mott transition.

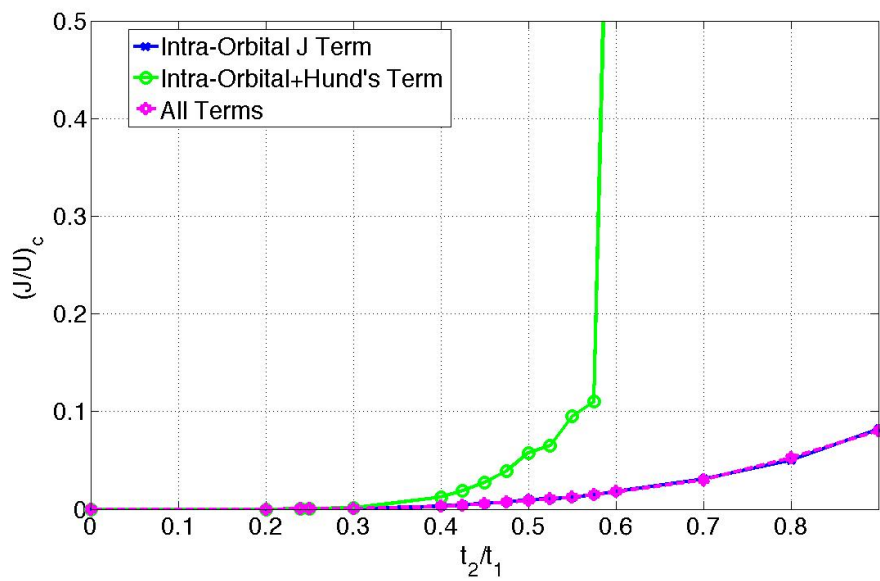


FIGURE 3.6: Phase diagram for the anisotropic two-band single-site Hubbard model at half-filling as a function of the anisotropy ratio t_2/t_1 and J for the spin+orbital slave model. Three different interaction terms are used: intra-orbital term only which is Eq. (3.27), intra-orbital plus Hund's which is Eq. (3.29), and all terms included which is Eq. (3.30)

. This allows us to isolate the role of each interaction term.

3.2.4 Ground State Energies

A final and most stringent test for the slave models is to compare their total energies. In the interest of space, we will focus on the simplest case of degenerate orbitals, isotropic hopping, and phases that are paramagnetic and paraorbital (no orbital differentiation) to make some general comments. In a fully self-consistent model with more parameters and non-degenerate bands, we may expect more complexity to be revealed. Previous work [52] has shown that ground-state calculations can reveal competition between the orbital-selective Mott state (due to very large crystal-field splitting) and an anti-ferromagnetic Mott insulating state (due to a large J), a transition which is likely first-order [52].

With $J = 0$, the ground state energy per site of the paramagnetic and paraorbital phase is

$$E_g = - \sum_{\alpha} \sum_{m \in \alpha} t_m^{eff} \langle \hat{O}_{\alpha} \rangle_s + \frac{U}{2} \langle [\sum_{\alpha} \hat{N}_{\alpha} - n_{orb}]^2 \rangle. \quad (3.31)$$

We compute the ground-state energy as a function of U for one-band and two-band isotropic models at half-filling (same systems that are in the above sections) and also include the Hartree-Fock total energy. Figures 3.7 and 3.8 display the energies versus U for the one-band and two-band cases, respectively. The plots employ the half-band width $D = 2t$.

In all cases, for large enough U the slave models produce an insulating phase (i.e., isolated atomic-like sites) which has zero hopping and zero number fluctuation and thus zero energy in this model. The Hartree-Fock total energy necessarily has a linear dependence on U for the high

degree of spin and orbital symmetry since the Hartree-Fock Slater determinant wave function will be unchanged versus U and always predicts a metallic system.

The next observation is that for small U , some of the slave models do worse than Hartree-Fock. However, as U is increased their total energies eventually drop below the Hartree-Fock one. Furthermore, increasing the number of bands from one to two improves the total energies of all slave methods compared to Hartree-Fock. For a given number of bands, increasing the fine-grained of the slave model (i.e., having more slave modes per site) also lowers the total energy. Hence, the slave-rotor is generally the worst performer.

A final observation is that only the fully fine-grained spin+orbital slave method, which can differentiate between all possible configurations, always predicts a total energy below that of Hartree-Fock. It also has the correct linear slope of E_g versus U matching the Hartree-Fock one. The other slave methods have higher slopes of E_g versus U at the origin so that they can only outperform Hartree-Fock beyond some finite value of U . The slope matching of the spin+orbital slave is a natural expression of its accounting in detail for all the quantum numbers on each site and in being forced (like all slave models) to reproduce the non-interacting state at $U = 0$. The fact that the other slave models have higher slopes is a reflection of their larger (and quantitatively incorrect) number fluctuations at $U = 0$. Namely, the interaction Hamiltonian \hat{H}^{int} is a quadratic function of the occupancy numbers so that its expectation value (the interaction energy) depends directly on the fluctuations

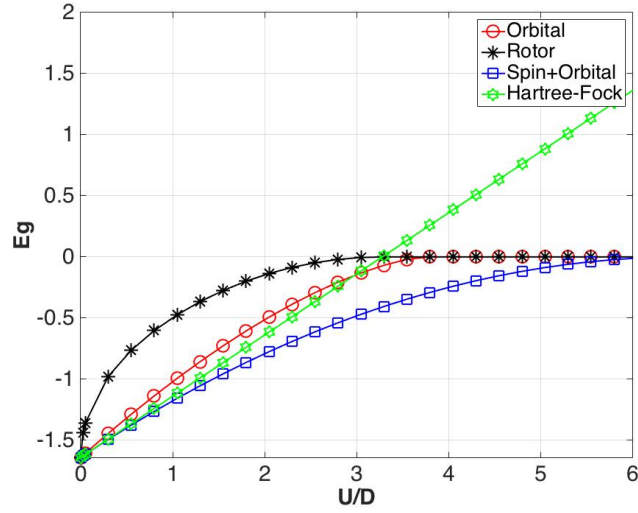


FIGURE 3.7: Ground-state energy per site (E_g/t) of a single band Hubbard model at $J = 0$ in the paramagnetic phase at half filling for a variety of slave representations as well as for the Hartree-Fock approximation. $D = 2t$ is the band width of the non-interacting system. For this model the orbital slave is identical to the number slave and the spin slave is the same as the spin+orbital slave.

of these occupancies; at fixed U , the larger the set of allowed occupancies in a slave model, the larger this quadratic fluctuation and the higher the interaction energy. In fact, the number fluctuations of the slave-rotor model are so large at $U = 0$ that they lead to a pathological infinite slope of E_g versus U at $U = 0$. By comparison, the number slave method, which can be viewed as a corrected rotor, has a much more reasonable behavior.

As a side note, it is interesting that for the single-band case, one has the following analytical results based on the coincidence of the of the spin+orbital slave and Gutzwiller approximations. In the metallic phase, where $U < U_c$, the quasiparticle weight Z is given by

$$Z = 1 - U^2/U_c^2 \quad (3.32)$$

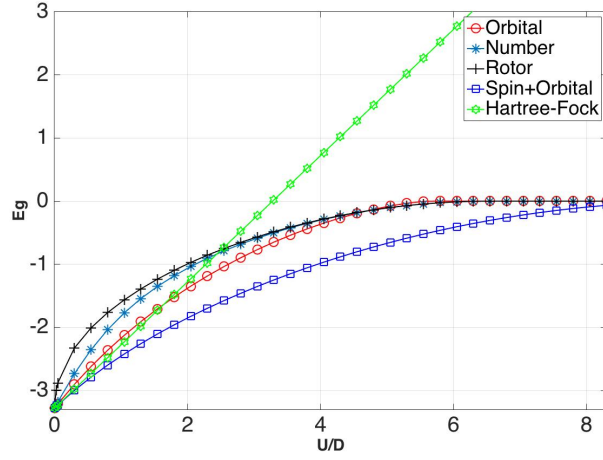


FIGURE 3.8: Ground-state energy per site (E_g) for an isotropic two-band Hubbard model at half filling for $J = 0$ in the paramagnetic and paraorbital phase.

and from perturbation theory at small Z [8]

$$U_c = 8D. \quad (3.33)$$

Using the following definition:

$$t_0 = t \langle f_{im\sigma}^\dagger f_{im\sigma} \rangle_{U=0} \quad (3.34)$$

the ground-state energy is given by

$$E_g = -2t_0 + \frac{U}{4} - \frac{U^2}{128t_0^2}. \quad (3.35)$$

For the insulating state ($U \geq U_c$), we have $E_g = 0$.

Our calculations in this section permit us to say that while our generalized approach permit us to easily compare different slave models and isolate different degrees of freedom simply, total energy comparisons are

much more challenging. First, one should do energy comparisons of different phases within a single slave model since the differing models can produce differing total energies with dependence on the details of the system. Second, after understanding the relevant degrees of freedom and how they influence the physical behavior, the total energy calculation should be most accurate with the most fine-grained model which is in the spin+orbital slave representation (“slave-spin” in the literature).

3.3 Conclusion

We have developed a generalized formalism that reproduces previous slave-particle formalisms in appropriate limits but also allows us to define and explore intermediate models and to compare them systematically. Our formalism moves beyond the analogy with angular momentum behind slave-rotor formalism, and instead works directly in the physically correct finite-sized number representation permitting new models to be developed in what we feel is a more natural way based on occupation numbers. As an example, we have shown how the standard Mott transition as well as the orbital selective Mott transition appear in different slave models for single-band and two-band Hubbard models.

We believe it is useful to have a variety of slave particle methods on hand as they provide computationally inexpensive methods for exploring the role of electronic correlations in materials and interfaces with broken symmetries (e.g., orbital symmetry breaking). The cheap computational load is particularly advantageous for interfacial systems where translational symmetry is lost in one direction and simulation cells that

capture the region near the interface must contain at least tens to hundreds of atoms. As such, these simpler slave-particle models are useful for exploratory research where more accurate and expensive Hubbard-model solvers such as DMFT [12, 36] would be prohibitive to apply routinely. The ability to isolate potentially interesting correlated degrees of freedom from each other by choosing different slave approaches may illuminate which degrees of freedom are the most critical to model accurately.

3.4 Appendix

In this appendix, we provide some detailed examples of how the physical subspace is isolated from the extended Hilbert space of spinon+slave boson states and how the operators act in the physical subspace. In the process, we also provide explicit examples for various choices of the slave labels α . We focus on a single site i and hence suppress the site label i below.

The original Hilbert space, i.e, the Fock space of the fermionic $\hat{d}_{m\sigma}$ field operators, is spanned by basis kets in the occupancy number representation for the field operators and have the form $|\{n_{m\sigma}\}\rangle$ where $n_{m\sigma} \in \{0, 1\}$. The enlarged Hilbert space for spinons and slave particles is spanned by product kets in the number occupancy basis of the form

$$|\{n_{m\sigma}\}\rangle_f |\{N_\alpha\}\rangle_s$$

where, again, $n_{m\sigma} \in \{0, 1\}$ are the fermionic spinon occupancies while N_α are the bosonic particle counts. The f and s subscripts label the

spinon and slave boson kets.

The constraint on the physical allowed states translates to the numerical constraint

$$N_\alpha = \sum_{m\sigma \in \alpha} n_{m\sigma}. \quad (3.36)$$

We remember that we choose the $\{n_{m\sigma}\}$ to match exactly between the original electron and spinon kets.

We begin with the simplest example of a single spatial orbital on the site where the kets look like $|n_\uparrow, n_\downarrow\rangle_f |\{N_\alpha\}\rangle_s$. There are two states for electrons and thus a total of four possible configurations: no electrons, one spin up electron, one spin down electron, and a pair of spin up and down electrons. If we have a single slave boson per site to simply count the number of electrons so the α label is nil (i.e., the number slave representation), then our four physically allowed kets are

$$|0, 0\rangle_f |0\rangle_s, |1, 0\rangle_f |1\rangle_s, |0, 1\rangle_f |1\rangle_s, |1, 1\rangle_f |2\rangle_s.$$

We note that the number of slave particles is constrained by Eq. (??) to the total the number of spinons.

Next, if we have this single orbital but instead we choose to have a slave mode per spin channel (i.e, the spin+orbital slave representation), then we have two sets of slave bosons since now $\alpha = \sigma$. The four physical states are now

$$|0, 0\rangle_f |0, 0\rangle_s, |1, 0\rangle_f |1, 0\rangle_s, |0, 1\rangle_f |0, 1\rangle_s, |1, 1\rangle_f |1, 1\rangle_s.$$

A more complex set of examples has two spatial orbitals per site. Here

we have four choices of spinon label $m\sigma$ which we order as $1\uparrow, 1\downarrow, 2\uparrow, 2\downarrow$.

For the number slave representation, we have the 16 physical kets

$$\begin{aligned}
&|0, 0, 0, 0\rangle_f|0\rangle_s, |1, 0, 0, 0\rangle_f|1\rangle_s, |0, 1, 0, 0\rangle_f|1\rangle_s, \\
&|0, 0, 1, 0\rangle_f|1\rangle_s, |0, 0, 0, 1\rangle_f|1\rangle_s, |1, 1, 0, 0\rangle_f|2\rangle_s, \\
&|1, 0, 1, 0\rangle_f|2\rangle_s, |1, 0, 0, 1\rangle_f|2\rangle_s, |0, 1, 1, 0\rangle_f|2\rangle_s, \\
&|0, 1, 0, 1\rangle_f|2\rangle_s, |0, 0, 1, 1\rangle_f|2\rangle_s, |1, 1, 1, 0\rangle_f|3\rangle_s, \\
&|1, 1, 0, 1\rangle_f|3\rangle_s, |1, 0, 1, 1\rangle_f|3\rangle_s, |0, 1, 1, 1\rangle_f|3\rangle_s, \\
&|1, 1, 1, 1\rangle_f|4\rangle_s.
\end{aligned}$$

An orbital slave representation has slave bosons counting the number of electrons in each spatial orbital, so $\alpha = m$. The 16 allowed kets are

$$\begin{aligned}
&|0, 0, 0, 0\rangle_f|0, 0\rangle_s, |1, 0, 0, 0\rangle_f|1, 0\rangle_s, |0, 1, 0, 0\rangle_f|1, 0\rangle_s, \\
&|0, 0, 1, 0\rangle_f|0, 1\rangle_s, |0, 0, 0, 1\rangle_f|0, 1\rangle_s, |1, 1, 0, 0\rangle_f|2, 0\rangle_s, \\
&|1, 0, 1, 0\rangle_f|1, 1\rangle_s, |1, 0, 0, 1\rangle_f|1, 1\rangle_s, |0, 1, 1, 0\rangle_f|1, 1\rangle_s, \\
&|0, 1, 0, 1\rangle_f|1, 1\rangle_s, |0, 0, 1, 1\rangle_f|0, 2\rangle_s, |1, 1, 1, 0\rangle_f|2, 1\rangle_s, \\
&|1, 1, 0, 1\rangle_f|2, 1\rangle_s, |1, 0, 1, 1\rangle_f|1, 2\rangle_s, |0, 1, 1, 1\rangle_f|1, 2\rangle_s, \\
&|1, 1, 1, 1\rangle_f|2, 2\rangle_s.
\end{aligned}$$

Alternatively, one can use the spin slave representation where the bosons count the number of electrons of each spin, so $\alpha = \sigma$. The allowed kets

are

$$\begin{aligned}
& |0, 0, 0, 0\rangle_f |0, 0\rangle_s, |1, 0, 0, 0\rangle_f |1, 0\rangle_s, |0, 1, 0, 0\rangle_f |0, 1\rangle_s, \\
& |0, 0, 1, 0\rangle_f |1, 0\rangle_s, |0, 0, 0, 1\rangle_f |0, 1\rangle_s, |1, 1, 0, 0\rangle_f |1, 1\rangle_s, \\
& |1, 0, 1, 0\rangle_f |2, 0\rangle_s, |1, 0, 0, 1\rangle_f |1, 1\rangle_s, |0, 1, 1, 0\rangle_f |1, 1\rangle_s, \\
& |0, 1, 0, 1\rangle_f |0, 2\rangle_s, |0, 0, 1, 1\rangle_f |1, 1\rangle_s, |1, 1, 1, 0\rangle_f |2, 1\rangle_s, \\
& |1, 1, 0, 1\rangle_f |1, 2\rangle_s, |1, 0, 1, 1\rangle_f |2, 1\rangle_s, |0, 1, 1, 1\rangle_f |1, 2\rangle_s, \\
& |1, 1, 1, 1\rangle_f |2, 2\rangle_s.
\end{aligned}$$

The final point is to check that the original electron operators $\hat{d}_{m\sigma}$ have the same effect as the combination of spinon and slave $\hat{f}_{m\sigma}\hat{O}_\alpha$ in the physical subspace. That this is in fact true follows directly from the defining Equations along with the constraint on N_α in Eq. (3.36). It is easy to check that the matrix elements of $\hat{d}_{m\sigma}$ and $\hat{f}_{m\sigma}\hat{O}_\alpha$ must match:

$$\langle n'_{m\sigma} | \hat{d}_{m\sigma} | n_{m\sigma} \rangle = {}_f \langle n'_{m\sigma} | \hat{f}_{m\sigma} | n_{m\sigma} \rangle_f \cdot {}_s \langle N'_\alpha | \hat{O}_\alpha | N_\alpha \rangle_s.$$

The matching of the \hat{d} and \hat{f} matrix elements is clear because the occupancies $n_{m\sigma}$ and $n'_{m\sigma}$ match by definition on both sides and both operators have identical behavior on the occupancies as per Eqs. (??) and (??). Thus both sides are non-zero only if the n' occupancy set has one fewer total count than the n occupancy set. As long as $N_\alpha > 0$, the matrix element of \hat{O}_α is unity because $N'_\alpha = N_\alpha - 1$ must be true due to the occupancy matching of Eq. (3.36). If $N_\alpha = 0$, it must be that $n_{m\sigma} = 0$, so that the matrix element of \hat{O}_α is irrelevant because the fermionic matrix elements (of \hat{d} and \hat{f}) are both zero.

Chapter 4

Symmetry Breaking in Occupation Number Based Slave-Particle Methods

The effects of strong electronic interactions and electronic correlations on materials properties is a subject with a considerable history. The most celebrated textbook example is the Mott transition where by increasing the strength of localized electronic repulsions, the electrons in the material lose band mobility and instead localize on the atomic sites (i.e., loss of wave behavior). However, electronic correlations also underlie many other ordered electronic phases such as various forms of magnetism as well as superconductivity. A canonical model Hamiltonian for correlated electron is the (extended) Hubbard model where electrons can hop between localized orbitals centered on atomic sites but multiple electronic occupancy of a given atomic site leads to a significant energy penalty U . By varying the ratio of U to the band hopping parameters, one can cover the range from weak to strong electronic interactions and correlations.[6]

The workhorse in realistic first principles calculations in crystal and

electronic structure calculations, Density Functional Theory (DFT)[3], is fundamentally based on a description of non-interacting electrons, i.e., band theory. Due to its simple structure, band theory approaches can not capture the effects of dynamical electronic fluctuations and localized correlations on electronic band spectra. Extensions of DFT to go beyond local exchange-correlation potentials and to include non-local Hartree-Fock type electronic behavior, such as the DFT+U or hybrid functional approaches[21, 53], can capture certain effects of electron-electron interactions especially for strongly symmetry-broken situations. Nevertheless, these are still band theory descriptions incapable of leading, e.g., to electron localization without resorting to symmetry breaking.

More advanced computational many-body approaches for simulation of electronic correlations are based on Green's functions methods. One type of approach is the *GW* approximation to the electron self-energy [54–56] which is a fully *ab initio* approach that includes the physics of non-local and dynamical electronic screening and produces accurate results for electronic band energies of a wide variety of materials [56, 57]. However, the *GW* method is based on summation of a subset of many-body diagrams (RPA diagrams) and thus does not capture a number of physical effects; separately *GW* calculations are notoriously expensive in terms of computation time due to their fully *ab initio* nature and lack of a particular basis set. Another avenue of approach is represented by Dynamical Mean Field Theory (DMFT) [12, 36] which can include the effect of local interactions and dynamical fluctuations by solving a model

Hamiltonian with local interactions exactly (i.e., all diagrams for the local interactions are included). However, DFT+DMFT calculations on realistic materials with large unit cells are still quite challenging as they require large-scale parallel computations.

For all these reasons, approximate and efficient methods for solving correlated problems continue to be of interest to the computational many-body community. One set of methods of recent interest for solving Hubbard models are slave-particle (slave-boson) methods. This method that has a long background in condensed matter theory. These methods have been used to study cases with infinitely strong repulsive interactions. [5, 7, 37–41] Dealing with finite interaction strengths was enabled by Kotliar-Ruckenstein approach [7] whose variants and modifications have been applied to study high-temperature superconductors [42] as well as multi-band models [43–45] to elucidate the effects of multiple orbitals, degeneracy and Hund’s coupling. [43, 44] In these approaches, each bosonic slave degree of freedom tracks the occupancy of a particular electronic configuration of a correlated site: once multiple orbitals and multiple electron counts can exist on a site, the number of required bosons becomes large. These methods can and have been used to describe spontaneously broken electronic symmetry (e.g., magnetic) states. [7, 43]

A recent set of more economical slave-particle methods has been developed and have become of wider interest, such as the slave-rotor method [8, 9] and its application to nickelate oxides [46] and the slave-spin method [15, 16] and its application to iron-based superconductors [47]. Recently, we have developed a generalized version of these methods that does not require the analogy with spin or angular momentum and introduces

multiple intermediate slave-particle models.[17] These recent approaches use slave degrees of freedom to track the electron occupation number on a site, and its distribution among orbital and spin channels, and thus require a much smaller number of bosons per site.

However, in all the previous literature in which these occupation number based methods has been used, spontaneous symmetry breaking has been achieved in multi-orbital systems where both a Hubbard U as well as a non-zero Hund's J interaction have been operative.[10, 15, 47] For a system where only the repulsion U operates, spontaneous symmetry breaking has not been displayed even when interaction-induced magnetism is a feature of the actual ground state of the model Hamiltonian (e.g., ground-state antiferromagnetic order for a half-filled single-band Hubbard model). Indeed, as we show, stabilizing a purely interaction induced symmetry-broken phase is very difficult for slave-particle methods without introduction of symmetry breaking fields. Our work describes this issue in detail and provides a total-energy approach that naturally produces symmetry breaking. We then show how one can make slave-particle self-consistency between spinon and slave modes much more efficient via a specific and exact decoupling of the two modes.

4.1 The Slave-Particle Approach

In this section we review the key aspects of the slave-particle formalism used in previous work to set up the notation and language used in subsequent sections. The general correlated-electron Hamiltonian we consider

is an extended Hubbard model given by

$$\hat{H} = \sum_i \hat{H}_{int}^i + \sum_{im\sigma} \epsilon_{im\sigma} \hat{d}_{im\sigma}^\dagger \hat{d}_{im\sigma} - \sum_{ii'mm'\sigma} t_{im'i'm'\sigma} \hat{d}_{im\sigma}^\dagger \hat{d}_{i'm'\sigma}. \quad (4.1)$$

The \hat{d} are canonical fermion annihilation operators. The indices i, i' range over the localized sites in the system (usually atomic sites), m, m' range over the localized spatial orbitals on each site, $\sigma = \pm 1$ denotes spin, \hat{H}_{int}^i is the local Coulombic interaction for site i , $\epsilon_{im\sigma}$ is the onsite energy of the state labeled by $im\sigma$, and $t_{im'i'm'\sigma}$ is the spin-conserving hopping element term connecting orbital $im\sigma$ to $i'm'\sigma$. A commonly used interaction term is given by the Slater-Kanamori form [48]

$$\begin{aligned} \hat{H}_{int}^i = & \frac{U_i}{2} (\hat{n}_i^2 - \hat{n}_i) + \frac{U_i - U'_i}{2} \sum_{m \neq m'} \hat{n}_{im} \hat{n}_{im'} \\ & - \frac{J_i}{2} \sum_{\sigma} \sum_{m \neq m'} \hat{n}_{im\sigma} \hat{n}_{im'\sigma} \\ & - \frac{J_i}{2} \sum_{\sigma} \sum_{m \neq m'} \left(\hat{d}_{im\sigma}^\dagger \hat{d}_{im\bar{\sigma}} \hat{d}_{im'\bar{\sigma}}^\dagger \hat{d}_{im'\sigma} \right. \\ & \left. + \hat{d}_{im\sigma}^\dagger \hat{d}_{im\bar{\sigma}}^\dagger \hat{d}_{im'\sigma} \hat{d}_{im'\bar{\sigma}} \right) \quad (4.2) \end{aligned}$$

While the Coulombic parameters U_i , U'_i and J_i can in principle depends the site index i , in practice in most models they are assumed to be the same for all correlated sites. Briefly, the U term describes repulsion between the same spatial orbitals on a site, U' repulsion between different orbitals, and J measures the strength of the Hund's interaction between

different orbitals with the same spin state. The number operators are

$$\hat{n}_{im\sigma} = \hat{d}_{im\sigma}^\dagger \hat{d}_{im\sigma}, \quad \hat{n}_{im} = \sum_{\sigma} \hat{n}_{im\sigma}, \quad \hat{n}_i = \sum_{m\sigma} \hat{n}_{im\sigma}.$$

The interacting Hubbard problem is impossible to solve exactly and even difficult to solve approximately. Some of the complexity is due to the fact that the interacting fermions have both charge and spin degrees of freedom. In slave-boson approaches[5, 7, 37–41], one separates the spin from charge degrees of freedom at each site by introducing a spinless charged bosonic “slave” degree of freedom on each site along with a spinful neutral fermion termed a spinon. The spinon and slave boson annihilation operators are indicated by \hat{f} and \hat{O} operators, respectively. Specifically, the electron field operators is decomposed as

$$\hat{d}_{im\sigma} = \hat{f}_{im\sigma} \hat{O}_{i\alpha}, \quad \hat{d}_{im\sigma}^\dagger = \hat{f}_{im\sigma}^\dagger \hat{O}_{i\alpha}^\dagger. \quad (4.3)$$

The index α is part of our generalized notation [17] that permits us to unify different occupation number based slave-particle models. The meaning of α depends on the type of slave boson model chosen, and α refers to a subset of the $m\sigma$ indices that belong to a site i . For example, if we use a slave-rotor model for the correlated orbitals on a site [8, 9], then α is nil: $\hat{O}_{i\alpha} = \hat{O}_i$. Namely, we have a single slave particle on each site i that only tracks the total number of electrons on that site. At the opposite limit, we can have a unique slave boson for each $m\sigma$ combination on a site (the “slave-spin” method[15, 16]), so that in this case $\alpha = m\sigma$.

The introduction of slave bosons by itself does not make solution of the Hubbard model any easier as more degrees of freedom have been

introduced to further enlarge the Hilbert space. To avoid sampling of unphysical states in the enlarged spinon+slave Hilbert space which have no correspondence to in the original electronic Hilbert space, one must ensure that the number of slave particles and number of spinons track each other. More precisely, Eq. (4.3) shows, spinon and slave particles are created or annihilated at the same time so that only state kets in the extended Hilbert space that obey this condition are physical. Hence, one must ensure that

$$\hat{d}_{im\sigma}^\dagger \hat{d}_{im\sigma} = \hat{f}_{im\sigma}^\dagger \hat{f}_{im\sigma}$$

and also that the subset of physical states $|\Psi_{phys}\rangle$ must obey

$$\hat{n}_{i\alpha} |\Psi_{phys}\rangle = \hat{N}_{i\alpha} |\Psi_{phys}\rangle \quad (4.4)$$

where $\hat{N}_{i\alpha}$ is the number counting operator for the slave particles and the correspond particle count for spinons is

$$\hat{n}_{i\alpha} = \sum_{m\sigma \in \alpha} \hat{f}_{im\sigma}^\dagger \hat{f}_{im\sigma}. \quad (4.5)$$

This constraint on the physical states simply ensures that the number of slave bosons matches exactly the number of spinons on each site.

The key approximation that makes the slave-boson approach more tractable than the original problem is to assume a separable form for the overall wave function of the system which takes a product form $|\Psi_f\rangle |\Phi_s\rangle$ where $|\Psi_f\rangle$ is a spinor-only state ket and $|\Phi_s\rangle$ is a slave-only state ket. This means one can only enforce the above operator constraints on average:

$$\langle \hat{n}_{i\alpha} \rangle_f = \langle \hat{N}_{i\alpha} \rangle_s \quad (4.6)$$

where the spinon and slave averages for any operator \hat{A} are defined via

$$\langle \hat{A} \rangle_f = \langle \Psi_f | \hat{A} | \Psi_f \rangle, \quad \langle \hat{A} \rangle_s = \langle \Phi_s | \hat{A} | \Phi_s \rangle.$$

This separability assumption means one must solve two separate and easier eigenvalue problems

$$\hat{H}_f | \Psi_f \rangle = E_f | \Psi_f \rangle, \quad \hat{H}_s | \Phi_s \rangle = E_s | \Phi_s \rangle$$

in a self-consistent fashion. The spinon Hamiltonian is given by

$$\begin{aligned} \hat{H}_f = & \sum_{im\sigma} \epsilon_{im\sigma} \hat{f}_{im\sigma}^\dagger \hat{f}_{im\sigma} - \sum_{i\alpha} h_{i\alpha} \hat{n}_{i\alpha} \\ & - \sum_{ii'\alpha\alpha'} \langle \hat{O}_{i\alpha}^\dagger \hat{O}_{i'\alpha'} \rangle_s \sum_{\substack{m\sigma \in \alpha \\ m'\sigma' \in \alpha'}} t_{imim'\sigma} \hat{f}_{im\sigma}^\dagger \hat{f}_{i'm'\sigma}. \end{aligned} \quad (4.7)$$

The slave boson Hamiltonian takes the form

$$\begin{aligned} \hat{H}_s = & \sum_i \hat{H}_{int}^i + \sum_\alpha h_{i\alpha} \hat{N}_{i\alpha} \\ & - \sum_{ii'\alpha\alpha'} \left[\sum_{\substack{m\sigma \in \alpha \\ m'\sigma' \in \alpha'}} t_{imim'\sigma} \langle \hat{f}_{im\sigma}^\dagger \hat{f}_{i'm'\sigma} \rangle_f \right] \hat{O}_{i\alpha}^\dagger \hat{O}_{i'\alpha'} \end{aligned} \quad (4.8)$$

where the spinon averages $\langle \hat{f}_{im\sigma}^\dagger \hat{f}_{i'm'\sigma} \rangle_f$ renormalize the slave boson hoppings. The slave boson problem is one of interacting charged bosons without spin on a lattice.

Self-consistency refers to the fact that the spinon Hamiltonian involves averaged quantities involving the slave wave function and vice versa. In addition, the values of the Lagrange multipliers $h_{i\alpha}$ must be chosen to

ensure average particle number matching as per Eq. (4.6).

4.2 Single-site mean-field approximation

In practice, the slave Hamiltonian of Eq. (4.8) represents a many-body interaction bosonic problem that has no exact solution. In what follows, when solving numerically for the ground state of a spinon+slave problem, we will use a simple single-site mean-field approach: when dealing with site i in the slave problem, we replace the $\hat{O}_{i\alpha}$ slave operators on the other neighboring sites by their averages $\langle \hat{O}_{i\alpha} \rangle_s$. For the spinon Hamiltonian, this boils down to the simple replacement

$$\langle \hat{O}_{i\alpha}^\dagger \hat{O}_{i'\alpha'} \rangle_s \rightarrow \langle \hat{O}_{i\alpha}^\dagger \rangle_s \langle \hat{O}_{i'\alpha'} \rangle_s$$

in the hopping term. The slave Hamiltonian turns into

$$\begin{aligned} \hat{H}_s = & \sum_i \hat{H}_{int}^i + \sum_\alpha h_{i\alpha} \hat{N}_{i\alpha} \\ & - \sum_{ii'\alpha\alpha'} \left[\sum_{\substack{m\sigma \in \alpha \\ m'\sigma' \in \alpha'}} t_{imi'm'\sigma} \langle \hat{f}_{im\sigma}^\dagger \hat{f}_{i'm'\sigma} \rangle_f \right] \\ & \left[\langle \hat{O}_{i\alpha}^\dagger \rangle_s \hat{O}_{i'\alpha'} + h.c. \right] \quad (4.9) \end{aligned}$$

which is a simple many-body system of isolated sites where the bosonic $\hat{O}_{i\alpha}$ and $\hat{O}_{i\alpha}^\dagger$ operators remove and add bosons to the site from an effective bosonic mean-field bath. We note that, for the simple model Hamiltonians we will be using below in this approach, the quasiparticle renormalization factor (or weight) Z is simply given by $Z_{i\alpha} = \langle O_{i\alpha} \rangle_s^2$.

4.3 Difficulties Obtaining Symmetry Broken Phases

In this section, we explain why the current implementation of mean-field theory fails to obtain proper symmetry broken phases. We use the example of the well-understood one-dimensional Hubbard model at half filling. Consider the Hamiltonian:

$$\hat{H} = \frac{U}{2} \sum_i (\hat{N}_i^2 - \hat{N}_i) - \sum_{i,\sigma} t (\hat{c}_{i,\sigma}^\dagger \hat{c}_{i+1,\sigma} + \hat{c}_{i+1,\sigma}^\dagger \hat{c}_{i,\sigma}) \quad (4.10)$$

where i is the site index, there is a single orbital per site, there are two spin channels per site, and we consider the case where we are at half filling ($\langle \hat{N}_i \rangle = 1$). The ground state is well-known. For $U = 0$, the ground state is non-magnetic and metallic. For $U > 0$ but finite, the ground state is insulating and shows anti-ferromagnetic correlations [58] but has finite quasiparticle weight $Z > 0$.

The $U = 0$ and $U \gg |t|$, the model's solutions are well-described by existing slave-particle mean-field implementations. For the intermediate region $U \sim |t|$, we are aware of no published study using recent slave-spin, slave-rotor or other formalisms from the same family that has correctly obtained the correct AFM phase for this model. Namely, the AFM solution does not appear to be a self-consistent ground state solution of the spinon+slave coupled Hamiltonians. In addition to being annoying, this is very worrisome since even a simple uncorrelated approach such as Hartree-Fock easily delivers an AFM ground state.

To understand where the problem lies, consider the spinon Hamiltonian of Eq. (4.7) and how one would achieve symmetry breaking, e.g.,

spin symmetry breaking and ordering, due to electron interaction effects. Since the electron interaction is handled by the slave sector, the only quantities that can be affected by the slave calculation that then feed into the spinon Hamiltonian are the Lagrange multipliers $h_{i\alpha}$ and the rescaling factors $\langle \hat{O}_{i\alpha}^\dagger \hat{O}_{i'\alpha'} \rangle_s$ of the spinon hopping.

In the simplest slave treatment, we have a single slave particle on the site: for example, the slave-number or slave-rotor treatments. In such a case, the α label is nil so our Lagrange multipliers are only indexed by site h_i and the rescaling factors as well $\langle \hat{O}_i^\dagger \hat{O}_{i'} \rangle_s$. Obviously, no spin symmetry breaking is possible in the spinon sector since these variables do not depend on spin in any way.

When we move to more elaborate slave-particle models where there are different slave modes for the different spin channels, then one can imagine that symmetry breaking is possible. For example, in our single orbital per site 1D Hubbard model, when we have one slave-particle for each spin channel, then $\alpha = \sigma$. We could now imagine that the $h_{i\sigma}$ shift the on-site energies of the orbitals in such a way to break spin symmetry, or that the hopping rescaling factors are also spin dependent. In practice, however, we have not found this to be the case: starting from a strongly symmetry broken initial guess, the self-consistency cycle between spinon and slave sectors drives the system towards a paramagnetic solution and the two spin channels become equivalent. Any initial magnetization disappears upon self-consistent iteration.

We have analyzed this failure and discovered the following situation. If at some point the spinon system has broken spin symmetry on a site i with net spin up, then $h_{i\uparrow} > h_{i\downarrow}$ is what makes this true. However,

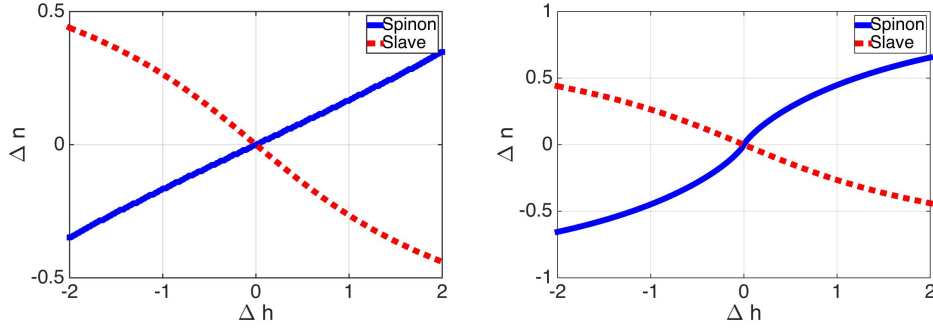


FIGURE 4.1: $\Delta n = n_{\uparrow} - n_{\downarrow}$ as a function of $\Delta h = h_{\uparrow} - h_{\downarrow}$ on one site of the 1D half-filled single band Hubbard model with $U = 2$ and $t = 1$. Upper figure is for the FM phase, and the lower figure for the AFM phase. The Δh dependence of the spinon and slave occupancies are shown separately. Self-consistency between the two requires zero occupancy difference.

although $h_{i\uparrow} > h_{i\downarrow}$ favors higher spin \uparrow occupancy in the spinon sector (due to the negative sign in front of $h_{i\alpha}$ in Eq. (4.7)), it favors higher occupancy of the spin \downarrow channel in the slave sector (positive sign of $h_{i\alpha}$ in Eq. (4.8)). The two effects fight each other, and the final self-consistent solution has $h_{i\uparrow} = h_{i\downarrow}$. An explicit example is provided by the 1D single-band Hubbard model at half filling where the dependence of slave and spinon occupancies on h are shown in Figure 4.1. These plots are generated by providing $\Delta n_i = n_{i\uparrow} - n_{i\downarrow}$ on some fixed site i as input to the slave problem which yields $\Delta h_i = h_{i\uparrow} - h_{i\downarrow}$ and $\langle \hat{O}_{i\sigma} \rangle$ which are then used to solve the spinon problem to get the spinon Δn_i . The figures clearly show that the only self-consistent solution where slave and spinon particle numbers match is for $\Delta h_i = 0$ which is the symmetric paramagnetic state.

4.4 Symmetry breaking fields

In this section, we show how manually adding small external symmetry breaking terms (“fields”) to the on-site energies can lead to electronic symmetry breaking and lower the energy of the self-consistent ground state. In the next section, we will justify this apparently *ad hoc* approach.

Adding additional symmetry breaking (“magnetic field”) terms $b_{im\sigma}$ to the on-site energies of the orbitals in the spinon Hamiltonian gives the simple modification

$$\begin{aligned} \hat{H}_f = & \sum_{im\sigma} \epsilon_{im\sigma} \hat{f}_{im\sigma}^\dagger \hat{f}_{im\sigma} - \sum_{i\alpha} h_{i\alpha} \sum_{m\sigma \in \alpha} \hat{f}_{im\sigma}^\dagger \hat{f}_{im\sigma} \\ & - \sum_{ii'\alpha\alpha'} \langle \hat{O}_{i\alpha}^\dagger \hat{O}_{i'\alpha'} \rangle_s \sum_{\substack{m\sigma \in \alpha \\ m'\sigma' \in \alpha'}} t_{imim'\sigma} \hat{f}_{im\sigma}^\dagger \hat{f}_{i'm'\sigma} \\ & - \sum_{im\sigma} b_{im\sigma} \hat{f}_{im\sigma}^\dagger \hat{f}_{im\sigma}. \end{aligned} \quad (4.11)$$

We do not modify the slave Hamiltonian in any way in this *ad hoc* approach.

Addition of non-zero symmetry breaking fields $b_{im\sigma}$ will modify the self-consistent solution to the spinon+slave problem. To gauge if this improves the solution, we monitor the total electronic energy and see if it is lowered due to symmetry breaking. The total energy is the expectation value of the original Hubbard Hamiltonian of Eq. (4.1) with respect to the approximate spinon+slave wave function $|\Psi_f\rangle|\Phi_s\rangle$, and is equal to

$$\begin{aligned} E_{total} = \langle \hat{H} \rangle = & \sum_i \langle \hat{H}_{int}^i \rangle_s + \sum_{im\sigma} \epsilon_{im\sigma} \langle \hat{f}_{im\sigma}^\dagger \hat{f}_{im\sigma} \rangle_f \\ & - \sum_{ii'mm'\sigma} t_{imim'\sigma} \langle \hat{f}_{im\sigma}^\dagger \hat{f}_{i'm'\sigma} \rangle_f \langle \hat{O}_{i\alpha}^\dagger \hat{O}_{i'\alpha'} \rangle_s. \end{aligned} \quad (4.12)$$

We now apply this approach to the one-dimensional single band Hubbard model at half filling of Eq. (4.10). Without loss of generality, we choose $b_{i\uparrow} = -b_{i\downarrow}$ to break spin symmetry on each site i . For ferromagnetic (FM) order, we choose aligned symmetry breaking fields between neighboring sites $b_{i+1,\sigma} = b_{i\sigma}$, while AFM order requires staggered fields $b_{i+1,\sigma} = -b_{i\sigma}$. Hence, the field strength b for spin up at one site is sufficient to specify the fields at all sites. We numerically solve the spinon+slave self-consistent equations using the single-site mean-field approximation described Section 4.2.

We begin our analysis with the most coarse-grained slave-boson representations that only describe the total electron count on each site (i.e., no information on the spin configuration). These are the slave-rotor and number-slave methods. The chief difference between them is that the number count on a site can be any integer in the slave-rotor method while the number-slave corrects this by only permitting the electron count to be among the physically allowed values (e.g., zero, one or two for the single band Hubbard model). Figure 4.2 show the dependence of the total energy and quasiparticle weight Z (i.e., renormalization factor) on the field strength b within the slave-rotor approach. For the slave-rotor, increasing b increases the total energy of both AFM and FM solutions: the non-magnetic solution is the preferred ground state. The strength of electronic correlations, measured by how much Z deviates from its non-interacting value of unity, also increases with b . This b dependence is opposite to what one would expect for the actual model system: a more spin-polarized system should have smaller number fluctuations as

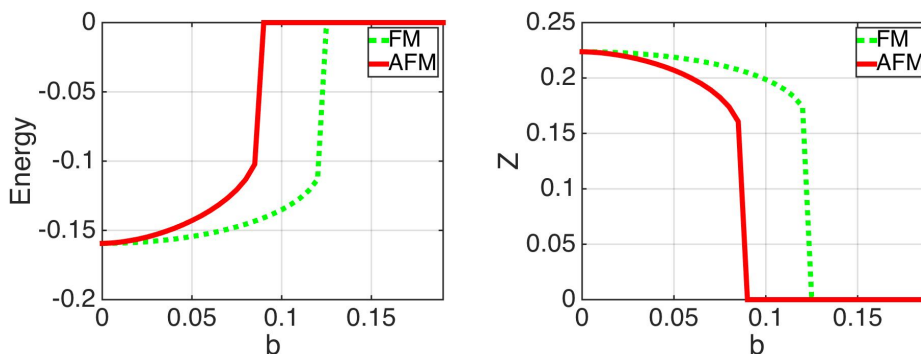


FIGURE 4.2: Total energy per site and quasiparticle weight Z (renormalization factor) versus symmetry breaking perturbation field strength b based on the slave-rotor method for the half-filled single-band 1D Hubbard model with $U = 2$ and $t = 1$.

occupancies are driven towards one or zero and the electron configuration becomes better described by a single Slater determinant. Finally, the slave-rotor predicts an abrupt transition to a Mott insulator at finite b which is peculiar (and wrong).

The number-slave results for total energy and Z versus b , displayed in Figure 4.3, are somewhat of an improvement over those of the slave-rotor but are still fundamentally flawed. The energy is still minimized by the non-magnetic solution at $b = 0$ (although the energy rises more gently with b) and Z drops with b (albeit more modestly). The failure of the slave-rotor and number-slave methods is tied to the fact that they do not consider the spin degree of freedom.

Due to the simplicity of the single-band Hubbard model, the only remaining slave model is the spin+orbital-slave approach (called “spin-slave” in the literature [15, 16, 18]). On each site, the each spin channel has its own dedicated slave particle. The energy versus b plot in Figure 4.4 shows that we obtain an AFM ground state since a minimum

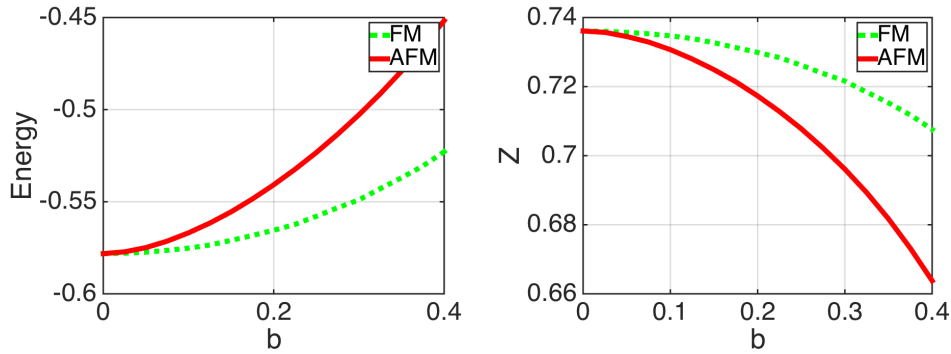


FIGURE 4.3: Total energy per site and Z versus field strength b for the number-slave method for the single-band 1D Hubbard model at half filling with $U = 2$ and $t = 1$.

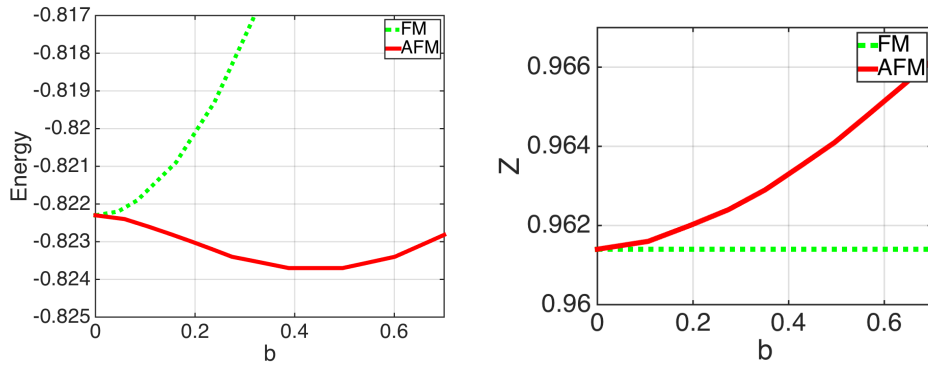


FIGURE 4.4: Total energy per site and Z versus field b for the spin+orbital-slave approach for the single-band 1D Hubbard model at half filling with $U = 2$ and $t = 1$. Unlike the number-slave and slave-rotor, correlations decrease with increasing b for the AFM phase and slowly increase with b for the FM phase.

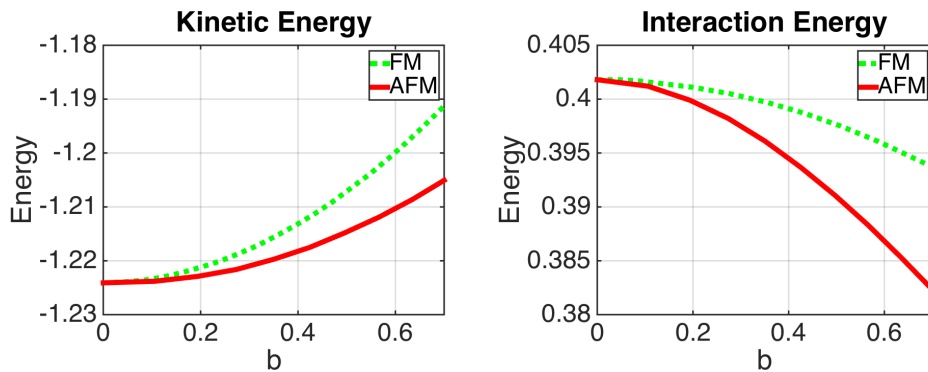


FIGURE 4.5

appears at finite b . The figure also shows that the degree of electronic correlation is reduced with increasing b (and increasing strength of AFM order) as the occupancies get closer to zero and one: the system becomes less strongly interacting as b is strengthened. This is what we expect: with increasing AFM spin-polarization, the electronic configuration of the system is driven to extremes of occupation (zero or one for each spin channel) meaning that one can describe the system more accurately with a single (non-interacting) Slater determinant. More details on the energetic behavior versus b is provided by Figure 4.5 where the individual components of the total energy are shown versus b . The interaction energy (Hubbard U term) is reduced by the spin symmetry breaking since for both FM and AFM order the occupancies move away from half-filling where occupancy fluctuation is largest. The band (hopping or kinetic) energy rises with b due to the splitting of bands upon symmetry reduction. Both behaviors are generic and as expected. However, the reason the AFM order shows a minimum total energy versus b is due to the fact that Z becomes larger with b in this case: a larger Z (i.e., larger $\langle O \rangle$) will enhance hopping and widen the bands and thus offset the reduction of total band energy due to the creation of spin polarization.

The take-home message of this section is that the introduction of symmetry breaking fields can succeed in stabilizing symmetry-broken ground states due to electronic correlations as long as the slave approach being used is able to describe the symmetry breaking degree of freedom (spin in the 1D single band Hubbard model). We are thus motivated to improve upon the *ad hoc* nature of the approach and put it on a firmer theoretical in the next section.

4.5 Self-consistent total energy approach

In this section, we justify the successful but *ad hoc* approach of the previous section. Namely, we describe a total energy functional that can be applied to any type of slave-particle problem and which permits easy incorporation of the various types of desired constraints. Specifically, we show that the slave-particle approach is a variational approach to the interacting ground-state problem, and we provide an explicit form for the variational energy functional. We also show that this viewpoint provides significant practical benefits for efficient solution of the self-consistency problem between slave and spinon sectors.

The form of the energy functional F is given by

$$F = E_{total} + \text{constraints}$$

where E_{total} is from Eq. (4.12) and the constraint terms are enforced by Lagrange multipliers.

Prior to the introduction of symmetry breaking fields, the constraints we have enforced are that $\langle N_{i\alpha} \rangle_s = \langle \hat{n}_{i\alpha} \rangle_f$ as well as the normalization of the spinon and slave wave functions $\langle \Psi_f | \Psi_f \rangle = \langle \Phi_s | \Phi_s \rangle$. To incorporate symmetry breaking fields, we choose to parametrize the functional F by *target* spinon occupancies $\nu_{im\sigma}$: these numbers are the occupancies that we are constraining the spinons to obey, i.e., the constraints are $\langle n_{im\sigma} \rangle_f = \nu_{im\sigma}$. The associated Lagrange multipliers are $b_{im\sigma}$. Hence the energy

functional has the form, where we write out E_{total} explicitly,

$$\begin{aligned}
F(\{\nu_{im\sigma}\}) = & \sum_i \langle \hat{H}_{int}^i \rangle_s + \sum_{im\sigma} \epsilon_{im\sigma} \langle \hat{f}_{im\sigma}^\dagger \hat{f}_{im\sigma} \rangle_f \\
& - \sum_{ii'mm'\sigma} t_{imim'\sigma} \langle \hat{f}_{im\sigma}^\dagger \hat{f}_{i'm'\sigma} \rangle_f \langle \hat{O}_{i\alpha}^\dagger \hat{O}_{i'\alpha'} \rangle_s \\
& - \lambda_f [\langle \Psi_f | \Psi_f \rangle - 1] - \lambda_s [\langle \Phi_s | \Phi_s \rangle - 1] \\
& - \sum_{i\alpha} h_{i\alpha} [\langle \hat{n}_{i\alpha} \rangle_f - \langle \hat{N}_{i\alpha} \rangle_s] \\
& - \sum_{im\sigma} b_{im\sigma} [\langle \hat{n}_{im\sigma} \rangle_f - \nu_{im\sigma}]. \quad (4.13)
\end{aligned}$$

The Lagrange multipliers λ_f and λ_s enforce normalization of the spinon and slave wave functions, respectively. The $h_{i\alpha}$ enforce particle number matching between slave and spinon sectors. The $b_{im\sigma}$ enforce spinon particle matching to target values. As expected, when the constraints are obeyed, $F = E_{total}$.

The point of having an energy functional is that the minimizing variational conditions, which generate desired eigenvalue problems, are easily derived by differentiation. In addition, the value of F provides a variational estimate of the ground state energy. Setting the derivative versus $\langle \Psi_f |$ to zero gives the spinon eigenvalue equation

$$0 = \frac{\delta F}{\delta \langle \Psi_f |} = H_f | \Psi_f \rangle - \lambda_f | \Psi_f \rangle$$

where the spinon Hamiltonian is that of Eq. (4.11) which includes the symmetry breaking fields. Similarly, the minimum condition for $|\Phi_s\rangle$ gives a slave eigenvalue problem with the slave Hamiltonian of Eq. (4.8).

The above formalism shows that, once all the constraints are obeyed,

$F(\{\nu_{im\sigma}\}) = E_{total}(\{\nu_{im\sigma}\})$. The remaining task is to search over the target occupancies $\nu_{im\sigma}$ to find the minimum total energy. While theoretically straightforward, in practice such an approach is difficult and inefficient because for each specified $\{\nu_{im\sigma}\}$, one must find the fields $b_{im\sigma}$ that enforce those particular target occupancies: this requires solving the spinon+slave problem a great many times.

Practically, it is better to use the $b_{im\sigma}$ as the independent variables and to minimize the energy over the (formally, this corresponds to a Legendre transformation of F). Hence, we now view $\nu_{im\sigma}$ as whatever mean spinon occupancies are generated by solution of the spinon+slave problem at fixed $\{b_{im\sigma}\}$ which makes that corresponding constraint form always vanish. Hence, in what follows, we will use the symmetry breaking fields as independent variables and consider the total energy functional $F(\{b_{im\sigma}\})$. Since we will always be obeying the key constraints for a physical solution, $F(\{b_{im\sigma}\}) = E_{total}(\{b_{im\sigma}\})$ will be true. Hence, minimization of the total energy versus $\{b_{im\sigma}\}$ will coincide with minimization of F .

4.6 Simplified and more efficient slave-particle approach

Up to this point, the slave-particle approaches we have developed require self-consistency between spinon and slave sectors in a specific manner: not only do the spinon expectations renormalize slave hopping terms (and conversely for slave expectations and spinon hoppings), but a shared set of Lagrange multipliers $h_{i\alpha}$ enforce particle number matching $\langle \hat{n}_{i\alpha} \rangle_f =$

$\langle \hat{N}_{i\alpha} \rangle_s$. The process of finding the $h_{i\alpha}$ is numerically challenging: the $h_{i\alpha}$ appear with opposite signs in the spinon H_f and slave H_s Hamiltonians meaning that increasing $h_{i\alpha}$ decreases $\langle \hat{n}_{i\alpha} \rangle_f$ but increases $\langle \hat{N}_{i\alpha} \rangle_s$. Our general observation is that this “fighting” over $h_{i\alpha}$ between the slave and spinon sectors leads to a time-consuming self-consistent process requiring many iterations to reach convergence.

Accelerating this process requires a simple change of variables that is motivated by three related observations: (i) in the total energy functional of Eq. (4.13), the spinon and slave number constraints are not treated symmetrically because the spinons have the added $b_{im\sigma}$ terms, (ii) in the spinon Hamiltonian of Eq. (4.11), we can add the $h_{i\alpha}$ and $b_{im\sigma}$ terms together into a single term whereas the slave Hamiltonian of Eq. (4.8) only has the $h_{i\alpha}$ terms, and (iii) in the end, these Lagrange multipliers $h_{i\alpha}$ and $b_{im\sigma}$ do not appear in the total energy so rearranging them in various ways does not change the total energy.

For the spinon Hamiltonian, we consider instead the new symmetry breaking field given by the sum $B_{im\sigma} = h_{i\alpha} + b_{im\sigma}$. The spinon Hamiltonian is now

$$\begin{aligned} \hat{H}_f = & \sum_{im\sigma} \epsilon_{im\sigma} \hat{f}_{im\sigma}^\dagger \hat{f}_{im\sigma} - \sum_{im\sigma} B_{im\sigma} \hat{f}_{im\sigma}^\dagger \hat{f}_{im\sigma} \\ & - \sum_{ii'\alpha\alpha'} \langle \hat{O}_{i\alpha}^\dagger \hat{O}_{i'\alpha'} \rangle_s \sum_{\substack{m\sigma \in \alpha \\ m'\sigma' \in \alpha'}} t_{imim'\sigma} \hat{f}_{im\sigma}^\dagger \hat{f}_{i'm'\sigma} \quad (4.14) \end{aligned}$$

while the slave Hamiltonian is unchanged

$$\hat{H}_s = \sum_i \hat{H}_{int}^i + \sum_\alpha h_{i\alpha} \hat{N}_{i\alpha} - \sum_{ii'\alpha\alpha'} \left[\sum_{\substack{m\sigma \in \alpha \\ m'\sigma' \in \alpha'}} t_{im'i'm'\sigma} \langle \hat{f}_{im\sigma}^\dagger \hat{f}_{i'm'\sigma} \rangle_f \right] \hat{O}_{i\alpha}^\dagger \hat{O}_{i'\alpha'}.$$

The slave Hamiltonian H_s no longer shares a common Lagrange multiplier with the spinon Hamiltonian H_f .

Operationally, this means that when we solve the slave Hamiltonian problem, we are given specified $\langle \hat{n}_{i\alpha} \rangle_f$ as input, and we solve the slave problem while adjusting the $h_{i\alpha}$ so as to ensure that the slave-particle counts match the input: $\langle \hat{N}_{i\alpha} \rangle_s = \langle \hat{n}_{i\alpha} \rangle_f$. However, when solving the spinon problem in the presence of symmetry breaking fields $B_{im\sigma}$, there is no need to do particle number matching: the Lagrange multiplier $B_{im\sigma}$ simply make the spinon particle counts match some free floating values. In this way, particle number matching between the slave and spinon sector is decoupled which *greatly* simplifies the self-consistency process. Put another way, the symmetry breaking fields $B_{im\sigma}$ specify a set of desired spinon particle counts $\{\nu_{im\sigma}\}$, and the slave sector is required to match this particle numbers via the $h_{i\alpha}$ Lagrange multipliers.

We find that this simplified approach, which is equivalent to the standard approach of having $h_{i\alpha}$ appear in both Hamiltonians, is much more efficient in numerical calculations as it greatly speeds up self-consistency. In this new approach, one achieves rapid self-consistency for a given set of $\{B_{im\sigma}\}$ which specify the spinon Hamiltonian and the target spinon occupancies $\nu_{im\sigma}$. One can then minimize $E_{total}(\{B_{im\sigma}\})$ over the $B_{im\sigma}$ to

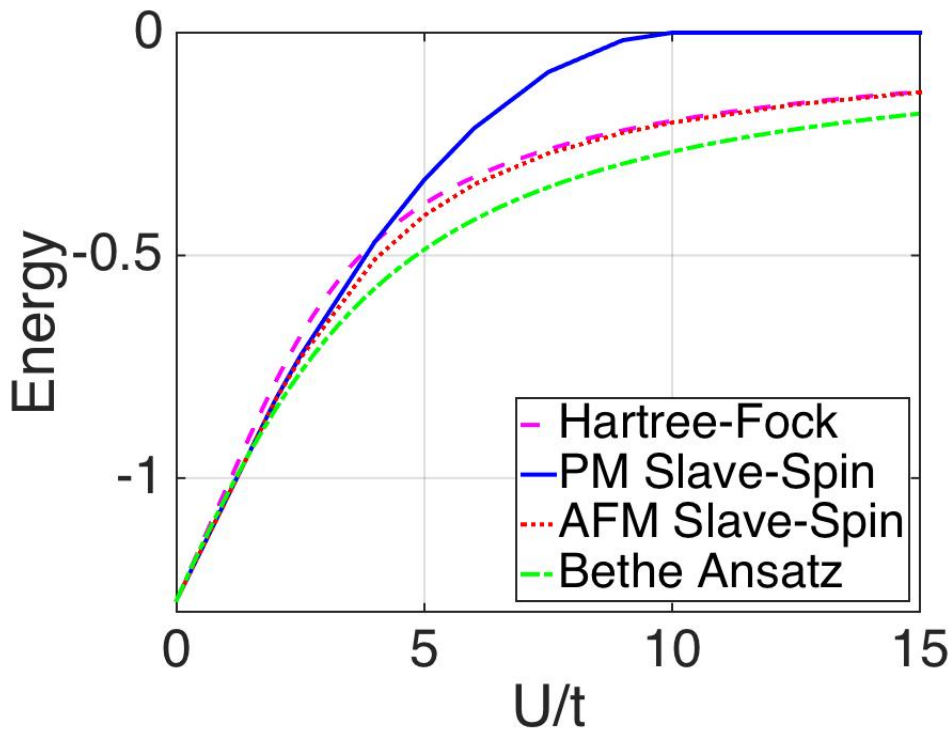


FIGURE 4.6: Comparison of the ground state energies (in units of t) for the single-band 1D Hubbard model at half filling based on the AFM Hartree-Fock solution, the PM slave-spin solution, the symmetry broken (AFM) slave-spin ground state solution, and the exact Bethe Ansatz (AFM) solution as calculated by the method of Ref. [59].

find the symmetry-broken ground state. In our experience, this new approach requires ~ 5 -10 times fewer self-consistent steps to reach the same level convergence.

Using this method, we can rapidly scan over B in a stable, self-consistent way to obtain ground state energies. Figure 4.6 shows the dependence of the ground state energy of the half-filled single-band 1D Hubbard model as a function of U/t : for each U/t , we easily scan over the new symmetry breaking field strength B to find the AFM ground state energy. The figure shows energy versus U/t for the AFM state as well as the $B = 0$ non-magnetic solution compared to the exact Bethe ansatz solution for

this problem.[58] Overall, the comparison between the AFM slave-spin solution (which is insulating in the spinon sector) and the exact Bethe ansatz is satisfactory given the simplicity of the single-site mean field slave model used here. As expected, the AFM slave-spin method becomes very much like AFM Hartree-Fock in the large U/t limit of very strong spin polarization since both approaches essentially describe the system as a single Slater determinant. We note that the non-magnetic ground state has an incorrect evolution from a metallic system at small U/t to a Mott-insulating phase at $U/t \geq 10$.

4.7 Conclusion

We've shown how occupation-based slave particle methods can be used to obtain spontaneously symmetry-broken electronic phases based on a total-energy approach. We have described and tested our ideas on the classic 1D Hubbard model Hamiltonian and showed both the difficulty of breaking symmetry without extra fields or a Hund's J . Furthermore, we have shown how to enable symmetry breaking via the use of auxiliary symmetry breaking fields in a self-consistent way that greatly lowers the computational burden and stability from the standard slave-particle calculation. Further, we have demonstrated that in order to obtain spontaneously symmetry-broken phases in the spinon sector, the slave-sector must be allowed to break the corresponding symmetry explicitly by having different slave-modes for the different degrees of freedom which may undergo symmetry breaking.

Chapter 5

Ionic Potential and Band Narrowing as a Source of Orbital Polarization in Nickelate/Aluminate Superlattices

In this chapter we explore the underlying mechanism behind orbital polarization in another interface, that of $\text{NdNiO}_3/\text{NdAlO}_3$. The experimental reason to study this material was to see whether, in a thin film, the long range NdNiO_3 order is suppressed for thin enough NdNiO_3 layer thickness. Our experimentalist collaborators have shown (currently under second round of review at Phys. Rev. X, Disa, Georgescu et al.), this is the case. This material also seems to be a good testing ground for our DFT+Slave calculation on a heterostructure, as DFT predicts an orbital polarization in reverse compared to what experiment predicts. This difficulty with DFT, however, is also what makes the application

of the slave-particle methods particularly relevant. In conjunction with phenomena DFT did predict accurately, this materials system shows the importance of simple, beyond-band-theory calculations.

5.1 Methodology

The theoretical calculations have been done within the density-functional-theory (DFT) approach using the Quantum Espresso software [22], using the generalized gradient approximation (GGA) in the PBE form [21], and ultrasoft pseudo potentials as implemented in the Quantum Espresso package [23]. All the super cells in our simulations have the form of an infinite periodic superlattice with formula $(\text{NNO})_m/(\text{NAO})_n$ along the (001) direction, where $m = 1, 2$ and $n = 3, 4$ with the condition that $m + n$ is even in order to allow for full relaxation of the octahedral rotations in the simulation supercell. The experimental system is grown on a LaAlO_3 substrate which has an experimental lattice constant of $a_{\text{LAO}} = 3.79 \text{ \AA}$, while $a_{\text{NAO}} = 3.74 \text{ \AA}$ and $a_{\text{NNO}} = 3.81 \text{ \AA}$. Our experimental collaborators have noted relaxation of the lattice unit cell compared to the substrate unit cell, leading to an estimated compressive strain on the NNO layers of around 0.5% on the NNO. As we will show, this small strain has very little effect on orbital polarization as computed by DFT in the context of this heterostructure. We have performed relaxation calculations by using a 1×1 in-plane unit cell in the xy plane as well as $c(2 \times 2)$ relaxation calculations.

In order to define orbital polarization of the e_g bands, we use the simple definition

$$r = \frac{2 - n_{3z^2-r^2}}{2 - n_{x^2-y^2}} \quad (5.1)$$

which measured the ratio of holes in the two different e_g orbitals (n_i is the electron count in orbital i). We choose to measure orbital polarization as a function of the number of holes per orbital in order to compare directly with experiments that measure holes (unoccupied states) via x-ray absorption spectroscopy (XAS).

In order to get an average local (on-site) energy per orbital, we first calculate the projected density of states (PDOS) for each orbital and then perform integrals. For an orbital labeled by $nm\sigma$, the average energy is given as

$$\bar{E}_{nm\sigma} = \frac{\int_{-\infty}^{\infty} PDOS_{nm\sigma}(E) \cdot E \cdot dE}{\int_{-\infty}^{\infty} PDOS_{nm\sigma}(E) \cdot dE}. \quad (5.2)$$

To focus on the main aspects of the physics around the Fermi level, particularly that of the d-bands, we have found it helpful to build a tight binding model. Since bulk NdNiO_3 is a charge-transfer insulator, we include the O 2p orbitals explicitly in our tight-binding model. Hence, we have both Ni 3d states and the Oxygen 2p states for the $\text{NNO}_m/\text{NAO}_n$ superlattice in our p-d model. The Wannierization process used to find these orbitals was performed using the open-source code Wannier90 software [60] to post process the results of our DFT calculations.

Finally, to model the effects of band narrowing on orbital polarization, we have used the slave-particle approach as described in previous chapters for the p-d model while keeping the on-site energies at the value calculated from DFT (this is equivalent to setting all $B = 0$ as defined in

Structure	Lattice Constant (strain)	$n_{3z^2-r^2}$	$n_{x^2-y^2}$	r
1x1	3.71 (0.5% compressive)	0.634	0.715	1.28
c(2x2)	3.79 (1% tensile)	0.626	0.719	1.33
c(2x2)	3.71 (1 % compressive)	0.631	0.715	1.29

TABLE 5.1: Electron occupation and orbital polarization of e_g orbitals as a function of strain and with and without octahedral distortions based on DFT calculations.

Chapter 4).

5.2 Results

Within standard crystal-field theory, orbital polarization on the cation in a perovskite is driven by structural distortions of the cation-O bonds around the cation. For example, strain can lead to such distortions. At an interface, another source of orbital polarization that is often discussed in the literature is from quantum confinement: electrons are confined in the out-of-plane superlattice direction by insulating layers (in our example) when compared to unimpeded motion in the in-plane directions.

Based on our DFT calculations for these NNO-NAO superlattices, we notice that the effect of octahedral distortions and experimental strain ranges of $\pm 0.5\%$ on the orbital polarization is quite small. (The sign of the strain depends on whether NNO is strained epitaxially to the LAO substrate or relaxes to that NAO lattice parameter if epitaxy is lost.) Table 5.1 shows numerical results for a few variant calculations. In all cases, $r \approx 1.3$ which is not only qualitatively different from the experimentally measured $r = 0.9$ but also in the opposite direction (computed $n_{x^2-y^2} > n_{3z^2-r^2}$ while the measured $n_{3z^2-r^2} > n_{x^2-y^2}$). We note from table 5.1 that

U(Ni)	U(O)	$n_{3z^2-r^2}$	$n_{x^2-y^2}$	r	$\bar{E}_{3z^2-r^2}$	$\bar{E}_{x^2-y^2}$	$\Delta\bar{E}$
0	0	0.558	0.641	1.23	-2.712	-2.471	-0.241
3	0	0.554	0.663	1.32	-2.745	-2.717	-0.028
6	0	0.539	0.693	1.50	-2.696	-3.093	0.397
0	3	0.541	0.627	1.23	-2.636	-2.389	-0.247
0	6	0.523	0.612	1.23	-2.568	-2.316	-0.252

TABLE 5.2: Electron occupation numbers and average energies for Ni e_g orbitals for the $(\text{NNO})_1/(\text{NAO})_4$ 1×1 structure calculation for different values of U within DFT+U theory.

within a range of 2% in strain, the change of orbital polarization for the fully relaxed $c(2\times 2)$ structure is very small and the change when adding or removing octahedral rotations (1×1 versus $c(2\times 2)$) is also small. This allows use the 1×1 structure for the rest of the chapter as a model system to understand orbital polarization in the superlattice.

Since nickelates are electronically correlated materials, an obvious next step is to include some type of local interaction effects within the DFT+U approximation by adding a Hubbard U to the Ni $3d$ orbitals. For reasons that will become obvious below, we separately apply a Hubbard U to the O $2p$ orbitals as well.

Adding a U to the Ni $3d$ orbitals does not drive the orbital polarization towards experimental results. When the U is applied to the Ni $3d$ in DFT+U calculations, it further increases the orbital polarization, exacerbating the trend above. This is something we expect since the correction to the on-site energies for orbital $nlm\sigma$ in DFT+U takes the form

$$\epsilon_{nlm\sigma} = \epsilon_{nlm\sigma}^{U=0} + U \left(\frac{1}{2} - n_{nlm\sigma} \right) \quad (5.3)$$

which has a tendency to push down in energy states that are more than

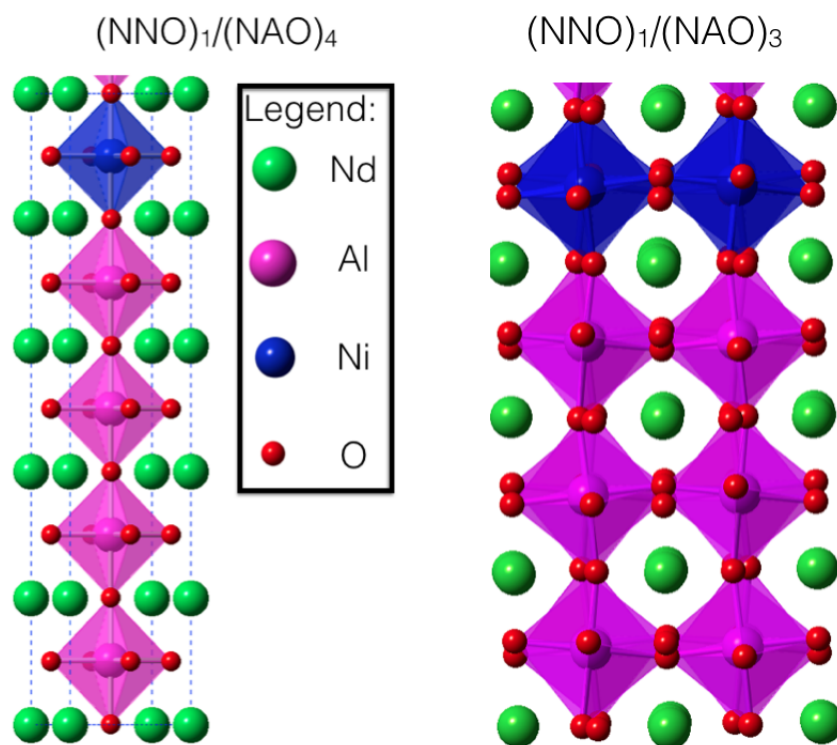


FIGURE 5.1: 1×1 structure of $(\text{NNO})_1/(\text{NAO})_4$ and fully relaxed $c(2 \times 2)$ $(\text{NNO})_1/(\text{NAO})_3$ as simulated in Quantum Espresso. We only use 3 layers of NAO in order to have an even number of octahedra and allow for octahedral distortions

half filled (and push up in energy states below half filling). This generally exaggerates the pre-existing patterns of occupations at $U = 0$. Since both e_g states are more than half-filled, their occupation number tends to be further increased by the addition of a U and their energies are reduced. As a by product, this ends up reducing the p-d energy splitting.

We proceed to add a U to the O $2p$ orbitals as a numerical exercise and thought experiment. Since DFT+ U in effect only changes the on-site energies, this results in an effective increase in the p-d splitting by lowering the relative energy levels of the Oxygen p states (which are much more than half filled). As expected, this decreases the orbital occupancy of the e_g orbitals by reducing their covalent bonding. This is, as it will become clear later in this chapter, due to the band narrowing induced by the increase in p-d splitting.

Looking at the average energies in Table 5.2, we observe something interesting. The on site energies at $U = 0$ show a splitting of $\bar{E}_{x^2-y^2} - E_{3z^2-r^2} = 0.24eV$. This compares well with the experimental value of $\bar{E}_{x^2-y^2} - E_{3z^2-r^2} = 0.3eV$. What is puzzling is that the $3z^2 - r^2$ orbital has a lower energy but has a smaller occupancy than the $x^2 - y^2$ orbital. Hence, this is an unusual case where the DFT occupancies are wrong but the on site orbital energies are correctly ordered (i.e., the self-consistent potential seems to be correct but the occupancies coming from that potential are not correct).

To better understand what is happening, we return to our model 1×1 system, and plot the e_g projected density of states (PDOS). As we can see in Figure the $x^2 - y^2$ band is significantly wider than the $3z^2 - r^2$ band, despite the already discussed marginal effect of strain. To explain

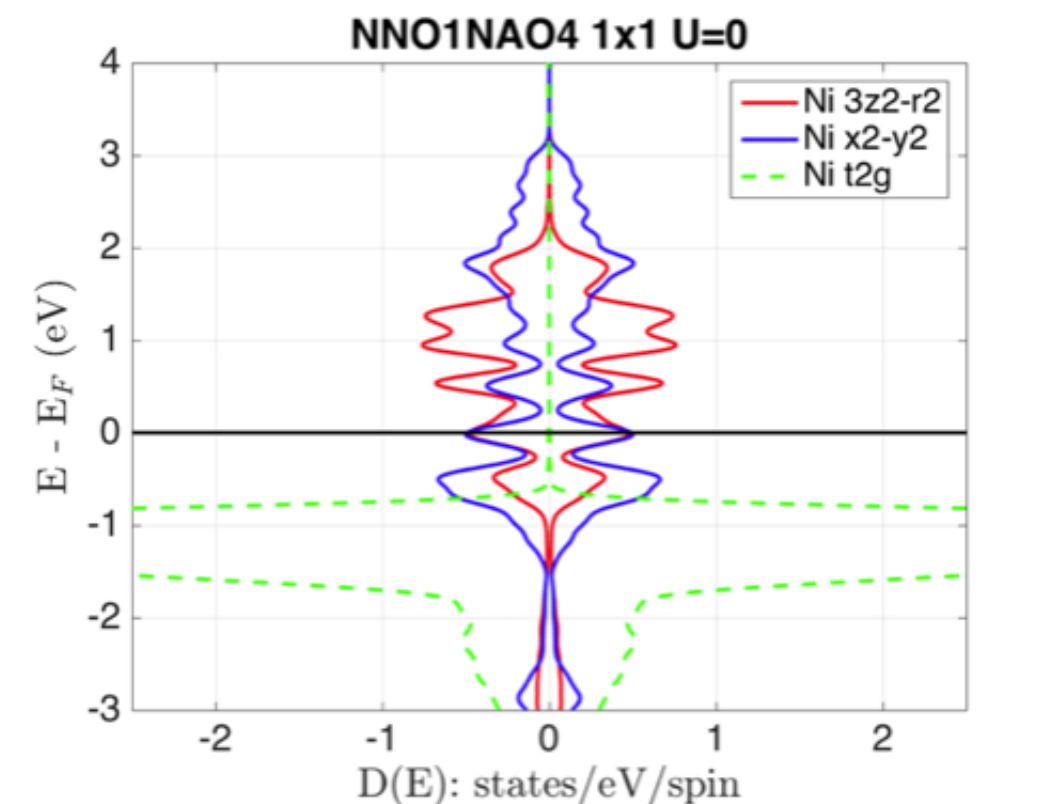


FIGURE 5.2: Projected density of states of the Ni e_g orbitals for the $(\text{NNO})_1/(\text{NAO})_4$ heterostructure.

how the confinement leads to band narrowing and less covalence, even in the context in which bond lengths are not affected, we appeal to a simple physical picture shown in Figure 5.3. The picture shows that even for identical orbital energies and inter-orbital hoppings, confinement in the superlattice direction will reduce electron propagation. This in turn narrows the bands. A corollary of this band width reduction is that the Ni $3z^2 - r^2$ and O $2p$ orbitals mix less (i.e., the associated conduction bands have stronger Ni $3d$ character) which is what is meant by reduced covalence.

While the above picture explains the difference in covalence and the origin of the band narrowing, it does not explain why the orbital occupancies should differ (and opposite to those in experiment) nor why the on-site energies of the Ni e_g orbitals are different (and match experiment). We will deal with the two issues separately as they are interrelated but distinct and require separate types of analysis.

The on-site energy difference can be explained by the different ionicity of the two materials. Namely, NAO is a wide gap insulator and should be quite ionic: the Al cation in NAO should be very solidly in the $3+$ state due to the high energy of its unoccupied orbitals. On the other hand, NNO is much more covalent since the states near the Fermi energy have strongly mixed Ni $3d$ -O $2p$ character: we expect the Ni to be less close to a formal $3+$ charge state and closer to $2+$. The point is not the precise values, but simply that Al will be more positively charged than Ni. From here, the path forward is directed by basic electrostatics: as we near the Al site, its more positive charge will make the filled states of the nearby oxygens become lower in energy (a Madelung potential effect)

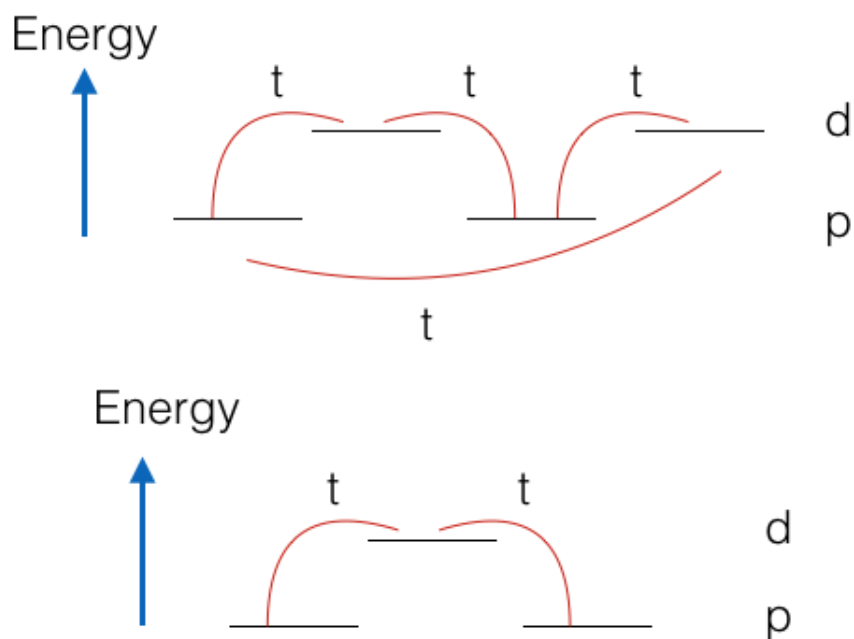


FIGURE 5.3: Simplified picture of how confinement changes inter-orbital hoppings, band widths, and covalence. Top: a p-d Hamiltonian that includes alternating higher and lower energy orbitals in a periodic way (similar to bulk NNO in any axial direction or Ni $x^2 - y^2$ orbital and in-plane oxygens in NNO/NAO). Bottom: a similar Hamiltonian with the same hopping terms and on-site energy differences that, however is not periodic due to the confinement (insulating layers surround this subsystem). This describes the $3z^2 - r^2$ orbital in the $(\text{NNO})_1/\text{NAO}$ system. While the immediate environment around the d orbitals is the same, the hoppings to father sites are not and this modifies band widths and covalence.

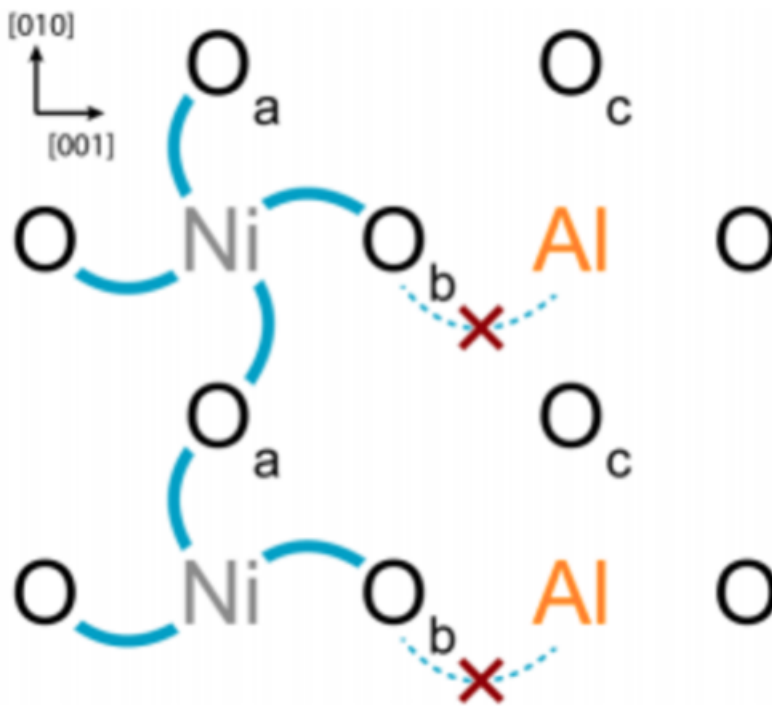


FIGURE 5.4: Schematic representation of the NNO/NAO interface. Note that hopping is energetically costly (i.e., forbidden) onto the Al in the NAO from O_b (due to the high energy of the local states on Al). As one proceeds away from the NiO₂ layer, the oxygens become more occupied as the environment becomes more ionic, i.e. $n(O_a) < n(O_b) < n(O_c)$. Image from Disa, Georgescu et al (under review).

$n(O_a)$	$n(O_b)$	$n(O_c)$
1.68	1.78	1.92

TABLE 5.3: Occupation numbers for oxygen apical $2p$ orbitals ($2p$ orbitals pointing along the local cation-O-cation direction on each oxygen). Oxygens are defined by Figure 5.4. The increased occupancy going from NNO to NAO indicating increased ionicity & decreased covalence.

and thus more occupied. This physical picture is directly supported by our DFT results. Table 5.3 shows that, indeed, as we approach the Al site, the O anion $2p$ states become systematically more occupied by electrons.

The anisotropic layout of ionicities can also affect the Ni orbitals. The difference in ionicity should reflect itself in an anisotropic electrostatic potential profile near the Ni site. In order to isolate this effect, we have compared a number of idealized model calculations: a 1×1 10-atom per unit cell $(\text{NNO})_1/(\text{NAO})_1$ superlattice with the same lattice constant in the x-y plane as our 1×1 $(\text{NNO})_1/(\text{NAO})_4$ superlattice as well as a 10-atom per unit cell 1×1 $(\text{NNO})_2$ 'superlattice' (i.e., pure NNO). We did not allow any relaxations of these model systems and enforced full cubic symmetry for each oxygen octahedron. We note that we obtain the same $\Delta E = 0.24 \text{ eV}$ in the $(\text{NNO})_1/(\text{NAO})_1$ supercell as in the $(\text{NNO})_1/(\text{NAO})_4$ supercell, proving that the energy splitting is not due to structural distortions in the full superlattice. Next, we take average of the potential in the x-y plane in both 10 atom theoretical superlattices, obtaining a 1-D potential for both superlattices. We can then subtract the potentials, $V_{\text{NNO}/\text{NAO}} - V_{\text{NNO}/\text{NNO}}$, and plot the resulting potential difference. The resulting plot (Figure 5.5) shows that the average potential

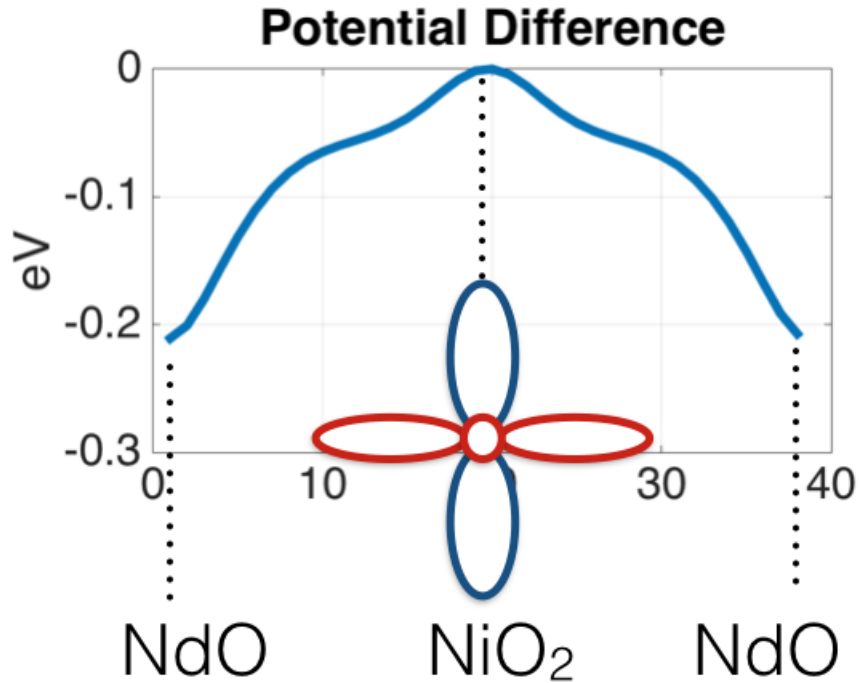


FIGURE 5.5: Potential difference averaged in the x-y direction in the NNO layer between NNO/NAO and NNO/NNO as a function of z position offset from the Ni (arbitrary horizontal linear axis units). The $3z^2-r^2$ orbital (red) samples a lower potential than the x^2-y^2 orbital (blue), leading to an energy splitting between the two orbitals.

sampled by the $3z^2-r^2$ potential is lower in energy than that of the x^2-y^2 orbital, as expected from the fact that the $3z^2-r^2$ orbital points towards the more positive Al, and thus explaining the electrostatic origin of the energy splitting.

We now summarize our understanding of what is happening in the material. In brief:

- the ΔE energy splitting between the two e_g orbitals is mainly due to the different electrostatic potential sampled by the two different e_g orbitals. The potential difference stems from the different ionicity of Al and Ni. ΔE matches well with experiment in the full

supercell calculation (0.27 eV in theory vs 0.3 eV in experiment)

- the $3z^2 - r^2$ is narrower than the $x^2 - y^2$ band due to the quantum confinement effect along the superlattice direction since NAO is a wide gap insulator.

The final aspect to be understood is the electron occupancy. A basic fact we must keep in mind is that the final electron occupancy on an atom is determined by both the on-site energies on that atom as well as the inter-atomic hopping terms to nearby neighbors (in a tight-binding view). We know, however, that the electronic bands in nickelates are broader in DFT calculations than in experiment due to electronic correlations. For example, bulk LaNiO_3 has $m^*/m_{DFT} \approx 3.0$ [13]. We then theorize that the discrepancy in orbital occupation could be due to the fact that our bands are much broader than in experiment.

The basic idea is simple and is highlighted in Figure 5.6 (see the caption for the explanation of the basic mechanism). In what follows, we will flesh out and verify this hypothesis.

5.3 Test Case: Band Narrowing in SrVO_3

Before applying the DFT+Slave-Boson method as above to the superlattice, we test this method on a transition metal oxide, namely SrVO_3 (SVO), where the band structure is known. We pick this material as its e_g bands are empty, while the t_{2g} bands at the Fermi level are degenerate. Further, SrVO_3 is a correlated metal [14, 61], making it an ideal testing ground for our theory.

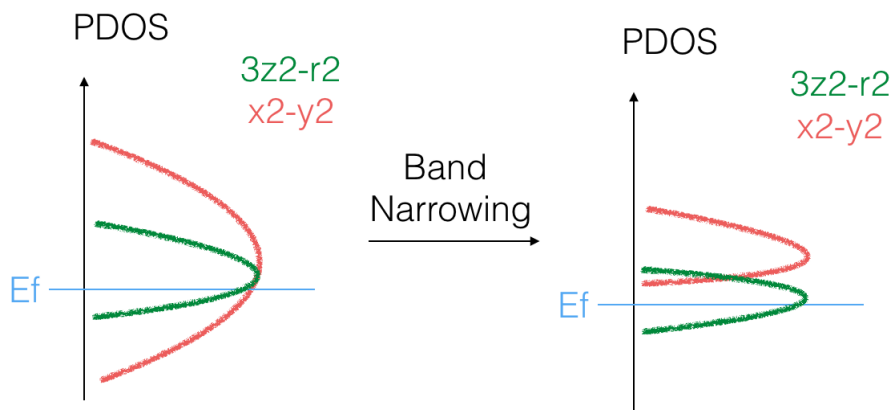


FIGURE 5.6: Simple physical picture of how band narrowing can reverse the direction of orbital polarization. Left: the average energy of the $3z^2 - r^2$ is lower than that of $x^2 - y^2$, however the $x^2 - y^2$ is quite broad and thus more of it is under the Fermi level, leading to a higher occupancy. Right: narrowing both bands by a significant amount leads to a higher occupancy of the band that has an average lower energy. In the limit of bands of zero width, the $x^2 - y^2$ would have zero occupancy, and we would have maximum orbital polarization.

Our slave-boson method is implemented as follows: we start by computing within DFT the relaxed atomic and electronic structure of SrVO_3 , extract the Wannier bands for the p and d bands using Wannier90 to build a tight-binding “p-d” model, and finally implement a self-consistent slave-boson calculation on this model. See Figure 5.7 for an overview of this process.

Here, we keep the on-site energies from DFT (i.e., all $B_{im\sigma} = 0$). The reasoning is that, due to the t_{2g} degeneracy and large p-d splitting, added on-site energy terms (B) for the t_{2g} orbitals would be equivalent to changing the p-d splitting and thus renormalize the band width, which in this particular material generates a very similar to changing the U but for different physical reasons. Namely, U creates dynamic electronic renormalization ($Z < 1$) which narrows the d bands, whereas increasing the



FIGURE 5.7: Basic schematic of the software used for the slave-particle calculation on real materials, starting with Quantum Espresso, continuing with Wannier90 and finishing with slave-particle calculations done with our software

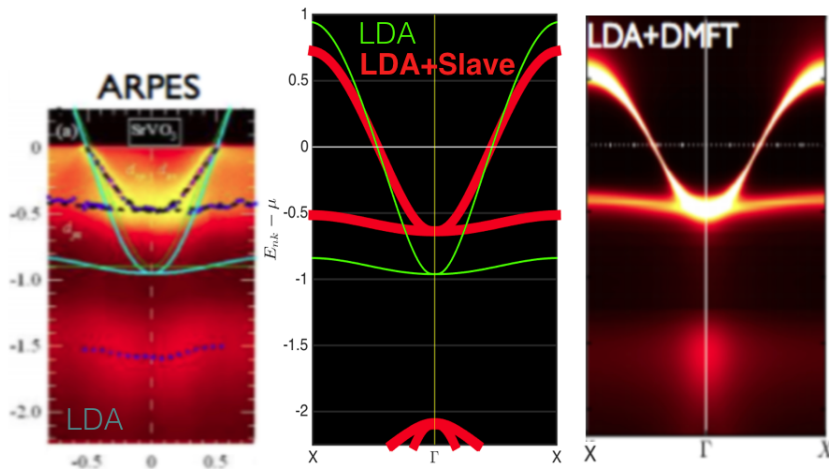


FIGURE 5.8: Spectral functions for SrVO_3 . Left: ARPES [61] and Right: DMFT [14] calculations, Middle: LDA+Slave. Despite a much simpler, faster approach, we reach very good agreement with DMFT and experiment.

p-d splitting will also narrow the d-bands even at $U = 0$ but will keep Z fixed. Hence, the underlying reason for the band narrowing is different. Here, we are inquiring if correlations can lead to the significant band narrowing observed in this system.

The DFT calculations were done using a $7 \times 7 \times 7$ k-point mesh sampling the Brillouin zone, a Gaussian smearing with width 0.05 eV when integrating over the Brillouin zone, a kinetic energy cutoff of 35 Ry for the wave functions and an energy cutoff for the charge and potential of 280 Ry. The Wannierization was done allowing a frozen window 20 eV wide

which included the oxygen 2p and vanadium 3d dominated valence and conduction bands. The slave-particle calculation was done allowing for different slave-modes for each vanadium d orbital, and the Hubbard U was chosen to be $U = 12$ eV. We picked the U value of 12 eV in order to include an amount of correlations comparable to DMFT $U=10$ eV and $J=1$ eV (as we do not use a J in this calculation) as well as to get the effective masses from experiment. Our effective masses $m^*_{t2g}/m_{DFT}=1.95$ and $m^*_{eg}/m_{DFT}=1.4$ are both in good agreement with experiment and available DMFT results [14, 61] of 2.0 and 1.3, while the LDA+slave spinon bands are in good agreement with the spectral functions from experiment and DMFT as shown in Figure 5.8.

5.4 Band narrowing in NAO/NNO

Emboldened by the success of our slave-boson approach for SrVO_3 , we now use it to study band narrowing effects in NAO/NNO. In order to test our hypothesis, we first create a Wannier p-d model from the superlattice calculation using Wannier90, retaining only the Ni 3d and O 2p Wannier orbitals. Furthermore, we perform self-consistent slave-particle calculations on this model, using slave particles only for the Ni e_g states and keeping the on-site energies unchanged from DFT. We begin by manually fixing the effective mass of both e_g orbitals to be $m^*/m_{DFT}=0.33$, assuming the effective mass renormalization is the same as that in bulk LNO to check our theory. We implement this by setting the value of all $\langle \hat{O} \rangle = 0.33$ by hand. In this case we obtain $n(3z^2 - r^2)=0.63$ and $n(x^2 - y^2)=0.59$, leading to $r = 0.9$, matching the experimental value.

U (eV)	$n(3z^2-r^2)$	$n(x^2-y^2)$	r	m^*/m_{DFT}
0	0.523	0.58	1.14	1
5	0.541	0.574	1.08	1.43
10	0.581	0.578	0.99	2.15
20	0.624	0.5852	0.91	2.8883
'manual'	0.63	0.53	0.9	3

TABLE 5.4: Slave-number calculations on the 1×1 NNO/NAO superlattice. Note that around $U = 10$ and $m^*/m_{DFT} = 2.15$, the orbital polarization starts matching the direction from experiment

Table 5.4 shows how the predictions depend on U .

5.5 Conclusions

Throughout this chapter, we have isolated a series of factors that are relevant to orbital polarization and that have not been previously reported in the literature. Given the growth rate of this field of study in the complex oxide community, a better understanding of what actually causes orbital polarization in a material can be used to design novel materials systems. After a brief review of how quantum confinement can narrow the Ni $3z^2 - r^2$ bands in a NNO/NAO superlattice, the main contributions of this work are the study of how an on-site orbital potential difference can appear without any strain effect, purely due to the different ionicity of the two materials used to build the heterostructure. Finally, we've explained how orbital polarization in such a case can be wrongly predicted by density functional theory and DFT+U and corrected by band narrowing which is not possible to describe in DFT calculations (and band theory more generally).

Chapter 6

EELS Spectra in Manganite-Ferroelectric Interfaces

An important characteristic of transition metal oxides are the electronically active d-orbitals on the transition metal cations [62] and their relative energies in both bulk and interfaces [63–68]. A rich variety of physical phases arise from these, including magnetism, ferroelectricity, colossal magnetoresistance and, most famously, high temperature superconductivity.

Manganites are a classical example of a transition metal oxide class in which the filled t_{2g} orbitals are low in energy while the e_g orbitals near the Fermi level ($d_{3z^2-r^2}$, $d_{x^2-y^2}$) play an active role in transport and magnetism [69, 70]. An important area of research in transition metal oxides, including manganites, has been that of orbital engineering. The energetic ordering of the e_g orbitals on the manganites has been shown to be important in the bulk as well as at manganite surfaces and interfaces [71–

77]. One aspect of orbital control involves the lifting of orbital degeneracy (orbital polarization). Jan-Teller-like distortions due to epitaxial strain are a common, albeit weak, tool for creating orbital polarization in manganites[70]. In terms of interfacial orbital control, the interface between the manganite $\text{La}_{0.2}\text{Sr}_{0.8}\text{MnO}_3$ (LSMO) and ferroelectric BaTiO_3 (BTO) offers, in principle, a system showing interfacial orbital polarization [26] that is, in principle, switchable via external electric fields.

A key aspect of understanding the physics of transition metal oxides is being able to relate theoretical predictions from calculations to various spectroscopic measurements. More specifically, new spectral phenomena specific to interfaces can occur that are not understood by superposing various reference bulk spectra (the typical experimental approach) and require direct theoretical modeling.

Electron Energy Loss Spectroscopy (EELS) has been used to understand electronic states at interfaces of transition metal oxides, including manganites [30, 31, 78, 79]. The most common approach is to study the oxygen K-Edge spectra (which correspond to electron excitation from the O $1s$ to unoccupied O $2p$ orbitals). In a purely ionic model and with oxygens being in their O^{2-} state in the oxide, the O-K edge spectrum would be zero as no empty O $2p$ orbitals would be available. In transition metal oxides, however, covalency between the oxygen atoms and the nearby transition metal cations is not negligible. This means that the unoccupied states of the material, while dominated by cation orbitals, have a substantial O $2p$ component which permits O K-edge excitations. Hence these types of spectra provide valuable information about the degree of

metal-oxygen hybridization and O $2p$ hole states. In terms of first principles DFT modeling of EELS spectra, the state of art tools are the so called “Z” and “Z+1” approximations, described below.[30–32]

In this work, we describe the relation between the computed spectra and the measured EELS O-K edge spectra in detail in a spatially resolved manner for the LSMO/BTO interface. We will show how EELS spectra and theoretical calculations can provide us insight into the local electric fields at the interface as well as information about the local core-hole screening.

6.1 Methodology

The experimental methods used for sample fabrication and EELS measurements have been mentioned in another publication [26]. The theoretical calculations have been done within the density-functional-theory (DFT) approach using the Quantum Espresso software [22] using the generalized gradient approximation (GGA) [21] and ultrasoft pseudo potentials as provided by the Quantum Espresso library [22]. We have used a $5 \times 5 \times 1$ k-point mesh for a $c(2 \times 2)$ unit cell in the x-y plane, a kinetic energy cutoff for the wavefunction of 30 Ryd, while for the potential and density we’ve used a cutoff of 350 Ryd. For the electron occupation function, we used a Gaussian smearing width of 5×10^{-3} eV. All the supercells in our simulations are of the form $(\text{Pt})_n / (\text{BTO})_m / (\text{LSMO})_l / \text{vacuum}$ along the (001) direction, where m is often a half integer due to the fact that we start and end the BTO structure with a BaO layer. (Please see

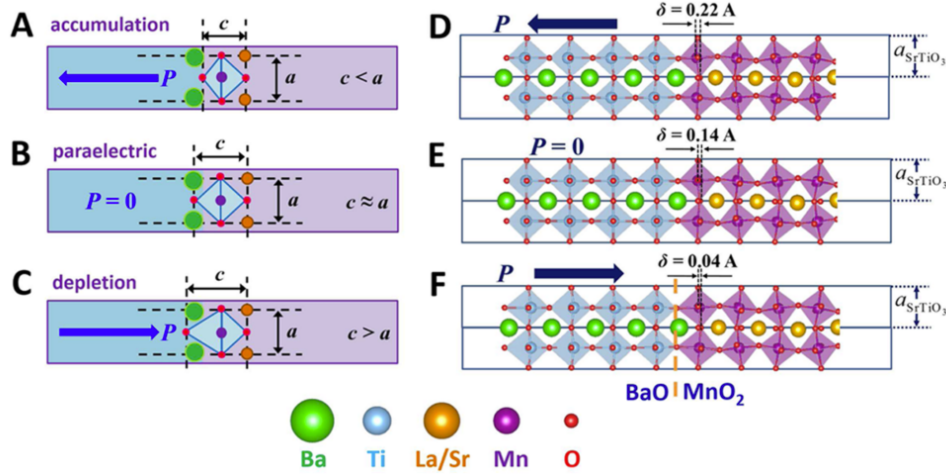


FIGURE 6.1: (A-C) Schematic of the BaTiO₃/LSMO interface where the purple part represents LSMO and light blue represents BTO. The oxygen octahedron changes its ratio with ferroelectric polarization. (D-F) Relaxed atomic structures from first-principles calculations. The structure is strained to an STO substrate (not shown) and uses Platinum as an electron reservoir (not shown). This figure was first published in a previous work[26]

reference [26] for details of the supercell and see Figure 6.1 for some illustrations.)

The periodic (100) and (010) dimensions of the supercell were fixed to the experimental SrTiO₃ size of $a=3.905 \text{ \AA}$, as the experimental system was grown epitaxially on SrTiO₃. The La_{1-x}Sr_x doping was implemented using the virtual crystal approximation (VCA) [24]. We have performed calculations by using a relaxed 1×1 structure in the xy plane, as well as relaxed $c(2 \times 2)$ calculations including octahedral rotations where all but a unit-cell thick region of the BTO were allowed to relax; the fixed atoms in BTO were used to impose a bulk-like polarization in the BTO layers. For the purposes of isolating different electronic factors through numerical experiments, we have also used 1×1 bulk supercells of the form (BTO)_{*m*}/(LSMO)_{*l*} whose structure we did not relax.

Our approach to computing the EELS is standard [30–32]. Fast electrons passing through a material can excite a variety of modes in the material. Electrons with sufficient kinetic energy can excite core electrons into the unoccupied valence manifold. Since core electrons are highly localized in space, we assume that the transition operator for the excitation is a traditional dipole transition operator. Furthermore, we assume that the transition matrix element is essentially independent of energy over the few eV range of interest for the spectra (e.g., O-K edge spectra in metal oxides are near 530 eV of excitation energy while the physically interesting feature of the spectrum appear over a range of about 5-10 eV) [30, 31]. What all these approximations mean is that, within band theory, the measured spectrum at energy should be proportional to the number of unoccupied O $2p$ states at that energy (i.e., the O $2p$ density of states). In what follows, the density of states projected onto atomic orbitals will be denoted as the PDOS (projected density of states).

We have used two methods of calculating EELS, known as the “Z” and “Z+1” approximations [32]. The difference between them regards how the core hole (i.e., the missing electron in the $1s$ shell of the excited oxygen) is treated. In the Z approximation, we assume that the states available for the excited electron are the band states from the ground state calculation: namely, no modification of the density of states should happen above the Fermi level E_F . This approximation is very good if the other electrons can screen the core hole effectively and very rapidly. In the Z+1 approximation, we first self-consistently calculate the electronic structure after we add a core-hole to the system on a chosen O atom. In practice, we add the core hole by either generating a specialized oxygen

pseudopotential with a core hole in its $1s$ state or more traditionally by adding a proton to the nucleus of this special atom; in practice, we find the difference between the two methods is negligible. Hence, the $Z+1$ approximation has the electron excited into electronic states corresponding to a fully and self-consistently screened core hole. The $Z+1$ approach has the merit of including the core hole and its associated screened potential, but it does assume that the core hole screening is essentially instantaneous compared to the process of electron excitation itself.

In order to check that our calculations are reliable and believable when compared to bulk experimental reference spectra, we have computed O-K edge spectra for a variety of dopings x in bulk $\text{La}_{1-x}\text{Sr}_x\text{MnO}_3$ ($x=0,0.2,0.4,0.6,0.8,1.0$). We find that $Z+1$ is consistently a good approximation which delivers high quality spectra from both previous theory [30, 31] as well as from our calculations in Fig 6.3.

6.2 Results

O-K edge spectra can be used to understand the nature of bonding between the O $2p$ states and the neighboring cation d states. At our LSMO/BTO interfaces, there are two polarization states. When the BTO ferroelectric polarization points towards the interface, electrons accumulate in the interfacial LSMO region to screen the ferroelectric surface charge: this is called the “accumulation” state since holes are the dominant carrier type in LSMO. The opposite polarization state accumulates electrons and is the “depletion” state.

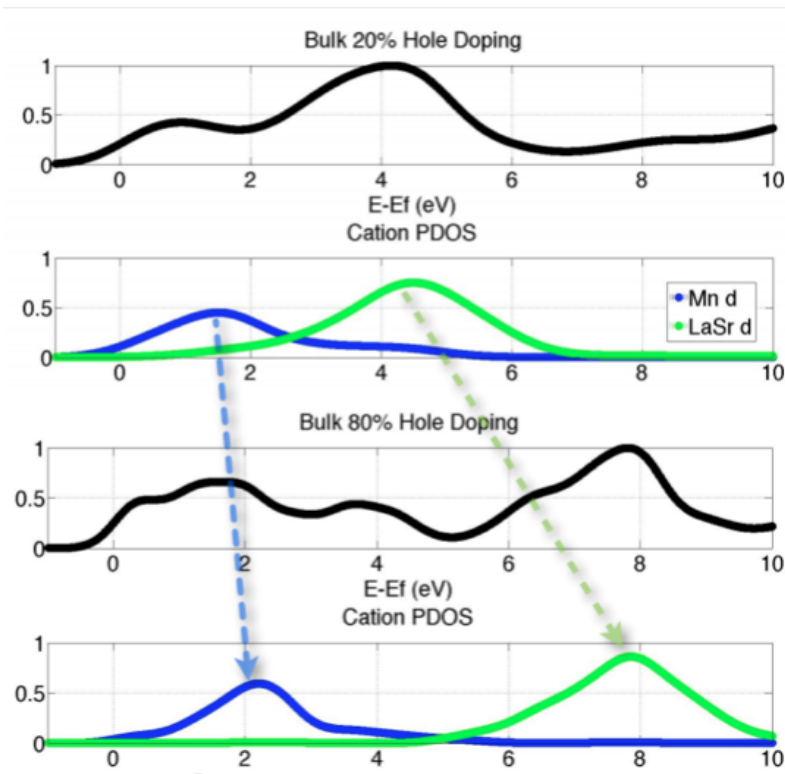


FIGURE 6.2: $Z+1$ calculations for two different doping levels of bulk $\text{La}_{1-x}\text{Sr}_x\text{MnO}_3$. Computed O $2p$ PDOS are in black and cation d PDOS are below them in blue and green. Note the two main effects of the change in doping: hole doping leads to an increased Mn-prepeak, while the change in element from La to Sr increases the relative energy of the La/Sr prepeak as Sr d states are higher in energy than La d states.

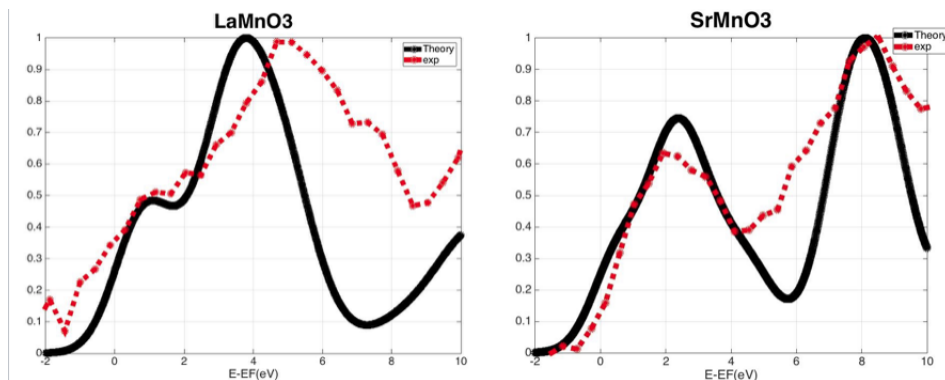


FIGURE 6.3: $Z+1$ calculations for fully relaxed LaMnO_3 and SrMnO_3 versus experimental data. Both show good agreement between theory and experiment.

Briefly, the two main effects caused by the existence and switching of the ferroelectric polarization are:

- The hybridized interfacial Mn $3d$ -O $2p$ states in the LSMO (dominated by Mn $3d$ as they are “conduction band” states) at the Fermi level accommodate almost all of the screening charge, as expected.
- The energy levels of the different cation dominated states above E_F shift in energy in different ways. The Mn $3d$ states shift in energy in order to accommodate the screening carriers (holes or electrons). However, the energy of the La/Sr d states and the Ba d states shifts according to the electrostatic potential profile in the interfacial region that is created by the ferroelectric field effect (i.e., ferroelectric surface charge and associated screening carriers).

This leads to the following effects on the computed EEL spectra:

- The low-energy part of the O-K edge spectrum, the “pre-peak”, is dominated by Mn $3d$ -dominated states right above E_F . As these are filled by electrons or holes, we see the associated spectral weight decrease or increase, respectively. However, the energy position of this prepeak does not shift much since the Mn $3d$ -dominated states are essentially pinned to the Fermi level.
- The higher energy spectral weight is the “main peak” and is dominated by La/Sr d states (hybridized with O $2p$). These states are not fixed to be near the Fermi level and are thus free to “slide” along the energy axis depending on the local electrostatic potential. They shift in energy and also separate in energy by different amounts in the two polarization states.

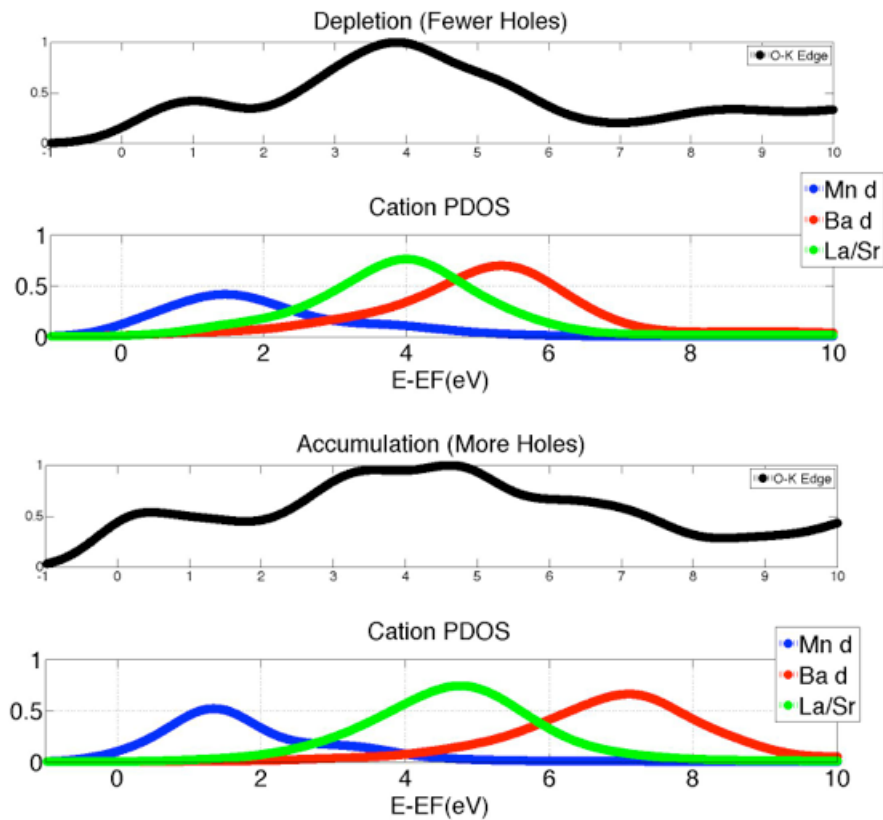


FIGURE 6.4: $Z+1$ calculations from a 1×1 supercell interface for LSMO/BTO. What are plotted are projected densities of states (PDOS) onto O $2p$ (the “O-K edge” data in black) and the various cation d orbitals at the interface. The normalization of the plots is arbitrary. Top two plots are for depletion and bottom two plots are for accumulation. Notice the upward shift in energy of the Ba d states and the La/Sr d states in the accumulation state compared to the depletion state as well as the increase in the Mn $3d$ density of states above E_F for accumulation.

Computed spectra illustrating these key points are shown in Figure 6.4. The main spectral features that we wish to analyze further are the relative shifts in energy of the different cation d projections. Please note that the shape of the main peak is quite different in the two different states primarily because the La/Sr d and Ba d states have different relative energy shifts in the two polarization states. This means that if one uses the pre-peak to main peak spectral ratio as a way to track the local electronic properties (a standard experimental approach), one must be cautious in interpreting the data since the interfacial ratio is modified by effects not present in bulk materials (multiple cation peaks moving by differing amounts).

We have done our analysis of spectral shifts in two ways. First, we can examine plots like Figure 6.4 and find the shift of the peaks of the cation PDOS. Second, we can compute the DFT self-consistent electrostatic potential and average it on each plane of atoms and compute the shift of averaged potentials. Figure 6.5 shows a comparison between the two methods showing that they agree quite closely.

These shifts are understood most simply via a simple electrostatic model. Figure 6.6 shows a schematic of the expected charge distributions for the accumulation configuration where the BTO polarization points away from the interface drawing holes into the interfacial LSMO. The fact that the interfacial LSMO is hole doped means its local potential must higher than deeper in the bulk of LSMO: pictorially, the presence of the negative BTO surface charge has “repelled away” electrons from the interface. The opposite situations hold for accumulation.

Finally, we compare our computed DFT spectra to measured EELS

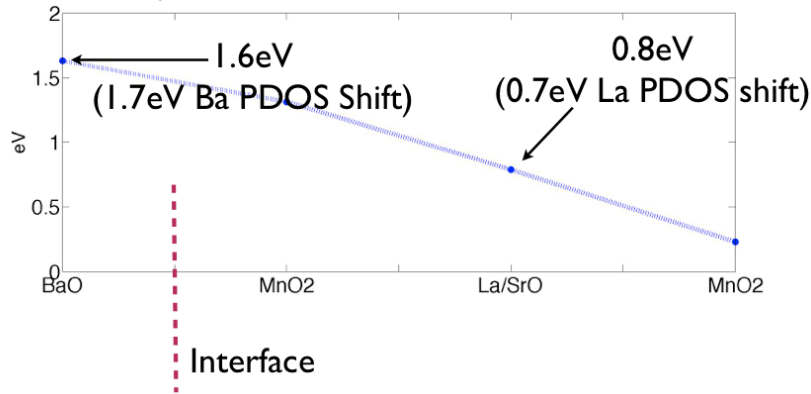


FIGURE 6.5: Energy shifts of various cation states across the LSMO/BSTO interface computed in two different ways. The blue dots show shifts of the layer-averaged electrostatic potential going from accumulation to depletion. They are compared to shifts of the cation PDOS peaks for the BaO and La/SrO layers as well showing close agreement. As expected, deep inside the metallic LSMO the shifts go to zero.

O-K edge spectra for the O atom in the MnO_2 layer at the interface. We compare the two experimental spectra (for the two polarization states) to both Z and Z+1 theoretical models in Figure 6.7. The four way comparison shows that the accumulation case is well described by the Z+1 approximation. Prior work in the bulk manganites [30, 31] for a large range of dopings as well as our bulk simulations would naturally make us expect Z+1 to work well. In addition, the computed spectra for the second MnO_2 layer in the LSMO (Figure 6.8) as well as the nearest TiO_2 layer in the BTO agree between theory and experiment for both polarization states when Z+1 is used, again as expected.

What is surprising is that the depletion spectrum is clearly much in closer agreement with the Z approximation and the Z+1 spectrum is poor by comparison. This is hard to understand given all the successes of Z+1 listed above.

(Hole) Accumulation State

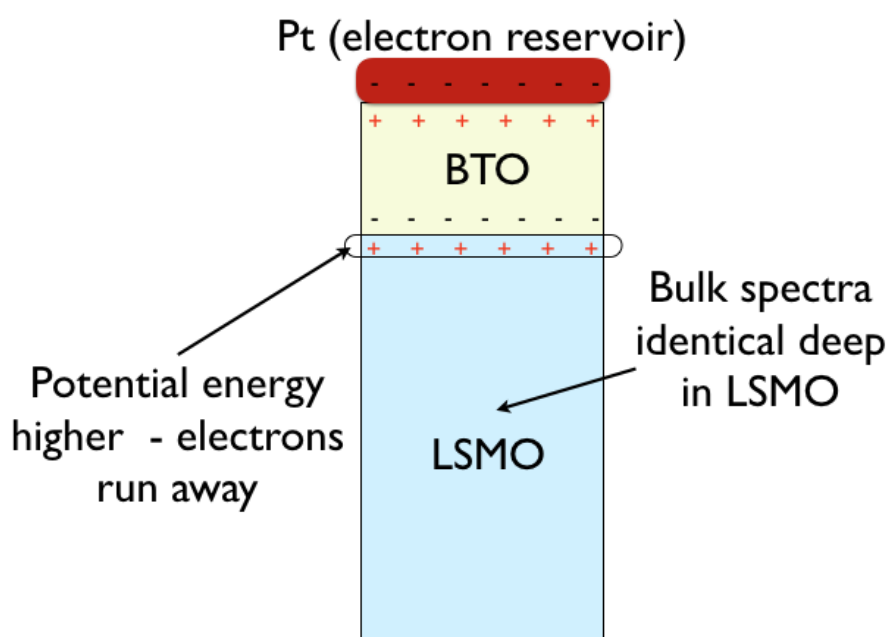


FIGURE 6.6: Simple electrostatic model of the LSMO/BTO system for the Accumulation State. Due to the ferroelectric field effect, electrons “run away” from the interface between the LSMO and the BTO, and the remaining holes act as the screening charge. The electrode on the other side of the BTO is the reservoir accepting the electrons. Hence, the energy shifts in the Ba d and La/Sr d PDOS and local potential correspond to this effect. The depletion state corresponds to the opposite of this effect.

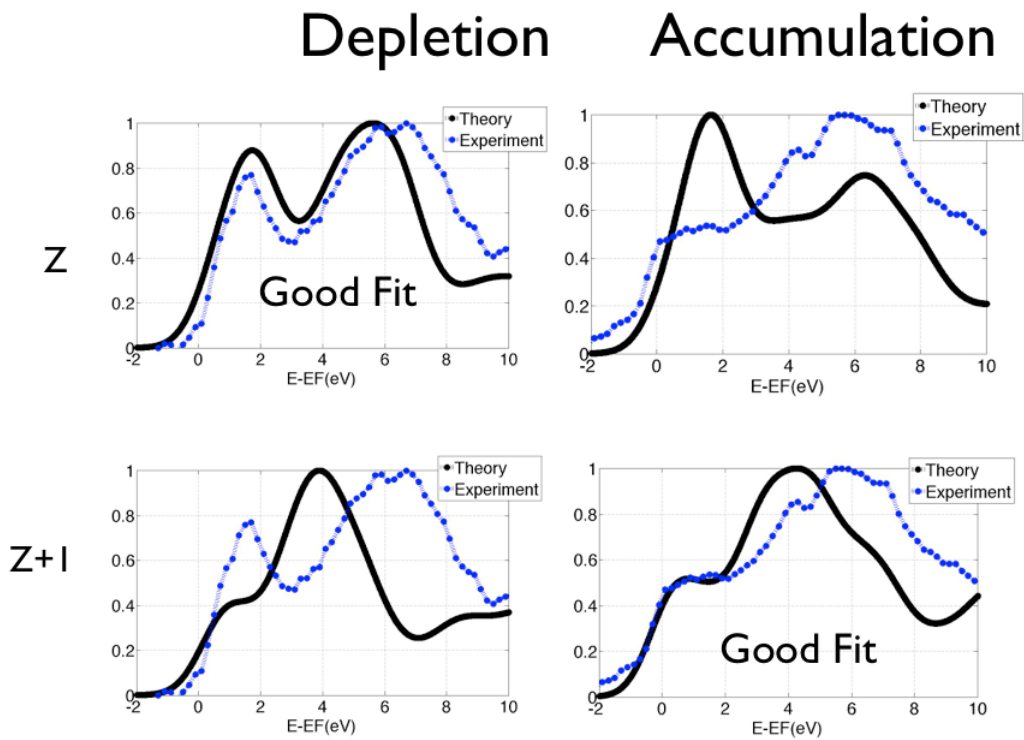


FIGURE 6.7: Comparison of DFT-computed and measured O-K edge EELS spectra for the O atoms in the interfacial MnO_2 layer at the LSMO/BTO interface. The columns label the interfacial state and the rows show a comparison between the Z and Z+1 theoretical models.

Physically, one expects the Z approximation to be more relevant when the core hole is well screened by a robust metal with a short screening length. If this were the case in the theory, then the Z and $Z+1$ would have produced very similar results since the $Z+1$ includes the screening. Given the qualitative difference, we must conclude that if in fact this line of reasoning is correct, then the screening as computed by DFT for this interface is incorrect in some basic way but only for depletion and only for this interface (as opposed to the bulk at the same doping level). While possible, this seems unusual.

Another possibility is that since the depletion state has more electrons at the interface, the lifetime of the core hole is reduced significantly due to enhanced Auger recombination processes making for a better match to the no-core-hole Z approach. Again, while possible, it is hard to understand why the bulk at the same doping levels would not see the same overall reduction.

A final possibility is experimental "error": perhaps the theoretical simulation is not being performed on the same system as the experiment. Since the theoretical interface is ideal and atomically sharp, one could guess that the depletion state suffers from an interface that is not quite sharp. For example, intermixing of cations across interface would make theory and experiment differ. We note that the experimental prepeak in depletion is tall relative to the main peak in depletion (and oppositely in accumulation) which is contrary to what would expect based on the doping level at the interface. By contrast, both Z and $Z+1$ theoretical spectra show higher prepeaks for the hole doped (accumulation) interface, as expected.

In an effort to resolve this discrepancy, we have first carefully checked a number of potential theoretical issues and verified that they do not change our theoretical conclusions.

First, this interface shows a change of magnetic structure of the Mn spin states when going from accumulation to depletion [25, 26]. We have computed O-K edge spectra with and without including the magnetic structure change and have not seen any significant changes in the computed spectra.

Second, we have checked for finite size effects. We have computed Z+1 spectra in both 1×1 and $c(2\times 2)$ unit cells. The computed PDOS do show changes, but the energy shifts of the PDOS and overall patterns do not change nor do these spectra agree any better with the experiment.

Third, in going from 1×1 to $c(2\times 2)$ unit cells, we permit for oxygen octahedral rotations to take place. Again, some changes are observed in the computed PDOS but no major qualitative changes are seen.

Fourth, we have tested for possible direction dependence of the O-K edge transitions. Namely, perhaps only dipole transitions perpendicular to the narrow electron beam are allowed to occur. This is easily modeled by only computing the oxygen PDOS for selected O $2p$ orbitals. However, the computed spectra do not show any real changes that help resolve the above disagreement.

Since we have exhausted a large variety of possible electronic explanations for the discrepancy, we turn to structural differences between experiment and theory. Perhaps there are 'steps' at the interface reflecting steps on the SrTiO₃ surface on which the interfacial system is grown epitaxially (steps in the direction along the electron beam). This would lead

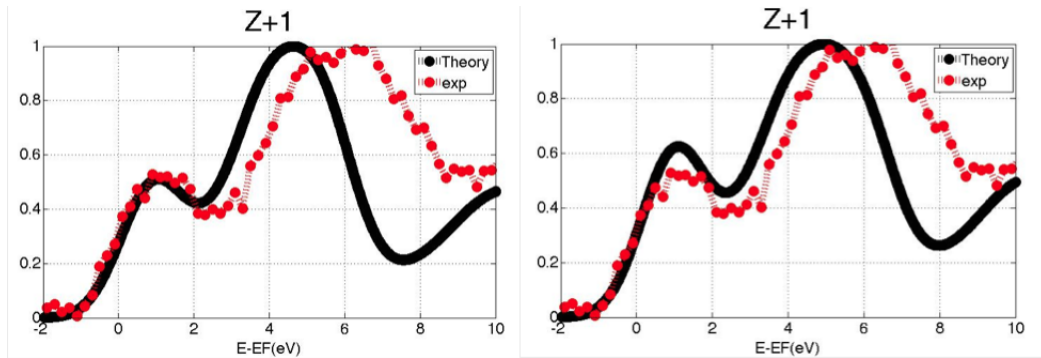


FIGURE 6.8: Comparison of DFT-computed and measured O-K edge EELS spectra for O atoms in the second MnO_2 layer of LSMO. The spectra are already bulk-like in this layer and show good agreement between theory and experiment. Shown here are depletion (left) and accumulation (right)

to a mixture of the interfacial spectra of $\text{La}_{1-x}\text{Sr}_x\text{MnO}_3$ and BaTiO_3 in the experimental results as the electron beam would sample both layers as it traverses the sample. See Figure 6.10 for an illustration.

Indeed, after Energy Dispersive X-ray Spectroscopy (EDS) was performed on the sample by our collaborators at University of Illinois at Chicago (Figure 6.11), we can infer that steps in the substrate do exist are a potentially a likely explanation for layer mixing. In order to further explore this possible avenue, we have asked our experimental colleagues to further explore this sample.

Separately, as illustrated in Figure 6.12, one can get a good match to the measured spectrum for depletion by empirically mixing in 30% of the computed spectrum for the TiO_2 layer with 70% of the spectrum from the interfacial MnO_2 layer. Hence, if there are steps such that the electron beam samples both MnO_2 and TiO_2 layers as it crosses the sample, it is very possible to see unexpected spectra.

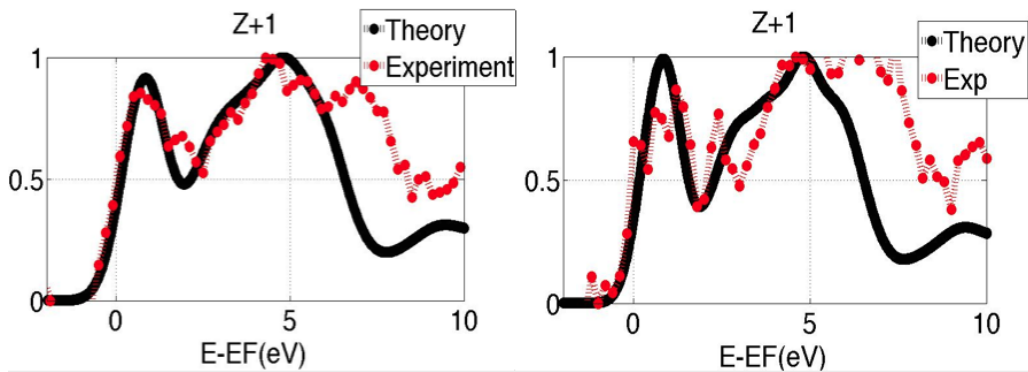


FIGURE 6.9: Comparison of DFT-computed and measured O-K edge EELS spectra for the O atoms in the second TiO_2 layer in BTO, depletion (left) and accumulation (right). The spectra are already bulk-like and match experiment well.

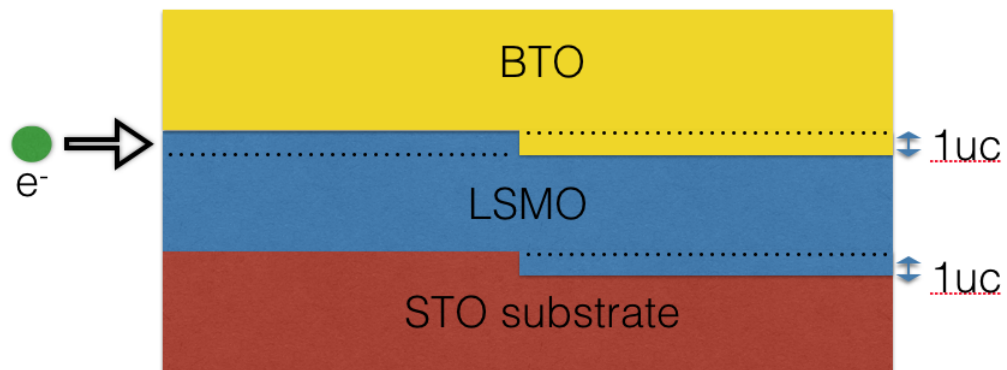


FIGURE 6.10: Steps in the STO substrate can lead to defects in the interface. An incoming electron samples both the TiO_2 layer and the MnO_2 layer, requiring an interpolation of the spectra of the two layers to appropriately describe the EELS spectra.

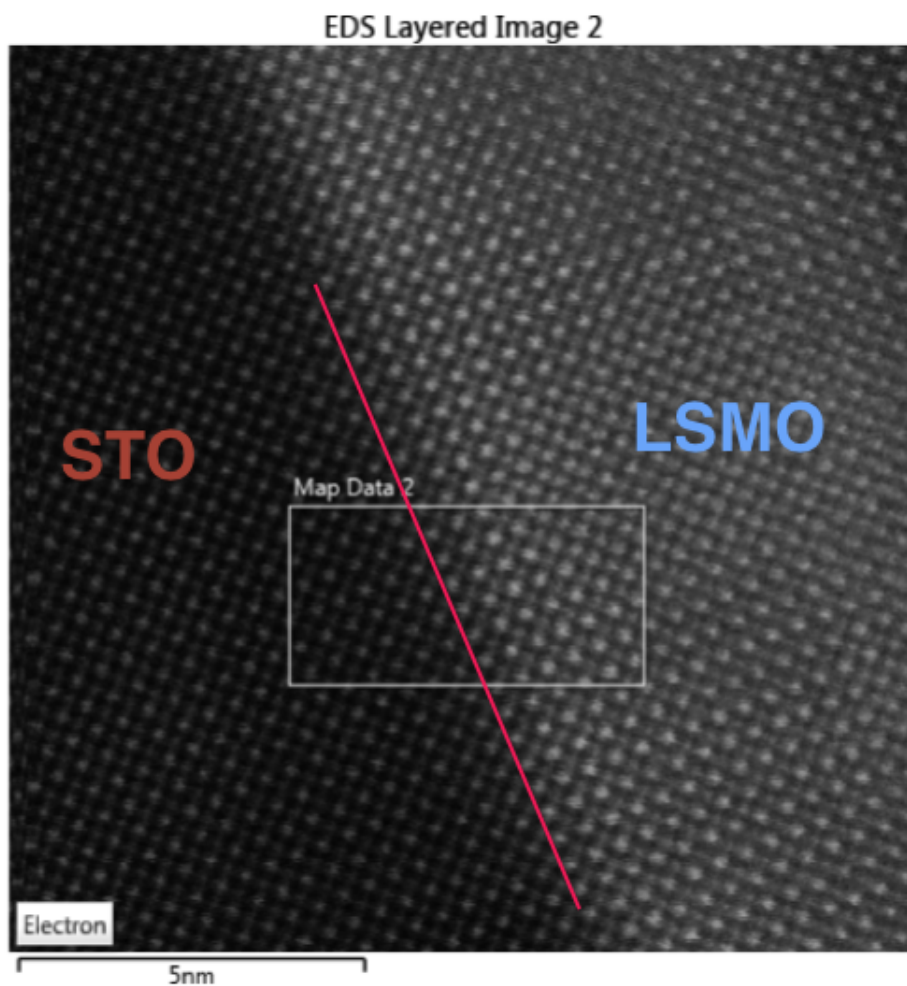


FIGURE 6.11: EDS image of the sample from our experimental collaborators at University of Illinois at Chicago. Note that as one follows the red line upwards, the atoms to the right are shown as darker. This signals that there is an increased amount of LSMO. A beam passing through the LSMO/BTO layer would see intermixing at that interface, as described in Figure 6.10.

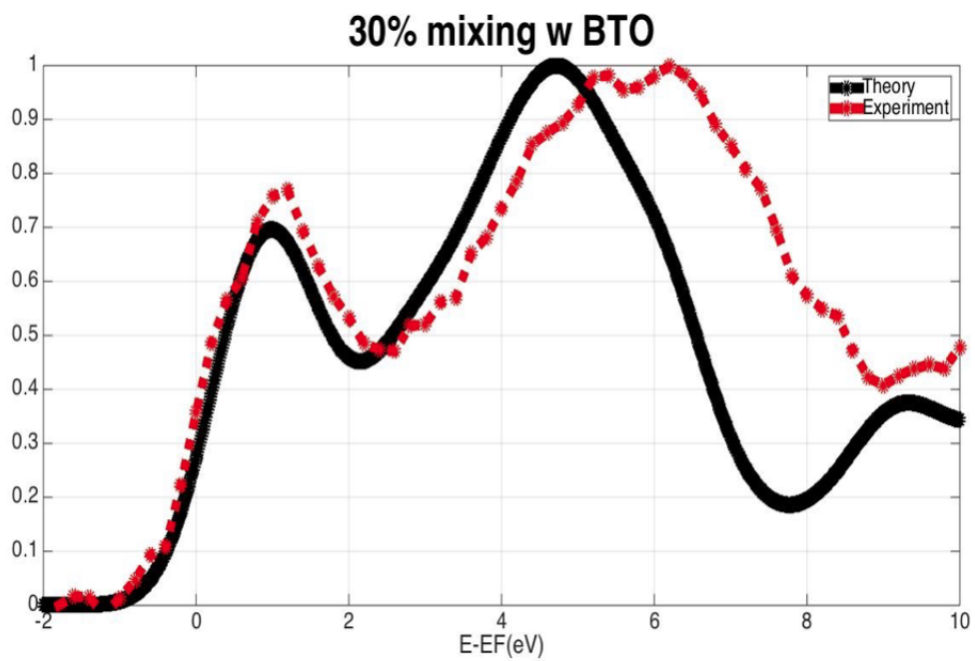


FIGURE 6.12: Experimental O-K edge compared to theoretical O-K edge simulated by linear superposition of 70% of the interfacial LSMO O-K edge obtained from the MnO_2 layer and 30 % of BTO TiO_2 layer for the depletion interfacial layer.

6.3 Conclusions

Our present work highlights a number of important factors when attempting to understand interfacial O-K edge EELS spectra at oxide interfaces. The first is that the energies of different cation orbitals across the interface can shift in different and independent ways depending on the electrostatic potential profile across the interface. In our example, the Ba d states on the BTO side move by a different amount than the La/Sr d states on the other side, and this makes the structure and energetic spread of the “main peak” of the O-K edge EELS behave in a non-straightforward manner.

Second, the energetic shifts of the various cation d states can be understood relatively easily from electrostatic considerations of how the potential profile changes across the interface in response to the polarization state of the ferroelectric.

Third, interfacial roughness can change the measured spectra due to the sampling of multiple interfacial environments as the electron beam goes through the sample. In fact, one can estimate the amount of layer intermixing by empirically fitting the theoretical results.

Chapter 7

Dimer Mott Insulator State in a Cobaltate-Titanate Heterostructure

In this chapter we study a cobaltate/itanate interface within the limits of DFT and DFT+U. As with previous systems, the main goal of looking at such a system is to devise new materials at the interface, as well as to 'orbitally engineer' the materials by creating orbitally-polarized materials. Surprisingly, in this case, DFT+U was able to provide an apparently accurate band gap and orbital polarization number r at the same time. This seems to be related to the fact that an interesting type of insulator in which nearby cobalt atoms form molecular-like bonds is formed. Further, this material shows a dramatic interaction between the amount of charge transfer (as dictated by the Hubbard U on titanium) and the structural distortions at the interface.

7.1 Methodology

The theoretical calculations have been done within the DFT+U approach using the Quantum Espresso software, the local density approximation (LDA), and ultrasoft pseudo-potentials. The supercells are infinite superlattices with formula $(\text{LTO})_2/(\text{LCO})_2$ along the (001) direction. We have done calculations without (1×1 in plane unit cell) and with ($c2(2 \times 2)$ in plane unit cell) octahedral rotations. All calculations reported here are performed for the non-magnetic configuration. While we've sampled a variety of strains and so did experiment (LSAT and STO substrates), our results do not seem strongly strain-dependent and for the rest of this chapter we will refer to calculations that impose 0% strain on the LCO using the theoretical lattice constant of LCO of $a_{\text{LCO}} = 3.65 \text{ \AA}$; this also allows us to isolate the effects of the superlattice as opposed to those of strain. Our fully-relaxed superlattices are shown in Figure 7.1 with octahedral distortions allowed ($c(2 \times 2)$ structure in the xy plane) and not allowed (1×1 structure in the xy plane). We used a $5 \times 5 \times 3$ k-mesh, a kinetic energy cutoff for the wavefunction is 35 Ry and for the density 280 Ry, and a Gaussian smearing of 0.01 eV

7.2 Results

In order to appropriately simulate the $(\text{LaCoO}_3)_2/(\text{LaTiO}_3)_2$ superlattice, we use DFT+U using a Hubbard U on the Co and the Ti $3d$ orbitals. Using a U of 4 eV on Co for bulk LaCoO_3 (LCO), we find an insulating electron configuration of $t_{2g}^6 e_g^0$ for the Co with a band gap matching that

of experiment at 0.7 eV [80]. Using a U of 8 eV on Ti in the superlattice leads to a Ti^{4+} valence with a $t_{2g}^0 e_g^0$ configuration. The U value for Co has been calibrated to reproduce bulk LCO properties since we do not know the electron configuration in the superlattice ahead of time (or from experiment). The relevant physical property we are trying to model by adding a U on Ti is the degree of electron transfer across the interface from Ti to Co. A U of 8 eV provides essentially full electron transfer (in agreement with experiment) as found previously in similar systems containing electron transfer from Ti when using the LDA+U approach [81]. This particular choice of U values for the full structural relaxation turns out to capture many of the experimental physical observations, matching both the experimentally measured band gap of 0.5 eV (from transport experiments done by Ankit Disa, however under the assumption that the material is a semiconductor) and the orbital polarization value of the Co e_g

$$r = \frac{2 - n_{3z^2-r^2}}{2 - n_{x^2-y^2}}$$

with $r_{DFT+U}=0.6$ and $r_{exp} = 0.6$ (experimental number obtained by Mark P.M. Dean at Brookhaven National Labs via XAS).

The interface between LCO and LTO is a charge-transfer interface due to the difference in electronegativity between Ti and Co. In bulk LTO, Ti has the 3+ valence with configuration $(t_{2g})^1(e_g)^0$, and Co in bulk LCO has the 3+ valence with configuration $(t_{2g})^6(e_g)^0$. At the interface, the electron leaves Ti and migrates to Co. Figure 7.2 shows the electron transfer process across the interface together with projected densities of states (PDOS) for the Ti and Co atoms at the interface. The PDOS show a fully ionized Ti and an Co accepting electrons into its e_g states.

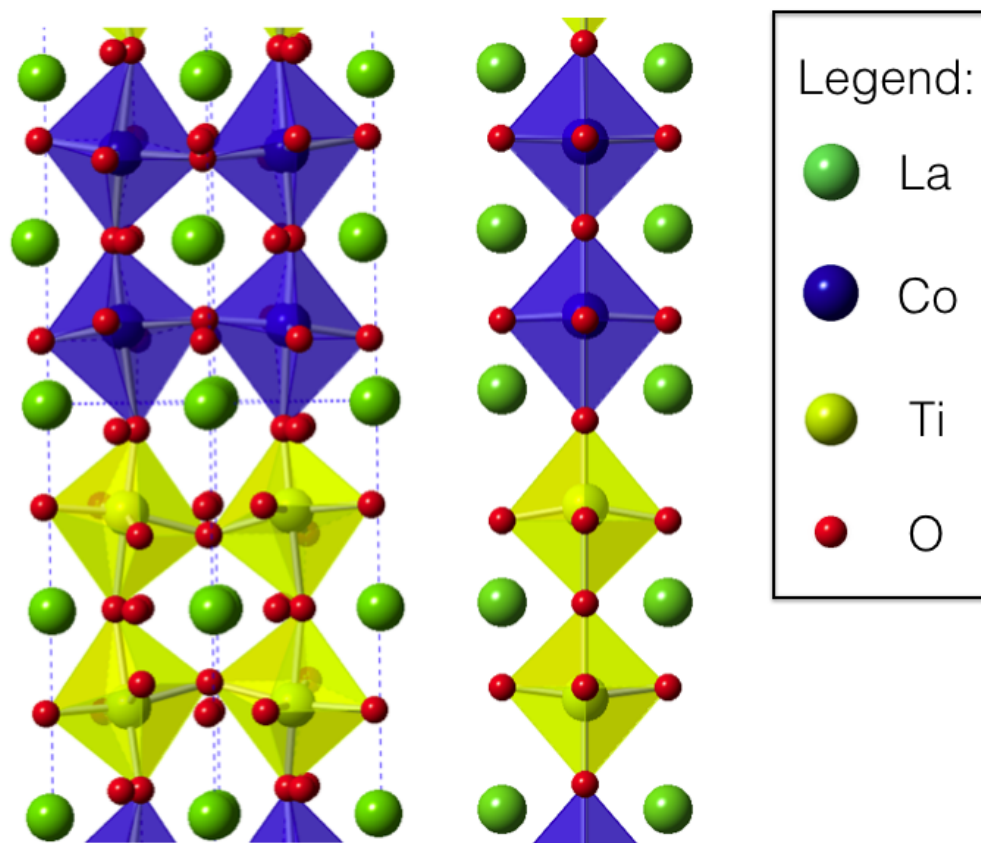
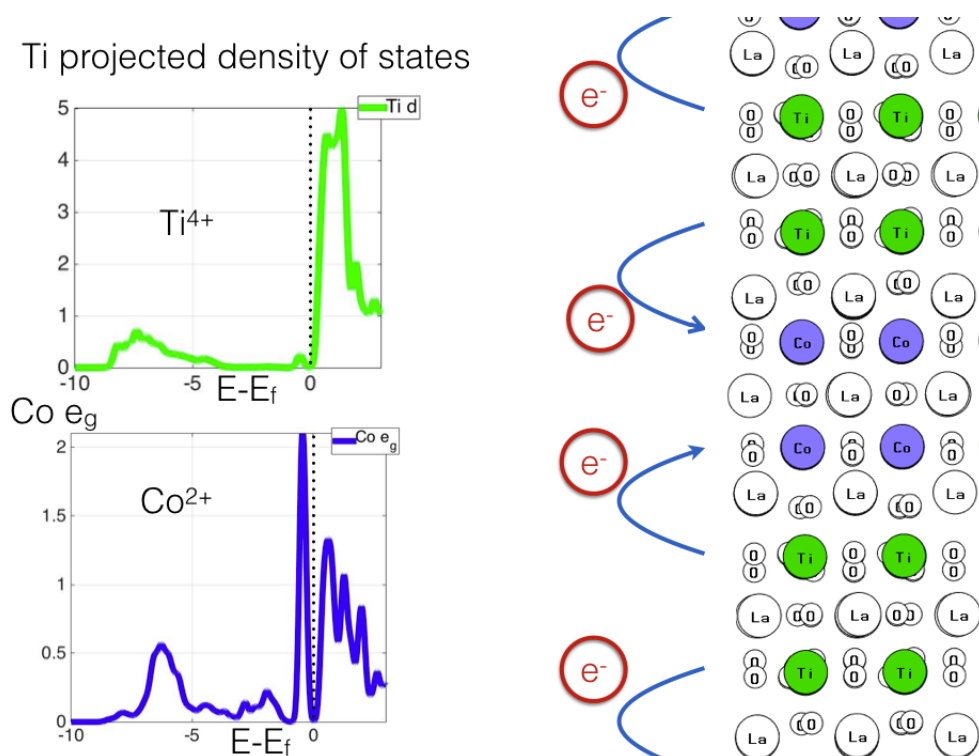


FIGURE 7.1: $(\text{LCO})_2/(\text{LTO})_2$, fully relaxed with a $c(2 \times 2)$ in-plane unit cell (left) and 1×1 (right). Periodic boundary conditions are imposed in theoretical calculation along the superlattice direction, whereas experiment uses 20 repetitions of the unit cell.

The experimentally measured valence of the Ti atom is 4+ (from XPS spectral matching to bulk references such as LTO and SrTiO₃ done by Ankit Disa), so clearly the electron has left the Ti in the experiment. XAS measurements (done by Mark P.M. Dean at Brookhaven National Labs) of the Co reveal a Co valence close to 3.5+ when comparing to reference bulk spectra which is confusing based on our theoretical findings. We note that, as we will show below, that the Co in the superlattice has a very unusual 3*d* electronic configuration which is not very close to any bulk compound that we are aware of.

As is visible in the computed structure shown in Figure 7.1 and as highlighted schematically in Figure 7.3, the interfacial oxygens are 'pulled' towards the Ti atoms and away from the Co atoms. We can modify the degree of charge transfer between Ti and Co by changing the value of U on the Ti atom in order to establish that charge-transfer is, indeed, the cause of the oxygen being 'pulled' towards the Co. As Table 7.1 shows, changing the U on Ti (but not on Co), leads to increased electron transfer, as well as to an increased distortion in the La-O plane.

We now turn to the electronic structure of the interface system. As stated above, the DFT+ U calculation yields a nonmagnetic insulator with an energy gap of 0.5 eV ($U=8$ eV on Ti and 4 eV on Co). This is somewhat surprising since the singly electron doped Co 2+ ion with configuration $(t_{2g})^6(e_g)^1$ is an open shell ion so we would expect a metallic non-magnetic state while an insulating state would tend to require magnetic ordering. To analyze this situation further, we first examine the Co 3*d* PDOS projected onto the separate e_g Co orbitals. As Figure 7.4 shows,



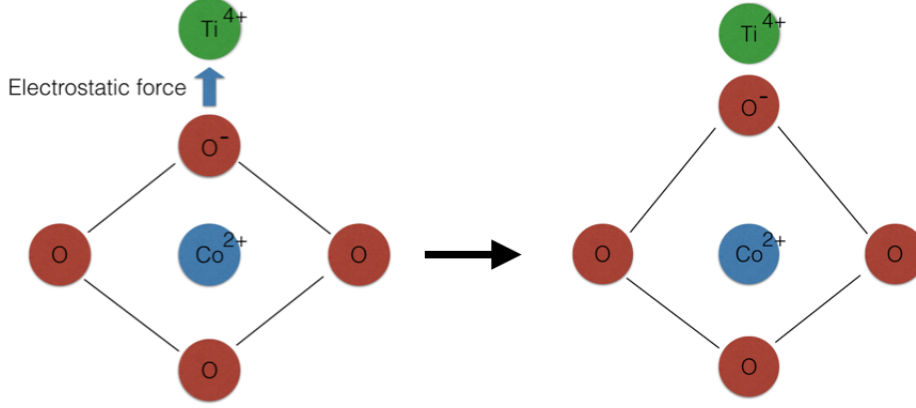


FIGURE 7.3: Left: schematic representation of the Co octahedron at the LCO/LTO interface. The O atom at the top is 'pulled' towards the Ti atom with a 4+ valence instead of the 2+ Co. Right: the resulting distorted structure.

U (Ti)	U (Co)	Energy gap (eV)	$z_O - z_{La}$ (Å)	$n_d(\text{Co})$	$n_d(\text{Ti})$
2	4	0.0327	0.44	7.940	3.146
4	4	0.0582	0.50	7.956	3.040
6	4	0.184	0.56	7.971	2.918
8	4	0.541	0.58	7.973	2.791
8	2	0.270	0.57	7.973	2.789
8	4	0.541	0.58	7.973	2.791
8	6	0.648	0.65	7.968	2.795

TABLE 7.1: Band gap, displacement along the z direction between O and La in the interfacial LaO layer between Ti and CO, and Löwdin electron count of the d orbitals on Co and Ti as a function of the U on Co and Ti. Increasing the U on Ti (but not on Co) significantly affects both charge transfer and interfacial distortions. Calculations done allowing full a full $c(2 \times 2)$ unit cell in the x-y plane, allowing for full octahedral distortions

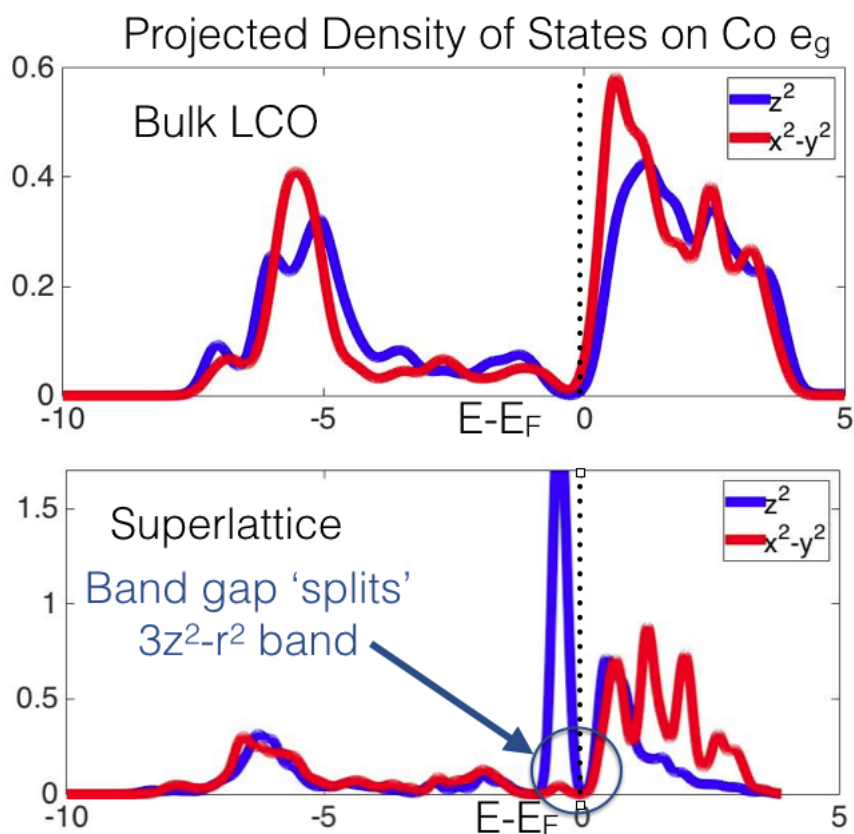


FIGURE 7.4: Top: projected density of states of Co e_g orbitals in bulk LCO. Bottom: projected density of states for Co e_g orbitals in the LCO/LTO superlattice. Both valence bands are empty in the bulk, however after charge transfer that is mainly isolated to the $3z^2 - r^2$ (denoted as z^2 in the legend) orbital in the superlattice, the e_g states show large orbital polarization and a narrow band gets filled right below the Fermi level.

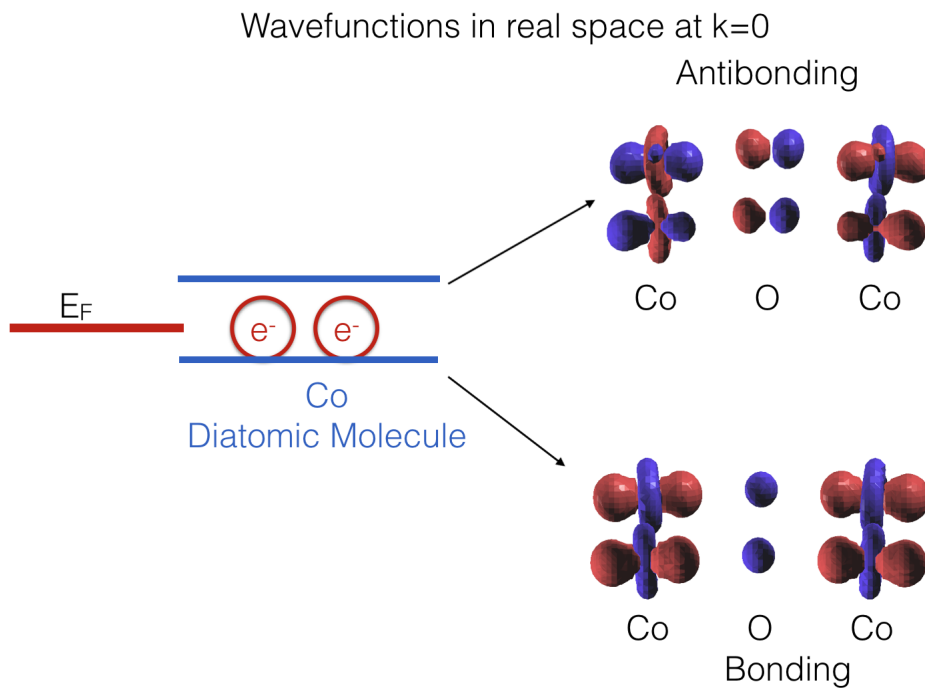


FIGURE 7.5: Right: plots of the unoccupied state right above the Fermi level (top) and the occupied state right below the Fermi level (bottom) at $k = 0$. What is shown are isosurfaces $|\Psi_{k=0}(r)|^2 \times \text{sign}(\Psi_{k=0}(r))$. The in-phase and out-of-phase nature is easily visible as is the dominant $3z^2 - r^2$ character on each Co site. We identify this pair as a bonding and anti bonding pair (left) of a simple diatomic molecular system.

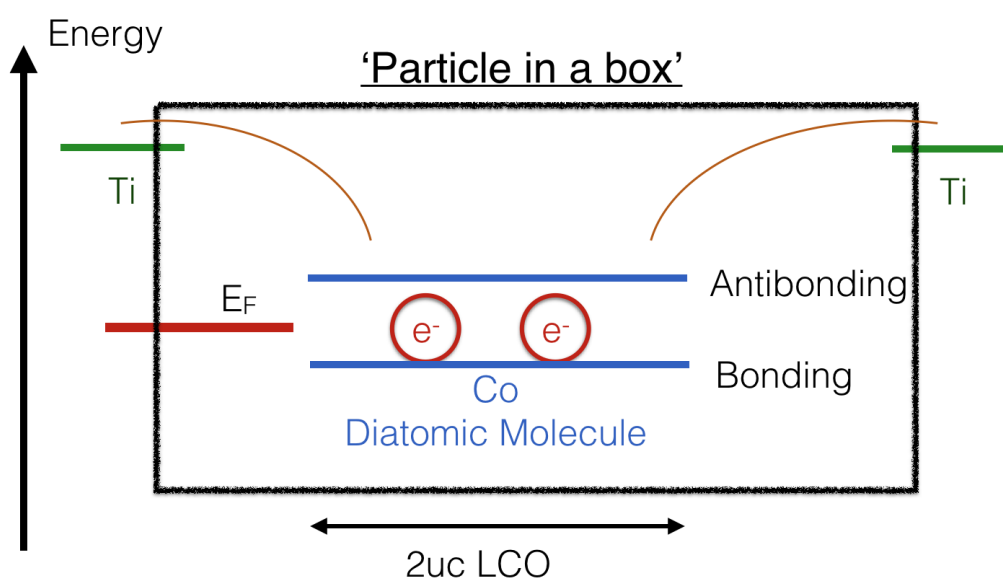


FIGURE 7.6: “Particle in a box” picture: understanding of the bonding-anti-bonding pair in the interfacial LCO bilayer. Since the transferred electron on each Co is confined to the bilayer system of Co (due to insulating band offset with the LTO), we get confined electronic states. The two nearby Co $3z^2 - r^2$ pair and form bonding and antibonding states, essentially forming a diatomic molecular system.

most of the electron transfer to the Co atom occurs into the $3z^2 - r^2$ orbital, leading to a very large orbital polarization ($r=0.63$). Interestingly, the energy gap occurs in the $3z^2 - r^2$ band itself. The PDOS shows that two electrons are filling a very narrow band right below the Fermi level primarily of $3z^2 - r^2$ character.

Next, we plot the band eigenstates at the Γ point ($k = 0$) that are mostly $3z^2 - r^2$ in character, right below and right above the Fermi level. These are shown in Figure 7.5. The phases and the overall structure are consonant with a simple physical picture: the two $3z^2 - r^2$ orbitals on the two Co combine in phase and out of phase to create bonding and antibonding states. The narrow bonding band is filled with two electrons. We end up with what is essentially a molecular insulator. This state is called a 'Dimer Mott State' in the literature [82], although a molecular insulator would probably be an appropriate name as well. Figure 7.6 shows a simple picture of how the confinement provided by the neighboring ionized (and insulating) LTO layers spatially isolates the two Co layers and permits formation of the "diatomic molecular" state.

7.3 Conclusions

Within these calculations, we have found electron transfer at the interface from Ti to Co and proved that it has a strong effect on the structure of the material (verified by modifying the amount of charge transfer via a change in U). The electron transfer and structural distortion leads to a strong orbital polarization and, indirectly, to a 'pairing up' of nearby Cobalt atoms to form a quantum state that, due to the localization of the

electrons, behaves similarly to a Mott insulator with an upper and lower Hubbard band (or, more simply, a two-atom molecule).

Chapter 8

Outlook

In this thesis, we've improved the formalism and the computational scheme for a class of slave-particle methods for use in the study of large complex oxides, as well as shown its potential in sample cases in both model Hamiltonians and in computations based on large-scale electronic structure calculations. We've developed an algorithm that greatly improves the numerical stability of this class of method while allowing for spontaneous symmetry breaking. We've shown the usefulness of our method in the context of understanding band narrowing in a bulk material, as well as helped elucidate new mechanisms leading to orbital polarization in a heterostructure where standard crystal field theory and Density Functional Theory failed. This result in itself gives new guidelines in the search for orbitally-polarized materials through heterostructure growth. Where possible, we've used 'classic' electronic structure theory (DFT, DFT+U) to understand materials grown by our experimental colleagues, revealing both the possibility of a new class of insulating heterostructure in the cobaltates as well as insights into interfacial phenomena at a manganite-ferroelectric interface.

While the class of slave-boson theory we've expanded is not as comprehensive as more established methods such as Dynamical Mean Field Theory, it can however make predictions that pure band theory methods such as DFT and DFT+U cannot. Further, it can be used in calculations to make simple predictions that at the moment would be computationally prohibitive within DMFT, while in cases where DMFT can be used, slave-particle methods give an avenue to do a quick check on the effect of correlations on spectral properties before deploying more expensive methods.

Theoretical issues remain, however, which are general to this class of method: throughout our calculations we did account for the double inclusion of electron-electron interactions in both DFT and the slave-particle method model glued on top, usually known as 'double counting'. In order to appropriately model materials such as charge-transfer insulators, the choice of double counting has been of outmost importance for both electronic and atomic structure predictions [83, 84]. Without a way to appropriately include the double counting terms, this type of method remains a post-processing method without the ability to calculate atomic structures. Further, as with all 'Hubbardism', this type of calculation does not have predictive power *a priori*, rather it depends on an empirically fitted parameter U and sometimes J and, in some cases, an empirically fitted double counting that relies on a different parameter U' [83, 84] as well. An appropriate way to self-consistently determine the parameter U from *ab-initio* remains an important question in this class of models. What our method can do, however, is give guidelines as to what the effect of correlations can be.

The study of correlated complex oxides remains a rich field, and as our study in previous chapters has shown, there is much room for discovery, whether it's in the discovery of new phases or in the explanation of ubiquitous phenomena such as orbital polarization or in the understanding of spectroscopy. And, within this large space, there is room for theory to guide the discovery process as well as explain what is actually being discovered.

Bibliography

- ¹P. Zubko, S. Gariglio, M. Gabay, P. Ghosez, and J.-M. Triscone, “Interface Physics in Complex Oxide Heterostructures”, [Annual Review of Condensed Matter Physics](#) **2**, 141–165 (2011).
- ²W. Kohn, and L. J. Sham, “Self-consistent equations including exchange and correlation effects”, *Physical Review* **140** (1965).
- ³P. Hohenberg, and W. Kohn, “Inhomogeneous electron gas”, [Physical Review B](#) **136**, 864–871 (1964).
- ⁴P. Anderson, and E. Blount, “Symmetry considerations on martensitic transformations: “Ferroelectric” metals?”, [Physical Review Letters](#) **14**, 217–219 (1965).
- ⁵S. Barnes, “New method for the Anderson model : 11 . The $U = 0$ limit”, *Journal of Physics F* **7**, 12 (1977).
- ⁶J. Hubbard, “Electron Correlations in Narrow Energy Bands”, [Proceedings of the Royal Society A](#) **276** (1963) [10.1098/rspa.1983.0054](#).
- ⁷G. Kotliar, and A. E. Ruckenstein, “New functional integral approach to strongly correlated fermi systems: The gutzwiller approximation as a saddle point”, [Physical Review Letters](#) **57**, 1362–1365 (1986).
- ⁸S. Florens, and A. Georges, “Slave-rotor mean-field theories of strongly correlated systems and the Mott transition in finite dimensions”, *Physical Review B* **70**, 035114 (2004).

- ⁹S. Florens, and A. Georges, “Quantum impurity solvers using a slave rotor representation”, *Physical Review B* **66**, 165111 (2002).
- ¹⁰B. Lau, and A. J. Millis, “Theory of the Magnetic and Metal-Insulator Transitions in RNiO_3 Bulk and Layered Structures”, *Physical Review Letters* **110**, 126404 (2013).
- ¹¹G. Kotliar, and D. Vollhardt, “Strongly Correlated Materials: Insights From Dynamical Mean-Field Theory”, *Physics Today* **57**, 53 (2004).
- ¹²G. Kotliar, S. Y. Savrasov, K. Haule, V. S. Oudovenko, O. Parcollet, and C. A. Marianetti, “Electronic structure calculations with dynamical mean-field theory”, *Reviews of Modern Physics* **78**, 865–951 (2006).
- ¹³X. Deng, M. Ferrero, J. Mravlje, M. Aichhorn, and A. Georges, “Hallmark of strong electronic correlations in LaNiO_3 : Photoemission kink and broadening of fully occupied bands”, *Physical Review B - Condensed Matter and Materials Physics* **85**, 2–6 (2012).
- ¹⁴K. Haule, “Exact Double Counting in Combining the Dynamical Mean Field Theory and the Density Functional Theory”, *Physical Review Letters* **115**, 196403 (2015).
- ¹⁵S. R. Hassan, and L. DeMedici, “Slave spins away from half filling: Cluster mean-field theory of the Hubbard and extended Hubbard models”, *Physical Review B* **81**, 035106 (2010).
- ¹⁶L. De’Medici, A. Georges, and S. Biermann, “Orbital-selective Mott transition in multiband systems: Slave-spin representation and dynamical mean-field theory”, *Physical Review B* **72**, 205124 (2005).
- ¹⁷A. B. Georgescu, and S. Ismail-Beigi, “Generalized slave-particle method for extended Hubbard models”, *Physical Review B* **92**, 235117 (2015).

- ¹⁸L. De'Medici, "Hund's coupling and its key role in tuning multiorbital correlations", [Physical Review B - Condensed Matter and Materials Physics](#) **83**, 1–11 (2011).
- ¹⁹B. A. D. Ceperley, "Ground state of the electron gas by a stochastic model", *Phys. Rev. Lett.* **45**, 566–569.
- ²⁰J. P. Perdew, and A. Zunger, "Self-interaction correction to density-functional approximations for many-electron systems", [Physical Review B](#) **23**, 5048–5079 (1981).
- ²¹J. P. Perdew, M. Ernzerhof, and K. Burke, "Rationale for mixing exact exchange with density functional approximations", *J. Chem. Phys.* **105**, 9982 (1996).
- ²²P. Giannozzi, S. Baroni, N. Bonini, M. Calandra, R. Car, C. Cavazzoni, D. Ceresoli, G. L. Chiarotti, M. Cococcioni, I. Dabo, A. Dal Corso, S. de Gironcoli, S. Fabris, G. Fratesi, R. Gebauer, U. Gerstmann, C. Gougousis, A. Kokalj, M. Lazzeri, L. Martin-Samos, N. Marzari, F. Mauri, R. Mazzarello, S. Paolini, A. Pasquarello, L. Paulatto, C. Sbraccia, S. Scandolo, G. Sclauzero, A. P. Seitsonen, A. Smogunov, P. Umari, and R. M. Wentzcovitch, "QUANTUM ESPRESSO: a modular and open-source software project for quantum simulations of materials.", [Journal of physics. Condensed matter : an Institute of Physics journal](#) **21**, 395502 (2009).
- ²³<http://www.physics.rutgers.edu/dhv/uspp/>,
- ²⁴L. Bellaiche, and D. Vanderbilt, "The virtual crystal approximation revisited: Application to dielectric and piezoelectric properties of perovskites", *Physical Review B* **61**, 7877 (1999).

- ²⁵H. Chen, and S. Ismail-Beigi, “Ferroelectric control of magnetization in $\text{La}_{1-x}\text{Sr}_x\text{MnO}_3$ manganites: A first-principles study”, *Physical Review B - Condensed Matter and Materials Physics* **86**, 1–13 (2012).
- ²⁶H. Chen, Q. Qiao, M. S. J. Marshall, A. B. Georgescu, A. Gulec, P. J. Phillips, R. F. Klie, F. J. Walker, and C. H. Ahn, “Reversible Modulation of Orbital Occupations via an Interface- Induced Polar State in Metallic Manganites”, *Nano. Lett* **14**, 4965–4970 (2014).
- ²⁷V. I. Anisimov, F. Aryasetiawan, and I. Lichtenstein, “First-principles calculations of the electronic structure and spectra of strongly correlated systems: the LDA + U method”, *J. Phys.: Condens. Matter* **9**, 767–808 (1997).
- ²⁸N. Marzari, and D. Vanderbilt, “Maximally Localized Generalized Wannier Functions for Composite Energy Bands”, *Physical Review B* **56**, 12847 (1997).
- ²⁹N. Marzari, A. A. Mostofi, J. R. Yates, I. Souza, and D. Vanderbilt, “Maximally localized Wannier functions: Theory and applications”, *Reviews of Modern Physics* **84**, 1419–1475 (2012).
- ³⁰W. Luo, M. Varela, J. Tao, S. J. Pennycook, and S. T. Pantelides, “Electronic and crystal-field effects in the fine structure of electron energy-loss spectra of manganites”, *Physical Review B* **79**, 052405 (2009).
- ³¹M Varela, M. P. Oxley, W Luo, J Tao, M Watanabe, A. R. Lupini, S. T. Pantelides, and S. J. Pennycook, “Atomic-resolution imaging of oxidation states in manganites”, *Physical Review B* **79**, 085117 (2009).
- ³²H. P. Hjalmarson, H. Buttner, and J. D. Dow, “Theory of core excitons”, **24**, 6010–6019 (1981).

- ³³M. Imada, A. Fujimori, and Y. Tokura, "Metal-insulator transitions", *Reviews of Modern Physics* **70**, 1039–1263 (1998).
- ³⁴S. Nakatsuji, and Y. Maeno, "Quasi-Two-Dimensional Mott Transition System $\text{Ca}_{2-x}\text{Sr}_x\text{RuO}_4$ ", *Physical Review Letters* **84**, 2666–2669 (2000).
- ³⁵V. Anisimov, I. Nekrasov, D. Kondakov, T. Rice, and M. Sigrist, "Orbital-selective Mott-insulator transition in $\text{Ca}_{2-x}\text{Sr}_x\text{RuO}_4$ ", *Eur. Phys. J. B* **25**, 191–201 (2002).
- ³⁶A. Georges, G Kotliar, W. Krauth, and M. Rozenberg, "Dynamical mean-field theory of strongly correlated fermion systems and the limit of infinite dimensions", *Reviews of Modern Physics* **68**, 13–125 (1996).
- ³⁷S. E. Barnes, "New method for the Anderson model", *Journal of Physics F* **6**, 1375–1383 (1976).
- ³⁸P. Coleman, "New approach to the mixed-valence problem", *Physical Review B* **29**, 3035 (1984).
- ³⁹N Read, and D. M. Newns, "A new functional integral formalism for the degenerate Anderson model", *Journal of Physics C: Solid State Physics* **16**, L1055–L1060 (1983).
- ⁴⁰N. Read, "Anderson model", *Journal of Physics C: Solid State Physics* **18**, 2651–2665 (1985).
- ⁴¹P. A. Lee, N. Nagaosa, and X. G. Wen, "Doping a Mott insulator: Physics of high-temperature superconductivity", *Reviews of Modern Physics* **78**, 17 (2006).
- ⁴²M. Raczkowski, R. Fresard, and A. M. Oles, "Interplay between incommensurate phases in the cuprates", *Europhysics Letters* **76**, 128 (2006).

- ⁴³R. Fresard, and G. Kotliar, “Interplay of Mott Transition and Ferromagnetism in the Orbitally Degenerate Hubbard Model”, *Physical Review B* **56**, 12909 (1997).
- ⁴⁴F. Lechermann, A. Georges, G. Kotliar, and O. Parcollet, “Rotationally invariant slave-boson formalism and momentum dependence of the quasiparticle weight”, *Physical Review B* **76**, 155102 (2007).
- ⁴⁵J. Bünenmann, “A slave-boson mean-field theory for general multi-band Hubbard models”, *Physica Status Solidi (B) Basic Research* **248**, 203–211 (2011).
- ⁴⁶B. Lau, and A. J. Millis, “Theory of the magnetic and metal-insulator transitions in RNiO₃ bulk and layered structures”, *Physical Review Letters* **110**, 126404 (2013).
- ⁴⁷L. De Medici, G. Giovannetti, and M. Capone, “Selective Mott physics as a key to iron superconductors”, *Physical Review Letters* **112**, 177001 (2014).
- ⁴⁸J. Kanamori, “Electron Correlation and Ferromagnetism of Transition Metals”, *Progress of Theoretical Physics* **30**, 275–289 (1963).
- ⁴⁹E. Zhao, and A. Paramekanti, “Self-consistent slave rotor mean-field theory for strongly correlated systems”, *Physical Review B* **76**, 195101 (2007).
- ⁵⁰W. Brinkman, and T. Rice, “Application of Gutzwiller’s Variational Method to the Metal-Insulator Transition”, *Physical Review B* **2**, 4302 (1970).
- ⁵¹A. Koga, N. Kawakami, T. M. Rice, and M. Sgrist, “Orbital-selective Mott transitions in the degenerate Hubbard model”, *Physical Review Letters* **92**, 216402–1 (2004).

- ⁵²Y. M. Quan, L. J. Zou, D. Y. Liu, and H. Q. Lin, "Competition between crystal field splitting and Hund's rule coupling in two-orbital magnetic metal-insulator transitions", *European Physical Journal B* **85**, 1–5 (2012).
- ⁵³A. D. Becke, "A new mixing of Hartree–Fock and local density-functional theories", *The Journal of Chemical Physics* **98**, 1372 (1993).
- ⁵⁴L. Hedin, "New Method for Calculating the One-Particle Green's Function with Application to the Electron-Gas Problem", *Physical Review* **139**, A796 (1965).
- ⁵⁵M. S. Hybertsen, and S. G. Louie, "Electron correlation in semiconductors and insulators: Band gaps and quasiparticle energies", *Physical Review B* **34**, 5390 (1986).
- ⁵⁶F. Aryasetiawan, and O. Gunnarsson, "The GW method", *Reports on Progress in Physics* **61**, 237–312 (1998).
- ⁵⁷M. van Schilfgaarde, T. Kotani, and S. Faleev, "Quasiparticle Self-Consistent GW Theory", *Physical Review Letters* **96**, 226402–4 (2006).
- ⁵⁸E. H. Lieb, and F. Y. Wu, "The one-dimensional hubbard model: A reminiscence", *Exactly Solved Models: A Journey in Statistical Mechanics: Selected Papers with Commentaries (1963-2008)* **321**, 535–561 (2009).
- ⁵⁹M. M Sánchez, A. Avella, and F. Mancini, "The half-filled Hubbard chain in the Composite Operator Method: A comparison with Bethe Ansatz", *Europhysics Letters (EPL)* **44**, 328–334 (1998).
- ⁶⁰<http://www.wannier.org/>,

- ⁶¹M. Takizawa, M. Minohara, H. Kumigashira, D. Toyota, M. Oshima, H. Wadati, T. Yoshida, A. Fujimori, M. Lippmaa, M. Kawasaki, H. Koinuma, G. Sordi, and M. Rozenberg, "Coherent and incoherent d band dispersions in SrVO₃", *Physical Review B - Condensed Matter and Materials Physics* **80**, 235104 (2009).
- ⁶²E. Benckiser, M. W. Haverkort, S. Brück, E. Goering, S. Macke, A. Frañó, X. Yang, O. K. Andersen, G. Cristiani, H.-U. Habermeier, A. V. Boris, I. Zegkinoglou, P. Wochner, H.-J. Kim, V. Hinkov, and B. Keimer, "Orbital reflectometry of oxide heterostructures.", *Nature materials* **10**, 189–193 (2011).
- ⁶³J Chakhalian, J. W. Freeland, H Habermeier, G Cristiani, G Khaliullin, M. V. Veenendaal, and B Keimer, "Orbital Reconstruction and Covalent Bonding at an Oxide Interface", *Science* **318**, 1114–1117 (2007).
- ⁶⁴A. D. Rata, A Herklotz, K. Nenkov, L. Schultz, and K Doerr, "Strain-induced insulator state and giant gauge factor of La_{0.7}Sr_{0.3}CoO₃ films", *Physical Review Letters* **100**, 076401 (2008).
- ⁶⁵A. Tebano, C. Aruta, S. Sanna, P. G. Medaglia, G. Balestrino, A. A. Sidorenko, R. De Renzi, G. Ghiringhelli, L. Braicovich, V. Bisogni, and N. B. Brookes, "Evidence of orbital reconstruction at interfaces in ultrathin La_{0.67}Sr_{0.33}MnO₃ Films", *Physical Review Letters* **100**, 2–5 (2008).
- ⁶⁶M. Huijben, L. W. Martin, Y. H. Chu, M. B. Holcomb, P. Yu, G. Rijnders, D. H. A. Blank, and R. Ramesh, "Critical thickness and orbital ordering in ultrathin La_{0.7} Sr_{0.3} MnO₃ films", *Physical Review B - Condensed Matter and Materials Physics* **78**, 094413 (2008).

- ⁶⁷M. Salluzzo, J. C. Cezar, N. B. Brookes, V. Bisogni, G. M. De Luca, C. Richter, S. Thiel, J. Mannhart, M. Huijben, A. Brinkman, G. Rijnders, and G. Ghiringhelli, "Orbital reconstruction and the two-dimensional electron gas at the LaAlO₃/SrTiO₃ interface", [Physical Review Letters](#) **102**, 166804 (2009).
- ⁶⁸P. Yu, J. S. Lee, S. Okamoto, M. D. Rossell, M. Huijben, C. H. Yang, Q. He, J. X. Zhang, S. Y. Yang, M. J. Lee, Q. M. Ramasse, R. Erni, Y. H. Chu, D. A. Arena, C. C. Kao, L. W. Martin, and R. Ramesh, "Interface ferromagnetism and orbital reconstruction in BiFeO₃-La_{0.7}Sr_{0.3}MnO₃ heterostructures", [Physical Review Letters](#) **105**, 027201 (2010).
- ⁶⁹Y Tokura, and N. Nagaosa, "Orbital Physics in Transition Metal Oxides", [Science](#) **288**, 462–468 (2000).
- ⁷⁰M. B. Salamon, and M. Jaime, "The physics of manganites: Structure and transport", [Reviews of Modern Physics](#) **73**, 583–628 (2001).
- ⁷¹I. Solovyev, N. Hamada, and K. Terakura, "Crucial Role of the Lattice Distortion in the Magnetism of LaMnO₃", [Physical Review Letters](#) **76**, 4825–4828 (1996).
- ⁷²H. J. A. Molegraaf, J. Hoffman, C. A. F. Vaz, S. Gariglio, D. Van Der Morel, C. H. Ahn, and J. M. Triscone, "Magnetoelectric effects in complex oxides with competing ground states", [Advanced Materials](#) **21**, 1–5 (2009).
- ⁷³H. Lu, T. A. George, Y. Wang, I. Ketsman, J. D. Burton, C. W. Bark, S. Ryu, D. J. Kim, J. Wang, C. Binek, P. A. Dowben, A. Sokolov, C. B. Eom,

- E. Y. Tsymbal, and A. Gruverman, "Electric modulation of magnetization at the BaTiO₃/La_{0.67}Sr_{0.33}MnO₃ interfaces", [Applied Physics Letters](#) **100**, 232904 (2012).
- ⁷⁴D Eichler, S. G. Lucek, F. a. Aharonian, V. N. Zirakashvili, W. M. Goss, C. L. Brogan, M. J. Claussen, J. Rho, T. H. Jarrett, S. D. Hunter, G Kanbach, P Sreekumar, J. M. Cordes, R. J. Dewey, K. D. Kuntz, R. L. Shelton, E. B. Giacani, G Dubner, C Brogan, N. E. Kassim, R. a. Chevalier, D. C. Ellison, Y. a. Uvarov, I. V. Moskalenko, a. W. Strong, A Mastichiadis, R. H. Becker, R. L. White, A Fallon, and S Tuttle, "Ferroelectric Control of", *Science*, 1106–1110 (2010).
- ⁷⁵J. D. Burton, and E. Y. Tsymbal, "Prediction of electrically induced magnetic reconstruction at the manganite/ferroelectric interface", [Physical Review B - Condensed Matter and Materials Physics](#) **80**, 174406 (2009).
- ⁷⁶J. D. Burton, and E. Y. Tsymbal, "Giant tunneling electroresistance effect driven by an electrically controlled spin valve at a complex oxide interface", [Physical Review Letters](#) **106**, 157203 (2011).
- ⁷⁷C. A. F. Vaz, J. Hoffman, Y. Segal, J. W. Reiner, R. D. Grober, Z. Zhang, C. H. Ahn, and F. J. Walker, "Origin of the magnetoelectric coupling effect in Pb(Zr_{0.2}Ti_{0.8})O₃/La_{0.8}Sr_{0.2}MnO₃ multiferroic heterostructures", [Physical Review Letters](#) **104**, 127202 (2010).
- ⁷⁸J. A. Mundy, Y Hikita, T Hidaka, T Yajima, T Higuchi, H. Y. Hwang, D. A. Muller, and L. F. Kourkoutis, "Visualizing the interfacial evolution from charge compensation to metallic screening across the manganite metal-insulator transition", [Nat Commun](#) **5**, 3464 (2014).

- ⁷⁹P. Cueva, R. Hovden, J. A. Mundy, H. L. Xin, and D. A. Muller, "Microscopy Microanalysis Data Processing for Atomic Resolution Electron Energy Loss Spectroscopy", *Microscopy and Microanalysis* **18**, 667–675 (2012).
- ⁸⁰H. Seo, A. Posadas, and A. A. Demkov, "Strain-driven spin-state transition and superexchange interaction in LaCoO₃: Ab initio study", *Physical Review B - Condensed Matter and Materials Physics* **86**, 1–9 (2012).
- ⁸¹A. S. Disa, D. P. Kumah, A. Malashevich, H. Chen, D. a. Arena, E. D. Specht, S. Ismail-beigi, F. J. Walker, and C. H. Ahn, "Orbital Engineering in Symmetry-Breaking Polar Heterostructures", *Phys. Rev. Lett.* **114**, 026801 (2015).
- ⁸²R. Chen, S. Lee, and L. Balents, "Dimer Mott insulator in an oxide heterostructure", *Physical Review B - Condensed Matter and Materials Physics* **87**, 2–5 (2013).
- ⁸³H. Park, A. J. Millis, and C. a. Marianetti, "Site-selective Mott transition in rare-earth-element nickelates", *Physical Review Letters* **109**, 1–5 (2012).
- ⁸⁴H. Park, A. J. Millis, and C. A. Marianetti, "Computing total energies in complex materials using charge self-consistent DFT+DMFT", *Physical Review B - Condensed Matter and Materials Physics* **90**, 1–17 (2014).